5-21-2005

Modeling Shape Effects in Nano Magnetic Materials With Web Based Micromagnetics

Zhidong Zhao
University of New Orleans

MODELING SHAPE EFFECTS IN NANO MAGNETIC MATERIALS WITH WEB BASED MICROMAGNETICS

A Dissertation

Submitted to the Graduate Faculty of the
University of New Orleans
in partial fulfillment of the
requirements for the degree of

Doctor of Philosophy
in
Chemistry

by

Zhidong Zhao

B.S., Huazhong University of Science and Technology, 1989
M.S., Beijing Normal University, 1992

May 2004

Acknowledgement

I would like to express my sincere thanks to my supervisor, Professor Scott L. Whittenburg, for his encouragement, guidance, support and fruitful discussions throughout this work.

I am very grateful to Dr. J. Wang from the Advanced Materials Research Institute and people from the Department of Chemistry for their support and help.

I thank my wife and parents for their continuous love and sacrifice.

Table of Contents

List of Tables

List of Schemas

List of Figures

Abstract

This research work focuses on the geometry and shape effects on submicron magnetic material. A web based micromagnetics program is written to model the hysteresis loop of nano magnetic samples with arbitrary geometry shapes and multiple magnetic materials.

Three material samples have been modeled with this program along with nano magnets with a variety of geometric shapes.

Shape anisotropy has been introduced to a permalloy ring by adding a cross-tie structure with various widths. The in-plane hysteresis loop and reversal behavior have no notable difference in direction parallel to the cross-tie, but greatly changed in perpendicular and diagonal directions. The switching field distribution is significantly reduced. The two distinct "onion" bit states of the modified ring elements are stabilized in the hysteresis in the diagonal direction. The changes in the modified rings make them better candidates for Magnetic Random Access Memory elements.

Two Pac-Man elements, PM I and PM II, geometrically modified from disc and half disc respectively, are modeled. The PM I element undergoes a magnetic reversal through a two-stage mechanism that involves nucleation in the left and right middle areas followed by vortex core formation and vortex core motion in the lower middle area. The

reversal process of the PM II element lacks the vortex core formation and motion stage. The switching field of the PM I and PM II elements are the same but the switching field distribution of the PM II elements is much narrower than that of the PM I element. Only the PM II element meets MRAM application requirements.

The thickness dependence of the magnetic properties of a core-shell structure has been studied. The nano particles have a cobalt core and a permalloy shell. The nano spheres are the same size but with various shell thickness. Simulations reveal a multi-stage reversal process without the formation of a Bloch wall for thin-shell structure and smooth reversal process with the formation and motion of a Bloch wall for thick-shell structure. Gradual transition of the hysteresis loop patterns has been observed.

Chapter 1 Introduction

1.1 Magnetic Nanostructures

Magnetism is a property of materials known for centuries. For many years, the focus was on macroscopic magnetism, such as compass and geomagnetic field. Macroscopic magnetism can be related to its atomic-scale origin. These origins include quantum-mechanical exchange,[1] crystal-field interaction[2] and relativistic spin-orbit coupling.[3] This understanding of the atomic-scale origin of magnetism has arisen through quantum-mechanical theory in the first half of the twentieth century. It is now clear that many solid-state magnetic properties are rooted in nanoscale structural effects. Nanostructuring is exploited in permanent magnets, soft magnets, hard-soft permanent-magnet composites[4] and recording media, in particular, ultra-high density magnetic random access memory.[5] Magnetic nanostructures are characterized by various geometries, ranging from naturally existing fine particles, clusters and particle arrays to thin films, multilayers and nanowires.

The typical diameter of natural nano particles is about 10nm. Very small particles are often known as clusters. Due to their high surface to volume ratio and their small size, clusters are single domain magnets and are normally in the superparamagnetic state at high temperature.[6] Large particle arrays may have thickness up to 50nm and lateral dimensions of up to 1 micron. They may be found in flux closure domains.[7] Magnetic

thin films and multilayers have been used as permanent magnets and magnetic recording media. Research interests in thin films include anisotropy,[8] moment modification,[9] and exchange coupling on or near film interfaces.[10]

1.2 Magnetic Properties

The magnetic moment, m, of solids often originates from the electrons in partly filled inner electron shells of transition metal atoms. Commonly encountered transition metals are 3d elements, Fe, Co, Ni and 4f, 4d, 5d and 5f elements. The moment is basically determined by intra-atomic Coulomb interactions. On the contrary, inter-atomic exchange determines whether a material is ferromagnetic, ferrimagnetic or antiferromagnetic. Inter-atomic exchange is usually described by the Heisenberg interaction $-J\vec{S_1}\bullet\vec{S_2}$ between neighboring atomic spins $\vec{S_1}$ and $\vec{S_2}$. Positive J values produce ferromagnets, such as Fe and Co, while negative J value, as in the case of many oxides, produces antiferromagnets that are composed of multiple sublattices with opposite moments.

The energy of a magnetic solid depends on the orientation of the magnetization with respect to the crystal axes. This is known as magnetic anisotropy. Permanent magnets have high magnetic anisotropy where soft magnets have low magnetic anisotropy. Recording media and memory materials have intermediate anisotropy. For soft nanomagnets, shape anisotropy is important.[11,12] But for large particles, shape anisotropy is weakened by internal flux closures.[13]

The saturation magnetization, M_s, the first uniaxial anisotropy constant, K_1, and the exchange stiffness, A, which are of atomic origin, are intrinsic magnetic properties and

their bulk values are achieved in nanoparticles whose dimensions are greater than 1nm. Other properties, such as remanence, M_r , and coercivity, H_c , that measured using hysteresis are extrinsic. These properties depend on the structure of magnetic sample. Particle size has a pronounced role in determining the ground state domain configuration and the magnetization reversal mechanism for small magnetic particles.[14]

1.3 Magnetization Reversal Processes

Magnetization reversal occurs through two basic processes, namely the coherent rotation or Stoner-Wohlfrath reversal[15] and curling.

The stability of the remanent state is characterized by the coercivity, H_c. For small particles where the exchange is sufficiently strong to ensure that magnetization is constant throughout the magnet such that $\nabla M = 0$, a good estimate is $H_c = \frac{2K_1}{m_0 M_s} + \frac{1}{2}(1-3D)M_s$, where D is the magnetostatic interaction parameter. The coercivity defines a 'nucleation' field. When the size of a nano particle is smaller than a coherence radius, the exchange energy dominates and the nucleation is realized by coherent rotation. For most common elements, the coherence radius is in the range of $1 \sim 10nm$. The coherence radius is anisotropy independent and is usually smaller than the exchange length. Beyond the coherence radius, nucleation or other incoherent rotations, such as domain-wall pinning and domain-wall motion will become the major mechanism of magnetic reversal. Nucleation is different from domain-wall pinning in that nucleation is defect-free and domain-free. The coercivity of a nucleation controlled magnetic sample is essentially given by the nucleation field, while the pinning force is associated with macroscopic mechanical strain. Pinning can be used to tune the coercivity of some

mesoscopic magnets through grain-boundary features, typically in high-temperature applications.[16,17]

1.4 Size and Shape Effects on Reversal Process

Intrinsic magnetic properties, such as M_s, K_1 and A, are not size dependent, but other magnetic properties, most importantly, remanence and coercivity are affected by the element size and shape. These effects are especially pronounced in the nanometer range. A full set of epitaxial garnet elements with areas varying from 2000 to 5mm^2 was studied by Vertesy *et. Al.*[18] It was found that the type of domain structure, width of the stripe domain period, domain wall energy and anisotropy do not change with a reduction of the sample size, but the coercivity was reduced by almost 10 fold. However, when particle sizes are comparable to the single domain length and exchange length, reducing the particle size will decrease the possibility of curling. This may cause the coercivity of some elements to be greater than their bulk coercivity. Chains of square and disk shaped permalloy dots were studied using MOKE, magnetic force microscopy and micromagnetic modeling.[19] The switching fields were found to be strongly affected by the particle shape, but the strength of inter dot interactions in chains of magnetostatically coupled elements were not influenced by the shape, when the dots were well separated. The switching fields in easy-axis and hard-axis directions on an array of thick garnet particles were found to be much smaller than the crystalline anisotropy field.[20] The end shape affects the domain configuration of deep submicron elements and eventually changes the switching fields and switching behavior.[21,22] Defects in the particles, rather than shape anisotropy, are attributed to the reduction of the switching field. Besides size

and shape, element thickness also plays an important role in determining the characteristics of hysteresis loops, particularly in exchange coupled multilayers, spin valves and regular nano-particles. These effects are summarized in the term "configurational anisotropy".

For magnetic memory and sensor applications, nano magnetic elements with various geometry shapes have been investigated, in an attempt to modify the hysteresis loops and reversal processes. To name a few, solid elements, such as square, rectangle, ellipse,[23] hexagon,[24] circular disc and elements with a center core removed, such as rings and modified rings,[25?27] have been extensively studied. Uncontrollable single vortex or double vortex formations during magnetic reversal are found in low aspect ratio elliptical permalloy dots, while high aspect ratio elliptical permalloy dots reverse through vortex-free paths.[28] Array of the aforementioned elements have also studied both experimentally and numerically.

Chapter 2 Micromagnetic Model

2.1 Magnetic Energy

The evolution of a magnetic system leads to a local minimum on the magnetic free energy surface. The magnetic free energy, better known as the Landau free energy, is a functional of the space-dependent magnetization, field and temperature. Due to magnetic viscosity, the magnetization, external field and temperature do not exclusively determine the state of a magnetic system. The current state of the system also depends on its history. Every local minimum on the magnetic free energy surface corresponds to a metastable state. The transition from one metastable state to another metastable state occurs through a Barkhausen jump.[29] Normally, thermal relaxation is fast, compared with the time required to achieve a metastable state under a varying applied field. In many micromagnetic simulations, thermal relaxation is neglected. This implies that once a system is in a metastable state, it remains in that state indefinitely, unless the applied field changes.

Neglecting thermal fluctuation, the magnetic free energy is composed of the exchange energy E_e, the anisotropy energy E_a, the magnetostatic or demag energy E_d and the external or Zeeman energy E_z. The magnetic free energy is expressed by the following:

$$G_L = \int_v \left[A\left(\nabla \vec{m}\right)^2 + f_a\left(\vec{m}, \vec{a}\right) - \frac{m_0}{2} M_s \vec{H_d} \bullet \vec{m} - m_0 M_s \vec{H_z} \bullet \vec{m} \right] d^3 r \qquad (2.1)$$

The first term of the integrand in Eq. 2.1 is the exchange energy density. It is a short hand notation for $A\left(\left|\nabla \vec{m_x}\right|^2 + \left|\nabla \vec{m_y}\right|^2 + \left|\nabla \vec{m_z}\right|^2\right)$ which represents the space gradient of the magnetization. The exchange energy originates from the atomic-scale Colombo exchange integral that occurs only between nearest neighbors. The exchange stiffness A can be estimated as $A \sim kJS^2/c$ where k is a numeric factor on the order of unity, J is the exchange integral, S is the spin magnitude and c is the lattice constant. A can also be experimentally determined from the Curie temperature. The exchange energy depends on the gradient of the magnetization, not the orientation of the magnetization. The exchange field prefers the spin vectors to align parallel for $A > 0$ and anti-parallel for $A < 0$.

The second term in Eq. 2.1 is the anisotropy energy density. It represents the preference of the magnetization direction with respect to the lattice. The anisotropy effect has two origins, the magnetocrystalline anisotropy that reflects the spin-orbit coupling and the magnetostriction anisotropy that reflects the magnetoelastic coupling to the lattice. Other types of anisotropy, such as shape anisotropy and exchange anisotropy, are magnetostatic and exchange effects that appear to be anisotropic.

The third term in Eq. 2.1 is the magnetostatic energy density. The corresponding field, $\vec{H_d}$, is the magnetostatic field. It is subject to the following two conditions:

$$\begin{aligned} \nabla \bullet \vec{H_d} &= -\nabla \bullet \left(M_s \vec{m}\right) \\ \nabla \times \vec{H_d} &= 0 \end{aligned} \qquad (2.2)$$

The second condition in Eq. 2.2 implies the magnetostatic field is the gradient of a

scalar potential field. The magnetostatic effect is a long range effect. The curl of magnetostatic field is zero everywhere in the bulk of a magnetic sample. It requires the spin vectors in the bulk to align head to tail. The magnetostatic term aligns spin vectors along the surface. For nano magnets the effect of this requirement is pronounced.

The last term in Eq. 2.1 is the energy density arising from the external applied field. It is normally known as the Zeeman energy after Pieter Zeeman.

2.2 Landau-Lifshiftz-Gilbert Equation

The magnetic energy equation, Eq. 2.1, is a continuum model. The properties M and H are phenomological continuous vector fields. To describe the magnetic system, a magnetic sample is discretized into a grid of rectangular cells. This is a finite difference approach. Although micromagnetics is based on atomic scale interaction theories, the size of each cell is large enough so that the atomic scale effects are represented by continuum fields. On the other hand, the size of each cell is small enough to guarantee that the atomic properties in each cell are uniform. In this context, the magnetization in the cell is constant in direction and magnitude and is represented by a vector spin that stands for hundreds or thousands of atomic spins. The size of a cell is scaled by a characteristic length l_{ex}. l_{ex} is known as the exchange length where exchange energy is comparable to magnetostatic energy. l_{ex} is given by $\sqrt{\frac{2A}{m_0 M_s^2}}$ where A is the exchange stiffness and M_s is the saturation magnetization. Since typical ferromagnets have M_s around 1T or 7.9×10^5 A/M and exchange stiffness around 10^{-12} J/M, the theoretical exchange length is found around 1nm. But, the experimental exchange length is normally around 10nm.[30]

According to William Fuller Brown, the magnetization, M, of a metastable state must satisfy:

$$\vec{m} \times \vec{H} = 0 \tag{2.3}$$

and a boundary condition:

$$\frac{d\vec{M}}{dn} = 0 \tag{2.4}$$

In Eq. 2.3 $\vec{H}$ is the local effective field. Eq. 2.4 requires the derivative of magnetization in the surface normal direction be zero. For a system with non-zero normal derivative of magnetization, it is said to have a surface anisotropy contribution.

The magnitude of each spin remains constant but its orientation is variable. The motion of the spin vector is governed by the Landau-Lifshiftz-Gilbert Equation:

$$\frac{d\vec{M}}{dt} = -g\vec{M} \times \vec{H} - \frac{ga}{M_s}\vec{M} \times \left(\vec{M} \times \vec{H}\right) \tag{2.5}$$

Eq. 2.5 is composed of two terms. The first is the precession term which rotates the magnetization to spin around its effective field. The precession can be observed by magnetic resonance. The second is an empirical damping term that brings the spin closer to its field axis through energy dissipation. $g = \frac{g m_0 e}{2m} = 2.21 \times 10^5 \frac{M}{As}$ is the gyromagnetic ratio where g is the Lande hyperfine structure factor, m_0 is the permeability in vacuum, e and m are the charge and mass of electron and a is the dimensionless empirical damping constant. A related parameter is the attempt frequency for spin flipping:

$$\begin{aligned} f &= f_0 \exp\left(-E_B / k_B T\right) \\ f_0 &= agM_s \end{aligned} \tag{2.6}$$

In Eq. 2.6 E_B is the energy barrier to spin flip, k_B is the Boltzman's constant and

T is temperature. f_0 is in the proximity of 1GHz and the observed damping constant is in the range of 0.001~0.1. In practical micromagnetic simulations, a is usually set as 0.5, up to 1.0, to decrease the calculation time needed to reach metastable states.

The LLG equation can be rewritten into a simpler form using reduced units.

Field and magnetization are reduced with the saturation magnetization:

$$\vec{h} = \vec{H} / M_s$$
$$\vec{m} = \vec{M} / M_s \qquad (2.7)$$

In Eq. 2.7 $\vec{h}$ is the dimensionless reduced field vector and $\vec{m}$ is the dimensionless reduced spin vector. The magnitude of reduced spin vector should always be unity.

Energy is reduced as follows:

$$e = \frac{E}{m_0 M_s^2 V} \qquad (2.8)$$

In Eq. 2.8 V is the volume of a cell and e is the dimensionless energy density.

Time is reduced as follows:

$$t = g M_s t \qquad (2.9)$$

In Eq. 2.9 t is the dimensionless time while t is the real time.

It is worth noting that for a system with multiple materials, the properties for each cell reduce with regard to the saturation magnetization of its own material. Therefore, the dimensionless time may be different for different materials.

Inserting Eqs 2.8, 2.9 and 2.10 into 2.5 yields:

$$\frac{dM_s\vec{m}}{d\frac{t}{g\,M_s a}} = -g\,M_s\vec{m}\times M_s\vec{h} - \frac{ga}{M_s}M_s\vec{m}\times\left(M_s\vec{m}\times M_s\vec{h}\right)$$

or (2.10)

$$\frac{d\vec{m}}{dt} = -\vec{m}\times\vec{h} - a\,\vec{m}\times\left(\vec{m}\times\vec{h}\right)$$

Exploiting the vector identity $\vec{m}\times\left(\vec{m}\times\vec{h}\right) = \left(\vec{m}\bullet\vec{h}\right)\vec{m} - \left(\vec{m}\bullet\vec{m}\right)\vec{h}$ and the fact that $\vec{m}\bullet\vec{m} = \left|\vec{m}\right|^2 = 1$, the LLG equation can be further reduced to:

$$\begin{aligned}\frac{d\vec{m}}{dt} &= -\vec{m}\times\vec{h} - a\,\vec{m}\times\left(\vec{m}\times\vec{h}\right)\\ &= -\left|\vec{m}\right|\left|\vec{h}\right|\sin q - a\left|\vec{m}\right|^2\left|\vec{h}\right|\left(\vec{m}\cos q - \vec{\hat{h}}\right)\\ &= -\left|\vec{h}\right|\left(\sin q + a\left(\vec{m}\cos q - \vec{\hat{h}}\right)\right)\end{aligned} \quad (2.11)$$

where q is the angle between $\vec{m}$ and $\vec{h}$ and $\vec{\hat{h}}$ is the unity vector in the field direction.

2.3 Magnetic Fields

The magnetic field can be derived from the magnetic energy density:

$$\vec{H} = -\frac{1}{m_0}\frac{\partial E}{\partial\vec{M}} = -\frac{1}{m_0 M_s}\frac{\partial E}{\partial\vec{m}} \quad (2.12)$$

Neglecting thermal fluctuations, the local effective field in Eq. 2.5 consists of four components, namely the exchange field, the anisotropy field, the demagnetization or demag field and the applied field.

$$\vec{H} = \vec{H_a} + \vec{H_e} + \vec{H_d} + \vec{H_z} \quad (2.13)$$

2.3.1 Exchange Field

In discretized form, the anisotropy energy density for a cell i is calculated among its nearest neighbors $j \in NN$. It has the following form:

$$\overline{E_{e,i}} = \sum_{j \in NN} A_{ji} \frac{\left|\overrightarrow{m_j} - \overrightarrow{m_i}\right|^2}{\left|R_j - R_i\right|^2} = \sum_{j \in NN} \frac{A_{ji}}{\left|R_j - R_i\right|^2} \left|\overrightarrow{m_j} - \overrightarrow{m_i}\right|^2 \qquad (2.14)$$

In Eq. 2.14 $\overline{E_{e,i}}$ is the anisotropy energy density of cell i, A_{ij} is the exchange constant between cell i and its neighbor j. If i and j are of same material, A_{ij} is simply the exchange stiffness of that material. Otherwise, an empirical coupling exchange constant must be used. In the later case, the exchange constant is usually taken as the geometric average of exchange stiffness of the two coupling materials. In practice, this constant depends on the relative position between the coupling atoms or functional groups, including distance, relative axes orientation and surface roughness.

Besides neighboring exchange, there are other forms of exchange such as RKKY exchange interaction[31] at a much smaller size scale and inter-layer exchange interaction at a larger size scale between thin-film layers.[32] These types of exchange are not considered in this work.

The exchange field can be derived from Eq. 2.14 by Eq. 2.12:

$$\begin{aligned} \overrightarrow{h_{e,i}} &= \sum_{j \in NN} \frac{2A_{ji}}{m_0 M_{s,i}^2} \frac{\overrightarrow{m_j} - \overrightarrow{m_i}}{\left|R_j - R_i\right|^2} = \sum_{j \in NN} \frac{2A_{ji}}{m_0 M_{s,i}^2 \left|R_j - R_i\right|^2} \left(\overrightarrow{m_j} - \overrightarrow{m_i}\right) \\ &= \sum_{j \in NN} a_{ji} \left(\overrightarrow{m_j} - \overrightarrow{m_i}\right) \qquad (2.14) \\ a_{ji} &= \frac{2A_{ji}}{m_0 M_{s,i}^2 \left|R_j - R_i\right|^2} \end{aligned}$$

a_{ij} is the reduced exchange constant. It is fixed during LLG integration and can be calculated once, stored separately and used repeatedly.

The exchange energy is split evenly between two coupled spins. Therefore for a

cell the reduced exchange energy is calculated using:

$$e_{e,i} = \sum_{j \in NN} \frac{1}{4} a_{ji} \left(\overrightarrow{m_j} - \overrightarrow{m_i} \right) \bullet \overrightarrow{m_i} \tag{2.15}$$

2.3.2 Anisotropy Field

Anisotropy means symmetry breaking. For different materials, the host lattice has different preferences in orientation for its spin. The direction in which the anisotropy energy is at a minimum is called the easy axis while the direction in which the anisotropy energy is at a maximum is called the hard axis. In the later case, spins prefer a plane perpendicular to the hard axis. According to the number of easy axes in a lattice, materials are classified into uniaxial, biaxial, cubic and higher order anisotropy.

2.3.2.1 Uniaxial Anisotropy

Uniaxial anisotropy energy is invariant upon rotation along the easy axis. Uniaxial anisotropy energy can be expressed as a power series of trigonometric functions of the angle q between magnetization and the easy axis. Since the energy surface is symmetric on rotation, only even functions are involved.

$$E_a / V = K_0 + K_1 \sin^2 q + K_2 \sin^4 q + ... \tag{2.16}$$

In Eq. 2.16 the coefficients K_0, K_1, K_2 and so forth are called anisotropy constants. The zero point of anisotropy energy is chosen to make it always non-negative. When K_1 is positive, the minimum occurs when $q = 0$ so K_0 is set to be zero. When K_1 is negative, the minimum occurs when $q = 90^\circ$, consequently $K_0 = -K_1$.

$$\begin{aligned} \overline{E_a} &= K_1 \sin^2 q + K_2 \sin^4 q, \ (K_1 \geq 0) \\ \overline{E_a} &= -K_1 + K_1 \sin^2 q + K_2 \sin^4 q = -K_1 \cos^2 q + K_2 \sin^4 q, \ (K_1 \leq 0) \end{aligned} \tag{2.17}$$

K_2 is normally negligible to K_1, so in many cases micromagnetic simulations include only K_1, but for some materials, K_2 is comparable to K_1 or even larger. This work uses the second anisotropy term when applicable.

Regardless of the sign of K_1, the anisotropy field is the same for uniaxial anisotropy material. Here $\sin q$ must be expressed in term of magnetization unity $\vec{m}$ and easy axis unity $\vec{a}$:

$$\begin{aligned}\vec{h_a} &= -\frac{1}{m_0 M_s^2}\frac{\partial}{\partial \vec{m}}\left(K_1\left(1-\left(\vec{m}\bullet\vec{a}\right)^2\right)+K_2\left(1-\left(\vec{m}\bullet\vec{a}\right)^2\right)^2\right), (K_1 \geq 0)\\ \vec{h_a} &= -\frac{1}{m_0 M_s^2}\frac{\partial}{\partial \vec{m}}\left(-K_1\left(\vec{m}\bullet\vec{a}\right)^2+K_2\left(1-\left(\vec{m}\bullet\vec{a}\right)^2\right)^2\right), (K_1 \leq 0)\end{aligned} \tag{2.18}$$

Simplification of Eq. 2.18 yields, for both positive and negative first anisotropy constant:

$$\begin{aligned}\vec{h_a} &= \frac{2K_1+4K_2}{m_0 M_s^2}\left(\vec{m}\cdot\vec{a}\right)\vec{a}-\frac{4K_2}{m_0 M_s^2}\left(\vec{m}\cdot\vec{a}\right)^3\vec{a}\\ &= \frac{\left(\vec{m}\cdot\vec{a}\right)\vec{a}}{m_0 M_s^2}\left(2K_1+4K_2\left(1-\left(\vec{m}\cdot\vec{a}\right)^2\right)\right)\\ &= \left(k_1+2k_2\left(1-\left(\vec{m}\cdot\vec{a}\right)^2\right)\right)\left(\vec{m}\cdot\vec{a}\right)\vec{a}\end{aligned} \tag{2.19}$$

where $k_1 = \frac{2K_1}{m_0 M_s^2}$ and $k_2 = \frac{2K_2}{m_0 M_s^2}$ are the reduced anisotropy constants. Using k_1 and k_2 the reduced energy is calculated using:

$$\begin{aligned}e_a &= \frac{k_1\left(1-\vec{m}\bullet\vec{a}\right)^2+k_2\left(1-\left(\vec{m}\bullet\vec{a}\right)^2\right)^2}{2}, (K_1 \geq 0)\\ e_a &= \frac{-k_1\left(\vec{m}\bullet\vec{a}\right)^2+k_2\left(1-\left(\vec{m}\bullet\vec{a}\right)^2\right)^2}{2}, (K_1 \leq 0)\end{aligned} \tag{2.20}$$

2.3.2.2 Cubic Anisotropy

A cubic anisotropy material has three orthogonal easy axes, namely a, b and c axes. The anisotropy energy density is expressed as a function of the three directional cosines.

$$\frac{E_a}{V} = K_1\left(\cos^2 a \cos^2 b + \cos^2 a \cos^2 g + \cos^2 b \cos^2 g\right) + K_2\left(\cos^2 a \cos^2 b \cos^2 g\right) \quad (2.20)$$

or in dimensionless form:

$$\begin{aligned} e_a &= \frac{E_a}{m_0 M_s^2 V} \\ &= \frac{K_1}{m_0 M_s^2}\left(\cos^2 a \cos^2 b + \cos^2 a \cos^2 g + \cos^2 b \cos^2 g\right) \\ &+ \frac{K_2}{m_0 M_s^2}\left(\cos^2 a \cos^2 b \cos^2 g\right) \\ &= \frac{k_1}{2}\left(\cos^2 a \cos^2 b + \cos^2 a \cos^2 g + \cos^2 b \cos^2 g\right) \\ &+ \frac{k_2}{2}\left(\cos^2 a \cos^2 b \cos^2 g\right) \\ &= \frac{k_1}{2}\left(\left(\vec{m}\bullet\vec{a}\right)^2\left(\vec{m}\bullet\vec{b}\right)^2 + \left(\vec{m}\bullet\vec{a}\right)^2\left(\vec{m}\bullet\vec{c}\right)^2 + \left(\vec{m}\bullet\vec{b}\right)^2\left(\vec{m}\bullet\vec{c}\right)^2\right) \\ &+ \frac{k_2}{2}\left(\vec{m}\bullet\vec{a}\right)^2\left(\vec{m}\bullet\vec{b}\right)^2\left(\vec{m}\bullet\vec{c}\right)^2 \end{aligned} \quad (2.21)$$

k_1 and k_2 are defined same as in the uniaxial anisotropy case.

The dimensionless cubic anisotropy field is calculated using:

$$
\begin{aligned}
\overrightarrow{h_a} &= -\frac{2K_1}{m_0 M_s^2}\left[\left(\left(\vec{m}\cdot\vec{b}\right)^2+\left(\vec{m}\cdot\vec{c}\right)^2\right)\vec{a}+\left(\left(\vec{m}\cdot\vec{a}\right)^2+\left(\vec{m}\cdot\vec{c}\right)^2\right)\vec{b}+\left(\left(\vec{m}\cdot\vec{a}\right)^2+\left(\vec{m}\cdot\vec{b}\right)^2\right)\vec{c}\right] \\
&\quad -\frac{2K_2}{m_0 M_s^2}\left[\left(\vec{m}\cdot\vec{b}\right)^2\left(\vec{m}\cdot\vec{c}\right)^2\vec{a}+\left(\vec{m}\cdot\vec{a}\right)^2\left(\vec{m}\cdot\vec{c}\right)^2\vec{b}+\left(\vec{m}\cdot\vec{a}\right)^2\left(\vec{m}\cdot\vec{b}\right)^2\vec{c}\right] \\
&= -\left(\left(\left(\vec{m}\cdot\vec{b}\right)^2+\left(\vec{m}\cdot\vec{c}\right)^2\right)k_1+\left(\vec{m}\cdot\vec{b}\right)^2\left(\vec{m}\cdot\vec{c}\right)^2 k_2\right)\vec{a} \\
&\quad -\left(\left(\left(\vec{m}\cdot\vec{a}\right)^2+\left(\vec{m}\cdot\vec{c}\right)^2\right)k_1+\left(\vec{m}\cdot\vec{a}\right)^2\left(\vec{m}\cdot\vec{c}\right)^2 k_2\right)\vec{b} \\
&\quad -\left(\left(\left(\vec{m}\cdot\vec{a}\right)^2+\left(\vec{m}\cdot\vec{b}\right)^2\right)k_1+\left(\vec{m}\cdot\vec{a}\right)^2\left(\vec{m}\cdot\vec{b}\right)^2 k_2\right)\vec{c} \\
&= -\left(\left(m_b^2+m_c^2\right)k_1+m_b^2 m_c^2 k_2\right)\vec{a} \\
&\quad -\left(\left(m_a^2+m_c^2\right)k_1+m_a^2 m_c^2 k_2\right)\vec{b} \\
&\quad -\left(\left(m_a^2+m_b^2\right)k_1+m_a^2 m_b^2 k_2\right)\vec{c}
\end{aligned}
\qquad (2.22)
$$

In Eq. 2.22 $m_x = \vec{m}\bullet\vec{x}, x = a,b,c$ is the projection of magnetization unity vector on easy axis x.

Besides uniaxial anisotropy and cubic anisotropy, other types of anisotropy are less common and are not implemented in this micromagnetics program. For a discussion of their inclusion into the program, see the appendix.

2.3.3 Magnetostatic Field

In a uniformly magnetized body, the internal magnetic field and demagnetizing energy can be conveniently expressed in terms of a demagnetizing tensor.

$$\overrightarrow{H_d} = -\widetilde{N}\bullet\overrightarrow{M} \qquad (2.23)$$

The demagnetizing energy is

$$E_d = -\frac{m_0}{2}\overrightarrow{M}\bullet\overrightarrow{H_d}V \qquad (2.24)$$

Eq. 2.23 and 2.24 hold for micromagnetic cells, because the magnetization inside a cell is uniform. Magnetostatic interaction is a long range interaction that spans all cells

in a magnetic sample. Every spin interacts with all spins in a sample, including itself. At a distance, the pair-wise demag interaction can be approximated by dipole-dipole interaction. The demagnetizing field contribution from spin j to spin i can always be expressed as the dot product of a demag tensor that depends on the relative position $R = r_j - r_i$ and the magnetization of spin j. For instance, the demagnetizing tensor for dipole-dipole approximation is given by:

$$\widetilde{N(X,Y,Z)_{i,j}} = -\frac{3t}{4p R^5}\begin{bmatrix} X^2 - R^2/3 & XY & XZ \\ XY & Y^2 - R^2/3 & YZ \\ XZ & YZ & Z^2 - R^2/3 \end{bmatrix} \qquad (2.25)$$

where X, Y, Z are the relative Cartesian coordinates and R is the distance between spins j and i.

The demagnetizing field contribution from spin j to spin i is given by:

$$\overrightarrow{H_{di,j}} = \widetilde{N(X,Y,Z)_{i,j}} \bullet \overrightarrow{M_j} = \frac{3\vec{R}\left(\vec{m}_j \bullet \overrightarrow{R_{ij}}\right) - \vec{m}\left|\overrightarrow{R_{ij}}\right|^2}{4p\left|\overrightarrow{R_{ij}}\right|^5} \qquad (2.26)$$

The self-demagnetizing tensor is simple. Since inside a uniformly magnetized sphere, $\vec{H} = -\vec{M}/3$, the self-demagnetizing tensor is:

$$\widetilde{N(0,0,0)_{i,i}} = \frac{1}{3}\begin{bmatrix} 1 & 0 & 0 \\ 0 & 1 & 0 \\ 0 & 0 & 1 \end{bmatrix} \qquad (2.27)$$

While a more favorable fast multi-pole demagnetizing formula[33,34] is utilized in some calculations, the most accurate demagnetizing tensor is that given by Andrew J. Newell[35]. Given x, y, z the coordinate differences between two spins and

$\triangle x$, $\triangle y$, $\triangle z$ the size of a rectangular cell, the diagonal component N_{xx} of demagnetizing tensor is calculated as follows:

$$N_{xx}(X,Y,Z)=\frac{1}{4pV}\left[2F(X,Y,Z)-F(X+\triangle x,Y,Z)-F(X-\triangle x,Y,Z)\right] \quad (2.28)$$

where $V=\triangle x\triangle y\triangle z$ is the volume of a cell.

The function F is given by:

$$F(X,Y,Z)=F_1(X,Y+\triangle y,Z+\triangle z)-F_1(X,Y,Z+\triangle z)-F_1(X,Y+\triangle y,Z)+F_1(X,Y,Z) \quad (2.29)$$

where the function F_1 is given by:

$$F_1(X,Y,Z)=F_2(X,Y,Z)-F_2(X,Y-\triangle y,Z)-F_2(X,Y,Z-\triangle z)+F_2(X,Y-\triangle y,Z-\triangle z) \quad (2.30)$$

where the function F_2 is given by:

$$F_2(X,Y,Z)=f(x,y,z)-f(x,0,z)-f(x,y,0)+f(x,0,0) \quad (2.31)$$

where the function f is given by:

$$\begin{aligned} f(x,y,z)=&\frac{y}{2}\left(z^2-x^2\right)f\left(\frac{y}{\sqrt{x^2+z^2}}\right)+\frac{z}{2}\left(y^2-x^2\right)f\left(\frac{z}{\sqrt{z^2+y^2}}\right)\\ &-xyz\tan^{-1}\left(\frac{yz}{xR}\right)+\frac{1}{6}\left(2x^2-y^2-z^2\right)R \end{aligned} \quad (2.32)$$

where $f(x)=\sin^{-1}x=\ln\left(x+\sqrt{1+x^2}\right)$ and $R=\sqrt{x^2+y^2+z^2}$.

Diagonal components N_{yy} and N_{zz} can be calculated by permuting x, y and z.

The off-diagonal component N_{xy} is given by:

$$N_{xy}(X,Y,Z)=\frac{1}{4pV}\begin{bmatrix}G(X,Y,Z)-G(X-\triangle x,Y,Z)\\ -G(X,Y+\triangle y,Z)+G(X-\triangle x,Y+\triangle y,Z)\end{bmatrix} \quad (2.33)$$

where the function G is given by:

$$\begin{aligned} G(X,Y,Z) = {} & G_1(X,Y,Z) - G_1(X,Y-\triangle y,Z) \\ & -G_1(X,Y,Z-\triangle z) + G_1(X,Y-\triangle y,Z-\triangle z) \end{aligned} \tag{2.34}$$

where the function G_1 is given by:

$$\begin{aligned} G_1(X,Y,Z) = {} & G_2(X+\triangle x,Y,Z+\triangle z) - G_2(X+\triangle x,Y,Z) \\ & -G_2(X,Y,Z+\triangle z) + G_2(X,Y,Z) \end{aligned} \tag{2.35}$$

where the function G_2 is given by:

$$G_2(x,y,z) = g(x,y,z) - g(x,y,0) \tag{2.36}$$

where function g is given by:

$$\begin{aligned} g(x,y,z) = {} & (xyz) f\left(\frac{z}{\sqrt{x^2+y^2}}\right) \\ & + \frac{y}{6}\left(3z^2-y^2\right) f\left(\frac{x}{\sqrt{y^2+z^2}}\right) + \frac{x}{6}\left(3z^2-x^2\right) f\left(\frac{y}{\sqrt{x^2+z^2}}\right) \\ & - \frac{x^3}{6}\tan^{-1}\left(\frac{xy}{zR}\right) - \frac{xy^2}{2}\tan^{-1}\left(\frac{xz}{yR}\right) - \frac{zx^2}{2}\tan^{-1}\left(\frac{yz}{xR}\right) - \frac{xyR}{3} \end{aligned} \tag{2.37}$$

Other off-diagonal components can be calculated by exchanging or permuting x, y and z.

The symmetry properties of the demagnetizing tensor are summarized in the following. It is easy to see from Eq. 2.32 and Eq. 2.37.

$$\begin{aligned} & N_{xx}(X,Y,Z) = N_{xx}(-X,Y,Z) = N_{xx}(X,-Y,Z) = N_{xx}(X,Y,-Z) \\ & = N_{xx}(-X,-Y,Z) = N_{xx}(-X,Y,-Z) = N_{xx}(X,-Y,-Z) = N_{xx}(-X,-Y,-Z) \\ & N_{xy}(X,Y,Z) = -N_{xy}(-X,Y,Z) = -N_{xy}(X,-Y,Z) = N_{xy}(X,Y,-Z) \\ & = N_{xy}(-X,-Y,Z) = -N_{xy}(-X,Y,-Z) = -N_{xy}(X,-Y,-Z) = N_{xy}(-X,-Y,-Z) \end{aligned} \tag{2.38}$$

An important conclusion from Eq. 2.38 is $N(X,Y,Z) = N(-X,-Y,-Z)$, which

means the demagnetizing tensor is symmetric in space for spins i and j, and $N_{xy} = N_{yx}$, which reduces the number of components needed to be calculated.

Demagnetizing tensors depend on the relative position between interacting spins only. They can be calculated once and used repeatedly.

The demagnetizing field of spin i is the sum over all spins:

$$\begin{aligned} \overrightarrow{H_{d,i}} &= \sum_{j=1}^{N} -N_{ij}\left(x_j - x_i, y_j - y_i, z_j - z_i\right)\overrightarrow{M_j} \\ \overrightarrow{h_{d,i}} &= -\sum_{j=1}^{N} N_{ij}\left(x_j - x_i, y_j - y_i, z_j - z_i\right)\frac{M_{s,j}}{M_{s,i}}\overrightarrow{m_j} \end{aligned} \tag{2.39}$$

The demag energy of spin i is given by:

$$\begin{aligned} E_{d,i} &= \sum_{j=1}^{N} \frac{1}{2}\mu_0 \widetilde{N_{ij}}\overrightarrow{M_j}\bullet\overrightarrow{M_i}V \\ e_{d,i} &= \frac{1}{2}\sum_{j=1}^{N} \frac{M_{s,j}}{M_{s,i}}\widetilde{N_{ij}}\overrightarrow{m_j}\bullet\overrightarrow{m_i} \end{aligned} \tag{2.40}$$

2.3.4 Applied Field

In the context of micromagnetic simulations, owing to the small size of the specimen, the applied field is usually the same for all spins. However, for a specimen with multiple materials, spins of different materials have different reduced applied field. The dimensionless applied field of spin i is given by:

$$\overrightarrow{h_{z,i}} = \frac{\overrightarrow{H_{z,i}}}{M_{s,i}} \tag{2.41}$$

and the associated dimensionless Zeeman energy density is given by:

$$e_z = \frac{-\mu_0 \overrightarrow{H_{z,i}}\bullet\overrightarrow{M_i}V}{\mu_0 M_s^2 V} = -\overrightarrow{h_{z,i}}\bullet\overrightarrow{m_i} \tag{2.42}$$

Micromagnetics simulations are often used to calculate rate-independent

hysteresis loops. By rate-independent it is implied that, after the applied field changed, the magnetic system is allowed more than sufficient time to reach a metastable state through Barkhausen jumps.

2.3.5 Thermal Fluctuation Field

Thermal fluctuation is assumed to be due to random Gauss white noise. Thermal fluctuation is not correlated in time, or in space. The thermal fluctuation field H_t follows the statistic equation: $\left\langle H_{t,i}^{k}, H_{t,j}^{l} \right\rangle = 2\frac{a\,k_B T}{\left(1+a^2\right) m_0 g\, M_s V} d_{ij} d_{kl} d\left(t, t'\right)$ where i and j denote the cells at location i and j, k and l equals to x, y or z and t and t' denote different time. The magnitude of the random oriented thermal field of a cell is estimated as $h\sqrt{2\frac{a\,k_B T}{\left(1+a^2\right) m_0 g\, M_s V \Delta t}}$ where h is a normal Gaussian random number, Δt is the duration of effect and V is the volume of a cell. In dimensionless form, the thermal effective field in evaluation of the LLG Equation is given by $h\sqrt{2\frac{a\,k_B T}{\left(1+a^2\right) m_0 M_s^2 V \Delta t}}$, where $\Delta t = g M_s \Delta t$ is the dimensionless time. For a detail discussion of the strength of thermal fluctuation field, see the appendix.

2.4 Integration of LLG Equation

The LLG equation, Eq. 2.10, gives the evolution of the magnetization. The magnetization depends on the external applied field and other field terms implicitly depend on the magnetization. The magnetization configuration at a given time is

calculated by integrating the LLG equation $\overrightarrow{M}\left(t,\overrightarrow{H_z}\right)=\int_o^t \frac{dM}{dt}dt$ starting from an initial state. The two common initial configurations are random initial spin configuration and saturated initial spin configuration. Another commonly encountered initial configuration is the vortex configuration. In a discretized form, time is separated from space variables and integrated by accumulating time steps. This can be done numerically though iteration until convergence criteria are met. A widely applied convergence criterion is the magnitude of magnetic torque $t=\left|\vec{m}\times\vec{h}\right|$. When all spins are exactly coincide with their local effective field, $t=0$. Other criteria include the maximum angle between spins and their effective fields and the energy change of the entire system. Due to the complicity of the magnetic energy surface, many metastable states may have similar energies and the energy curve may be very flat, especially when the system is close to a local minimum. For this reason, the maximum torque criterion and the maximum angle criterion are equivalent and are several levels higher in accuracy than the energy change criterion.

Eq. 2.10 can be written into discretized form $\frac{\Delta\vec{m}}{\Delta t}=-\vec{m}\times\vec{h}-\overrightarrow{a\,m}\times\left(\vec{m}\times\vec{h}\right)$. The simplest integration method is Euler's method in the following form:

$$\overrightarrow{m^{t+\Delta t}}=\overrightarrow{m^t}+\Delta t\frac{d\overrightarrow{m^t}}{dt} \qquad (2.43)$$

In Eq. 2.43 the time increment Δt can be fixed or adaptive. Δt is called step size throughout this document. Since the magnitude of magnetization is constant, a normalization or projection, as called by some authors, must be followed:

$$\overrightarrow{m^{t+\Delta t}} = \frac{\overrightarrow{m^t} + \Delta t \frac{d\overrightarrow{m^t}}{dt}}{\left| \overrightarrow{m^t} + \Delta t \frac{d\overrightarrow{m^t}}{dt} \right|} \tag{2.43}$$

The normalization factor is given by:

$$\left\{ \left[m + \Delta t \left(-m \times h - a\, m \times (m \times h) \right) \right] \bullet \left[m + \Delta t \left(-m \times h - a\, m \times (m \times h) \right) \right] \right\}^{1/2}$$

$$= \left\{ (m \bullet m) + \Delta t^2 \left[(m \times h) \bullet (m \times h) + a^2 \left(m \times (m \times h) \right) \bullet \left(m \times (m \times h) \right) \right] \right\}^{1/2}$$

$$= \left\{ (m \bullet m) + \Delta t^2 \left[(m \bullet m)(h \bullet h) - (m \bullet h)(m \bullet h) + a^2 \left((m \bullet h) m - (m \bullet m) h \right) \bullet \left((m \bullet h) m - (m \bullet m) h \right) \right] \right\}^{1/2}$$

$$= \sqrt{1 + \Delta t^2 \left[|h|^2 \sin^2 q + a^2 \left(|h|^2 - |h|^2 \cos^2 q \right) \right]}$$

$$= \sqrt{1 + \Delta t^2 |h|^2 \left[\sin^2 q + a^2 \sin^2 q \right]}$$

$$\approx \sqrt{1 + \left(1 + a^2 \right) \sin^2 q\, \Delta t^2 |h|^2}$$

Assuming that the effective field is steady, the old field can be used to approximate the updated field in the calculation of the updated torque:

$$
\begin{aligned}
&\overrightarrow{t^{t+\Delta t}} = \overrightarrow{m^{t+\Delta t}} \times \overrightarrow{h^{t+\Delta t}} \approx \overrightarrow{m^{t+\Delta t}} \times \overrightarrow{h^{t}} \\
&= \frac{1}{\sqrt{1+\left(1+a^2\right)\sin^2 q\,\Delta t^2 \left|h\right|^2}} \left(\overrightarrow{m^t} - \Delta t \left(\overrightarrow{m^t} \times \overrightarrow{h^t} + a\, \overrightarrow{m^t} \times \left(\overrightarrow{m^t} \times \overrightarrow{h^t} \right) \right) \right) \times \overrightarrow{h^t} \\
&= \frac{1}{\sqrt{1+\left(1+a^2\right)\sin^2 q\,\Delta t^2 \left|h\right|^2}} \left(\overrightarrow{m^t} - \Delta t a\, \overrightarrow{m^t} \times \left(\overrightarrow{m^t} \times \overrightarrow{h^t} \right) \right) \times \overrightarrow{h^t} \\
&= \frac{1}{\sqrt{1+\left(1+a^2\right)\sin^2 q\,\Delta t^2 \left|h\right|^2}} \left(\overrightarrow{m^t} - \Delta t a \left(\left(\overrightarrow{m^t} \bullet \overrightarrow{h^t} \right) \overrightarrow{m^t} - \left(\overrightarrow{m^t} \bullet \overrightarrow{m^t} \right) \overrightarrow{h^t} \right) \right) \times \overrightarrow{h^t} \\
&= \frac{1}{\sqrt{1+\left(1+a^2\right)\sin^2 q\,\Delta t^2 \left|h\right|^2}} \left(\overrightarrow{m^t} - \Delta t a \left(\overrightarrow{m^t} \bullet \overrightarrow{h^t} \right) \overrightarrow{m^t} \right) \times \overrightarrow{h^t} \\
&= \frac{1-\Delta t a \left(\overrightarrow{m^t} \bullet \overrightarrow{h^t} \right)}{\sqrt{1+\left(1+a^2\right)\sin^2 q\,\Delta t^2 \left|h\right|^2}} \overrightarrow{m^t} \times \overrightarrow{h^t} = \frac{1-\Delta t a \left(\overrightarrow{m^t} \bullet \overrightarrow{h^t} \right)}{\sqrt{1+\left(1+a^2\right)\sin^2 q\,\Delta t^2 \left|h\right|^2}} \overrightarrow{t^t} \\
&= \frac{1-\Delta t a \cos q \left|h\right|}{\sqrt{1+\left(1+a^2\right)\sin^2 q\,\Delta t^2 \left|h\right|^2}} \overrightarrow{t^t} = \frac{1-\Delta t a \left|h_{\parallel}\right|}{\sqrt{1+\left(1+a^2\right)\Delta t^2 \left|h_{\perp}\right|^2}} \overrightarrow{t^t}
\end{aligned}
\qquad (2.44)
$$

From Eq. 2.44, it is clear that the Euler's method always converges provided that the initial state is close enough to the final state. The larger the step size, the faster the method converges. A smaller initial step size is given when the iterations start, but a larger step size can be used when the maximum magnitude of torques is less than a predefined threshold.

Defining $\left(\frac{dm}{dt} \right)^{t+\Delta t/2} = \frac{m^{t+\Delta t} - m^t}{\Delta t} + O\left(\Delta t^2\right)$ and $m^{t+\Delta t/2} = \frac{m^{t+\Delta t} + m^t}{2} + O\left(\Delta t^2\right)$. Eq. 2.10 can be rewritten as $m^{t+\Delta t} + \frac{\Delta t}{2} m^{t+\Delta t} \times h^{t+\Delta t/2} = m^t - \frac{\Delta t}{2} m^t \times h^{t+\Delta t/2}$, where $h^{t+\Delta t/2} = \frac{3}{2}\left(h^t + a\, m^t \times h^t \right) - \frac{1}{2}\left(h^{t-\Delta t} + a\, m^{t-\Delta t} \times h^{t-\Delta t} \right)$ is calculated from two previous steps. This way the magnitude of magnetization is conserved and no normalization is required[31]

The Runge-Kutta method has been extensively employed in numerical integration

of ordinary differential equations in the form of $\frac{dy}{dx} = f(t, y)$, $y_0 = y(t_0)$. Suppose the system is currently at $f(t_n, y_n)$, the goal is to move forward to the next state $f(t_n + h, y_{n+1})$, where h is the time interval. The second order Runge-Kutta's method is carried out by advancing twice at half step size and the forth order Runge-Kutta's method is carried out as follows:

$$k_1 = hf(t_n, y_n)$$
$$k_2 = hf\left(t_n + \frac{h}{2}, y_n + \frac{k_1}{2}\right)$$
$$k_3 = hf\left(t_n + \frac{h}{2}, y_n + \frac{k_2}{2}\right)$$
$$k_4 = hf(t_n + h, y_n + k_3)$$

and the value of the next step is given by:

$$y_{n+1} = y_n + \frac{h}{6}(k_1 + 2k_2 + 2k_3 + k_4) \tag{2.45}$$

The local truncation error is given by:

$$LTE = \frac{2^n (y_{-2h} - y_{-h})}{2^n - 1} \tag{2.46}$$

where y_{-h} and y_{-2h} are the approximate values calculated by advancing h or twice at $h/2$ and n is the order of the method. Eq. 2.46 can be used to adapt the step size. Since the truncation error is proportional to h^{n+1}, if we need the truncation error to be less than a threshold d, then $h_{new} = q\left|\frac{d}{LTE}\right|^{n+1} h_{old}$, q is a fractional satisfaction factor.

The Runge-Kutta method is more accurate and more stable than Euler's method. This method also converges faster than Euler's method.

Chapter 3 Micromag - The Distributed Micromagnetics Program on the Web

3.1 Micromagnetics Software

Several software packages are available to perform micromagnetic simulation. These software packages fall into two categories, namely the finite element approach and the finite difference approach. The finite element approach discrete the energy equation, Eq. 2.1, with meshes of various shape, while the finite difference approach generally solves the discretized LLG equation, Eq. 2.10, on a rectangular grid.

OOMMF (Object Oriented Micromagnetics Framework) is a public-domain micromagnetics code from the National Institute of Standards and Technology (NIST). Its graphical user interface is written in Tck/Tk and computing engine is written in C++. It models three-dimensional rectangular multi-component magnetic samples.

JaMM (Java MicroMagnetics) is a freeware program written by Professor Scott Whittenburg at the University of New Orleans. It is a distributed three-dimensional micromagnetics program. It has a graphical front-end, a message passing server and a separate micromagnetics compute node. Multiple GUIs running on a network can execute jobs simultaneously on multiple copies of the compute node. The program provides visualization of the results.

Commercial software includes MagFEM3D, a finite element method program that uses VRML for graphical output; LLG Micromagnetics Simulator, a three-dimensional

simulation tool integrated graphics that runs on Windows platform; and MagSimus from Euxine, a tool that simulates recording heads, magnetic memories and magnetoresistives sensors.

Micromag is the micromagnetics program produced with this research work. It is the first web micromagnetics program which is completely based on Extensible Markup Language, Java 2 Enterprise Edition, Microsoft .NET and Web services technology. Micromag can handle magnetic samples with multiple materials and arbitrary geometric shapes and can visualize output in web based scalable vector graphics. Micromag prefers input parameters in SI unit system. Regardless of the input unit system, the output of the program is reported in SI units.

3.2 Micromag XML Schema

Micromag uses Extensible Markup Language (XML) to define input data, report results and exchange data. XML data is stored in a database or exchanged among multiple processing units as a compressed binary byte array, or as text document in a file system. An XML schema is used to specify the contents and formats of XML data. Micromag data structures and auxiliary data structures are defined in the XML schema. Java source code for the data structures are compiled from the schema using Java XML Bounding (JAXB) with customization extension. The same schema is also compiled into other programming languages, such as C# and Visual Basic.Net. Data stored in XML format is guaranteed language independence through schema validation. This mechanism provides the basis of distributed programming.

Vector: vector is the foundation of the program. A vector has three components,

corresponding to three dimensional calculations.

Location: owing to the finite difference discretization, location has three non-negative integer components, corresponding to three Cartesian coordinates.

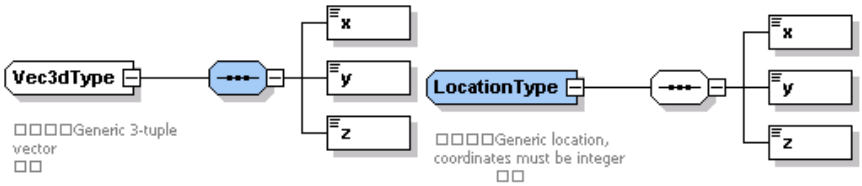

Schema 1. XML schema for vector and location

Material: material control parameters are material's name, anisotropy type, either uniaxial or cubic, first order anisotropy constant, $K_1(J/M^3)$, second anisotropy constant $K_2(J/M^3)$, self exchange constant $A(J/M)$, saturation magnetization $M_s(A/M)$, damping coefficient α and user specified display color. Exchange coupling between different materials is specified by coupling exchange constant $A_{ij}(J/M)$.

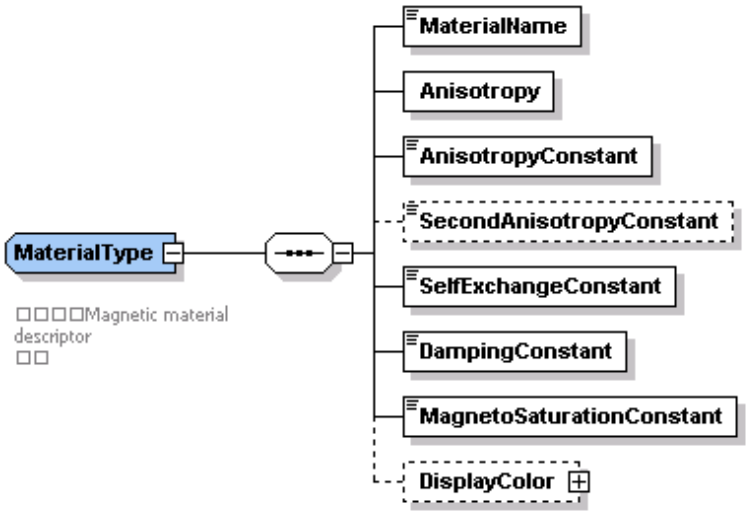

Schema 2. XML schema for material

Sample: a magnetic sample consists of one or more regions.

Region: a region is a group of cells with common properties. Every region associates to a unique material. A material can span one or more regions. All cells in a region have parallel easy axis and secondary easy axis. Initial spin configurations of the cells in a region can be uniform, random or in vortex form. A region is analytically defined by a list of constraints, each of which is a boolean expression that compares a constant with a quadratic homogeneous polynomial in the form of $C_{2x}x^2 + C_{2y}y^2 + C_{2z}z^2 + C_{xy}xy + C_{xz}xz + C_{yz}yz + C_x x + C_y y + C_z z$. In the polynomial, x, y and z are the coordinates for a cell. If all the expressions are true, *i.e.*, all the constraints are satisfied, the cell at the location belongs to the region.

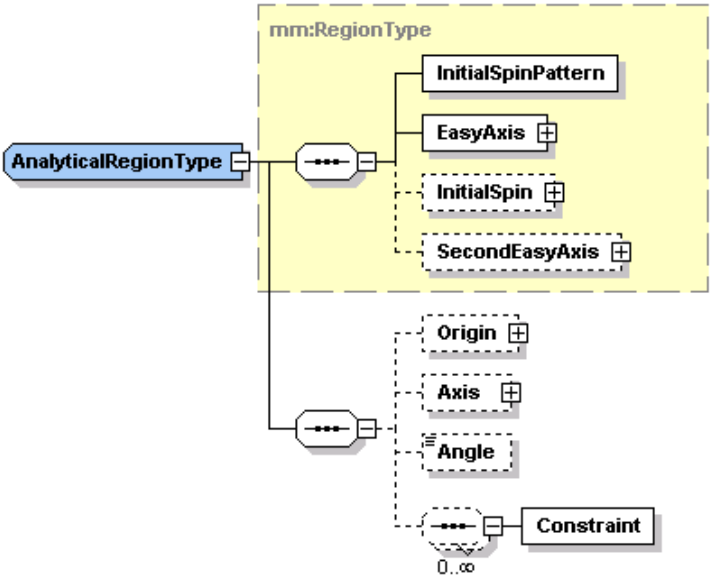

Schema 3. XML schema for analytical region

Cell: a cell has a location, a spin vector and a list of neighbor cells. Every cell associates to a region. Uniaxial cell has an easy axis. Cubic cell has an additional second easy axis that's orthogonal to the principle easy axis. The third easy axis is assigned by the program.

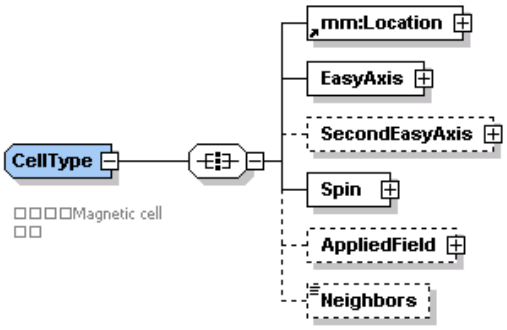

Schema 4. XML schema for cell

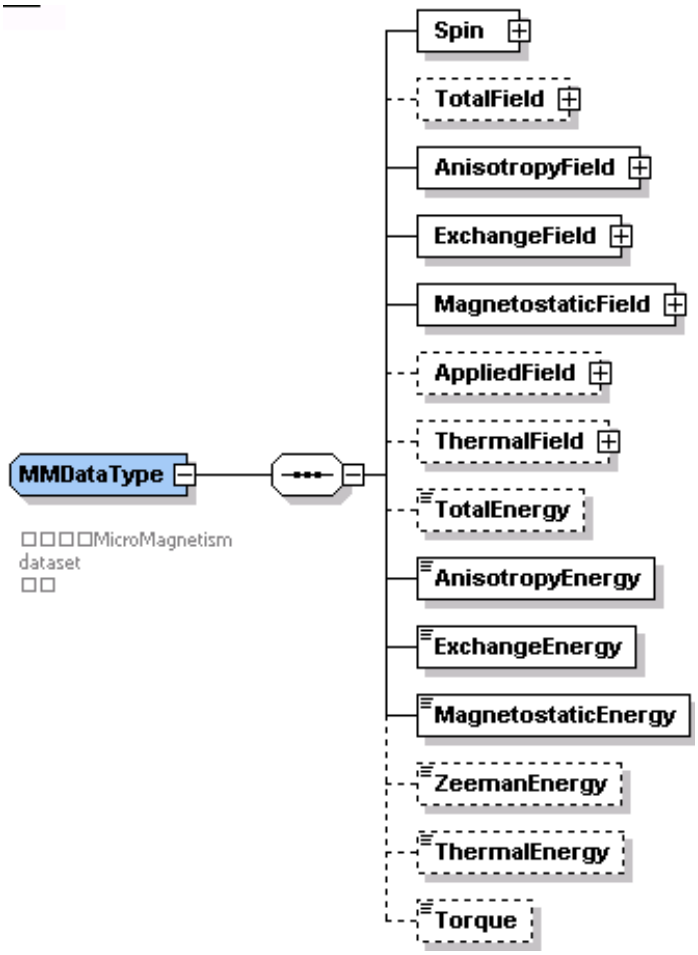

Schema 5. XML schema for Micromag data block

MMData: mmdata stores output of the program. Every entity, a cell, a region or the entire sample, is associated with an MMData structure. Total effective field *H* and its

components H_a, H_d, H_e, H_z and the reserved thermal fluctuation field H_t, there corresponding energies E, E_a, E_d, E_e, E_z and E_t are stored in the structure along with the spin vector and magnitude of the torque of a cell in a metastable state.

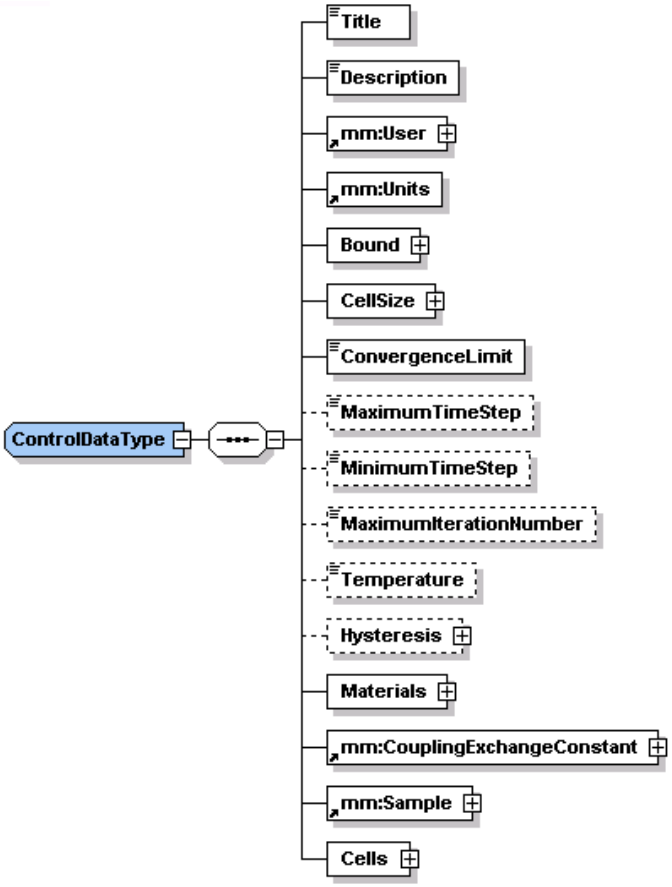

Schema 6. XML schema of ControlData

ControlData: ControlData contains other simple program control parameters. Bound is an instance of the location object that defines the three dimensions of the bounding box of a sample. CellSize is an instance of the vector object that defines the three dimensions of a rectangular grid. Hysteresis defines a sequence of applied fields, each of which is expressed as a vector. ConvergenceLimit defines the convergence criterion. The program uses the dimensionless maximum magnitude of torque as the

indication of equilibrium. The default convergence limit value is $\max\left(\left|\vec{m}\times\vec{h}\right|\right) < 10^{-5}$. MaximumTimeStep and MinimumTimeStep specify the range of dimensionless time step for every integration step. A typical range is $10^{-4} < \Delta t < 0.2$. Temperature specifies the temperature of a magnetic system. If temperature is zero, no thermal fluctuation field is computed.

3.3 Micromag Structure

Micromag program consists of seven packages: MicromagSchema, MicromagUtil, MicromagDB, MicromagJSP, MicromagService, MicromagRuntime and MicromagSVG.

MicromagSchema is a Java package compiled from the XML schema. It provides functions such as marshalling Java class objects into XML stream and unmarshalling XML stream into Java class objects. This package also does unit conversion between SI system and intrinsic dimensionless unit system. A similar C# package compiled from the XML schema is available for C# web services.

MicromagUtil is a Java package that provides the mathematic operations. This package includes complex routines, Fast Fourier Transform routines, magnetostatic tensor routines and data compression/decompression routines.

MicromagDB is a Java package provides communication with database. Several tables are defined in database. Their corresponding data access objects are implemented with Enterprise Java Beans (EJB) and wrapped as Java web services. The web services proxy provides table management operations through XML Remote Procedure Call (SOAP-RPC) invocations in network.

MicromagJSP is composed of several Java Server Pages and Java Servlets. It is

the web based user interface for Micromag. It provides functions for users to define every detail of a micromagnetics computing task, modify, submit and retrieve results of the computing task. This package handles concurrent requests from multiple users.

MicromagRuntime is a Java package that solves the LLG equation. It parses the program control configurations provided in a XML format text file, initializes computing tasks, calculates all field and energy terms, evaluates LLG equation, integrates evolution time steps, performs hysteresis loop and reports computing results and logs.

MicromagService is a sub-package of the MicromagRuntime package. It provides web services for the magnetostatic field term calculation and is deployed separately in web servers. A similar package in C# is available for C# web services for magnetostatic field and energy calculation.

MicromagSVG is composed of server XML Stylesheet Transformer (XSLT) and XML Scalable Vector Graphics (SVG) files as well as Javascript source files embedded in HTML pages. It is a post-processing tool that provides transformation and visualization of computation results in web graphics. MicromagSVG can display simulation results in an interactive way. Vector variables are displayed as an arrow scaled by their normalized magnitude. The composite RGB color of vector variables are calculated from their component values, with red represents x component, green represents y component and blue represents z component. Scalar variables are displayed as squares whose sizes are scaled to their normalized magnitude. Scalar variables are rendered in the user defined colors of their associated materials. The opacity of each cell is scaled to the normalized magnitude of the variable it is rendering. Figure1 illustrates a SVG graphics of the vortex state of a cubic magnetic sample.

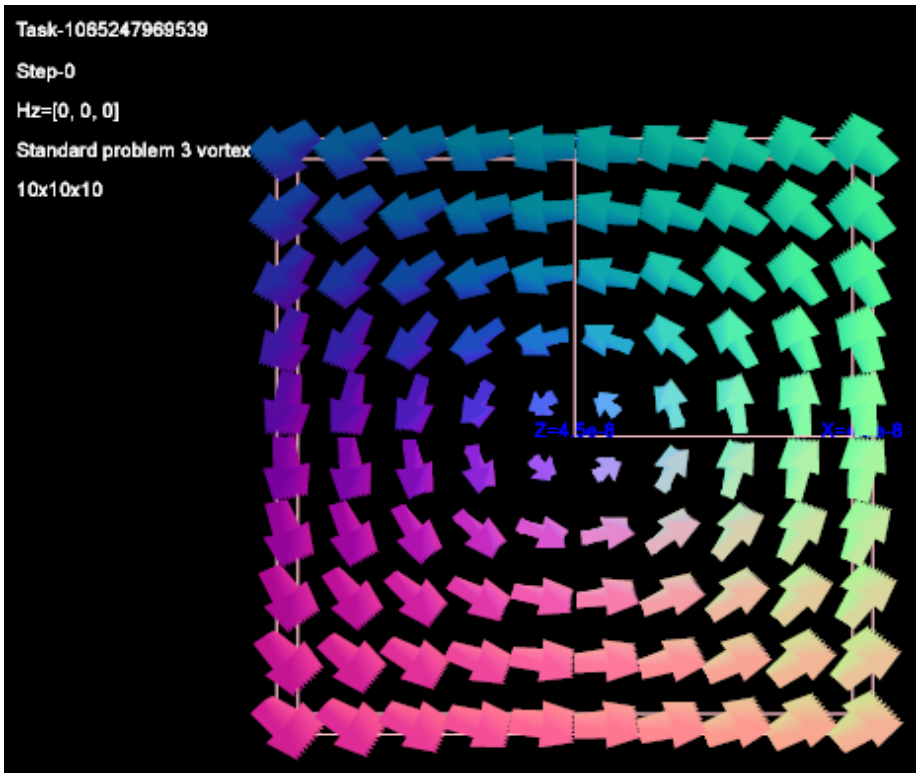

Figure 1. Vortex state of cubic sample in problem#3

MicromagDB, MicromagService and MicromagDB are deployed in Java Application Servers while the corresponding C# packages are deployed in Internet Information Servers. Java packages are platform independent and work for all operating systems that supporting Java. C# packages work for Microsoft Windows only. MicromagRuntime is a separate Java package that runs outside an application server. It retrieves computing tasks from a priority task queue in the application server and does the simulations. Users can download this package to perform computing locally.

The complexities to carry out individual field terms are different. The applied field is given and does not need computation. The anisotropy field is local and therefore its complexity is $O(N)$ where N is the total number of cells in a magnetic sample. The exchange field sums over the nearest neighbor only while the maximum number of

neighbors is 6 for three dimensional calculations (4 for 2D model). The complexity is also $O(N)$. The most intensive field term is the pair-wise demag term. Its complicity is $O(N^2)$. Since the demag field in its entirety can be expressed as a convolution of the demag tensor matrix and the spin vector matrix, Fast Fourier Transformation treatment reduces its complexity to $O(N \log N)$. With some approximations, a more flexible Fast Multiple Method (FMM)[33,34] can further reduce its complicity to leaner. The FMM method will be implemented in possible future work. Evaluating the demag field also demands large memory capacity and limits the scale of micromagnetics simulations. The web services technique is exploited to solve this problem. In the web services mechanism, the master computing node only keeps a handle of the demag service proxy, the CPU demanding and memory demanding computing tasks are distributed among scalable number of heterogeneous service nodes. Thus, larger simulation tasks are able to be performed. With the help of multithreading, high performance parallel computing for the demag term is achieved. Due to the heavy overhead of network transportation, only very large computing tasks should be distributed. Moderate tasks are still preformed locally. Similarly, to avoid overhead of FFT, demag fields for very small computing tasks are calculated directly. Options for direct, local or distributed computing of the demag field are provided to the program user.

3.4 Program Verification

The micromagnetics modeling society provides standard micromagnetics problems to verify modeling programs. The specifications of standard problems are found at the National Institute of Standards and Technology. The URL of standard problems is

at **http://www.ctcms.nist.gov/~rdm/mumag.org.html.** Micromag has been tested against standard problems 3 and 4 for its performance on static and dynamic issues.

3.4.1 µ-mag Standard Problem 3

The domain configuration of a magnetic cube depends on its size. Two magnetic domain patterns exist for a magnetic cube, namely the flower state and the vortex state. In a flower state spins align approximately parallel while in a vortex state the spins form a closure domain. Small cube favors the flower state for its lower exchange energy at the expense of higher magnetostatic energy. Large cube favors the vortex state for its lower magnetostatic energy at the expense of higher exchange energy. At a certain size, the total energy of the flower state and the total energy of the vortex state are equal. The transition is expected to occur near the vicinity of $8l_{ex}$.

The parameters of the material are given in Table 1.

Table 1. Sample parameters of standard problem #3

$K_1\left(J/M^3\right)$	$A\left(J/M\right)$	a	$M_s\left(A/M\right)$
6.2831583×10^{4}	1.773528×10^{-12}	0.75	10^{6}
$K_m=\frac{1}{2}m_0M_s^2\left(J/M^3\right)$	$l_{ex}=\sqrt{A/K_m}\,(M)$	$a,b,c(nm)$	a/l_{ex}
6.2831583×10^{5}	5.3128×10^{-9}	45	8.47

The program is tested twice, first with 4.5nm cubic mesh then with 3nm cubic mesh. The vortex state is previously shown in Figure 1. Figure 2 gives the flower state of the same cube.

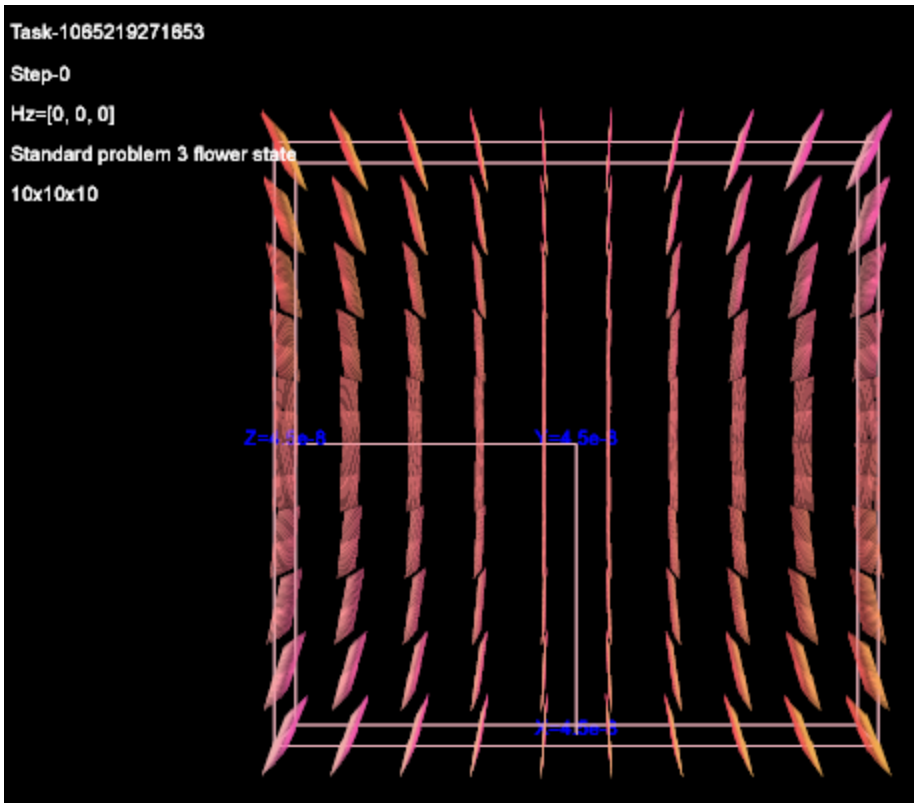

Figure 2. Flower state of cubic sample in problem#3

Table 2. Comparison table of standard problem#3

	Flower state					Vortex state				
	This work (3nm)	This work (4.5nm)	W. Rive	J. Martins	R. Hertel	This work (3nm)	This work (4.5nm)	W. Rive	J. Martins	R. Hertel
E(Km)	0.3043	0.30316	0.3027	0.3026	0.3049	0.3054	0.3007	0.03027	0.3026	0.3049
Ea(Km)	0.00558	0.005558	0.0056	0.0056	0.0052	0.05165	0.05133	0.0521	0.0521	0.0522
Ed(Km)	0.01754	0.01732	0.0177	0.0177	0.0158	0.1771	0.1721	0.1723	0.1724	0.1696
Ee(Km)	0.27977	0.2803	0.2794	0.2792	0.2839	0.0766	0.07720	0.0783	0.0780	0.083
Mx(Ms)	0.97108	0.971	0.971	0.971	0.973	0.3403	0.334	0.352	0.3516	0.351

The test results are compared with results submitted by other authors to the standard problem site, as summarized in Table 2. The energy and field term in Table 2 are reported in intrinsic units, *i.e.*, energies are relative to the magnetostatic

energy $K_m = \frac{1}{2} m_0 M_s^2$ and magnetizations are relative to the saturation magnetization, M_s. Good agreement between results of Micromag and other authors' results are found in Table 2. Furthermore, computations with 4.5nm cell size ($10\times10\times10$ mesh) and 3nm cell size ($15\times15\times15$) are in good agreement.

3.4.2 μ-mag Standard Problem 4

Standard problem #4 tests the dynamic performance of a micromagnetic modeling program. In this problem a rectangular magnetic sample with the parameters given in Table 3 is first saturated along the [1,1,1] direction, then the applied field is gradually removed to leave an initial "s" state. Successively two applied fields $H_{z1} = [-19576, 3421, 0]\left(\frac{A}{M}\right)$ and $H_{z2} = [-28250, -5013, 0]\left(\frac{A}{M}\right)$ are applied separately to two individual samples in "s" states to flip the spins in the samples. H_{z1} has a magnitude of $25mT$ and is applied at 170^0 counterclockwise to the positive x direction. H_{z2} has a magnitude of $36mT$ and is applied at 190^0 counterclockwise to the positive x direction. The fields are applied on the initial "s" state at time zero and the time series of the representative y components are plotted.

Table 3. Sample parameters of standard problem#4

$K_1\left(\frac{J}{M^3}\right)$	$A\left(\frac{J}{M}\right)$	a	$M_s\left(\frac{A}{M}\right)$
0	1.3×10^{-11}	0.02	8.0×10^5
Length(nm)	Depth(nm)	Thickness(nm)	H_{z1}(A/M)
500	125	3	[-19576,3421,0]
a(nm)	b(nm)	c(nm)	H_{z2}(A/M)
5	5	3	[-28250,-5013,0]

The entire time series of y component for H_{z1} and H_{z2} are given in Figure 3 and Figure 4. To compare with other authors' results, portions of the entire series up to 1ns are given in Figure 5 and Figure 7. Their comparisons are givens in Figure 6 and Figure 8.

Good agreements are found between the results of this work and the reported results. In particular, results of this work are closest to the OOMMF results reported by McMichael *et. al.* from NIST. By analyzing the public source code of OOMMF, it is found that both Micromag and 3D OOMMF adopted the same exchange field and magnetostatic field formula while other authors may have different approximations on these two field terms.

Also found from the figures is that Micromag does not accumulate the simulated time correctly. Micromag is 5% off in the accumulated time for the H_{z1} case and 8% off in the accumulated time for the H_{z2} case. This could be a bug in the Micromag program and will be solved in future work. Nonetheless, the error does not affect the correctness of stationary properties such as domain patterns, remanent states, coercivity and hysteresis loops. All conclusions drawn from the program results in this thesis are still reliable.

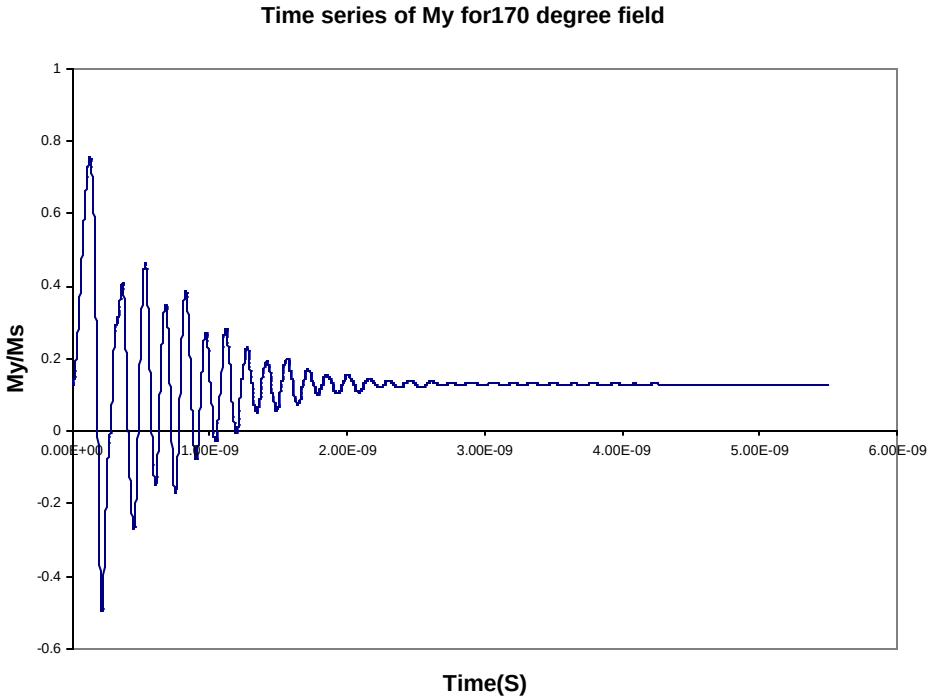

Figure 3. Time series of M_y for H_{z1}

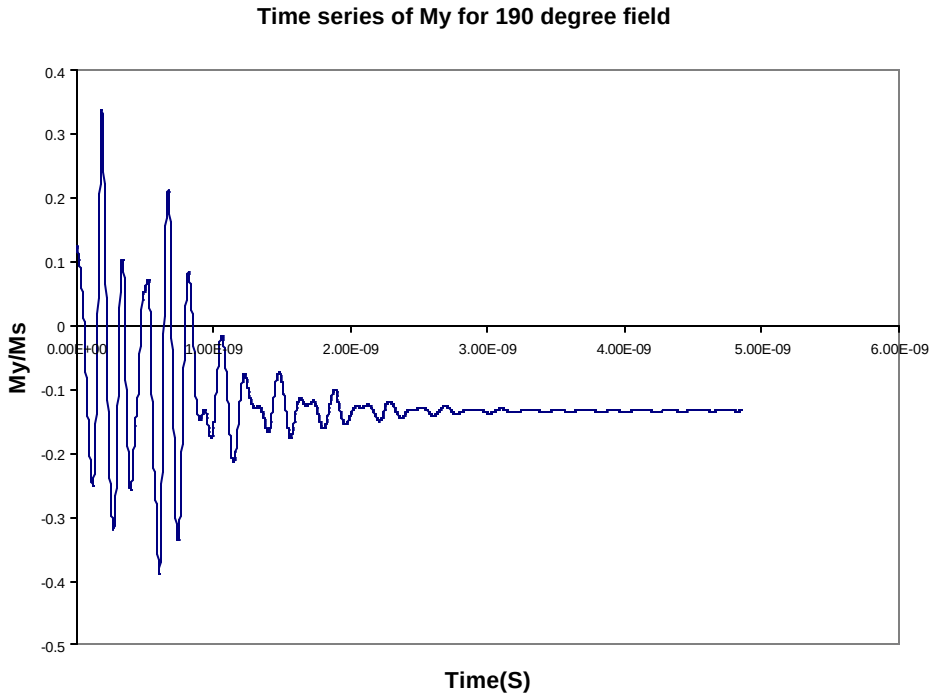

Figure 4. Time series of M_y for H_{z2}

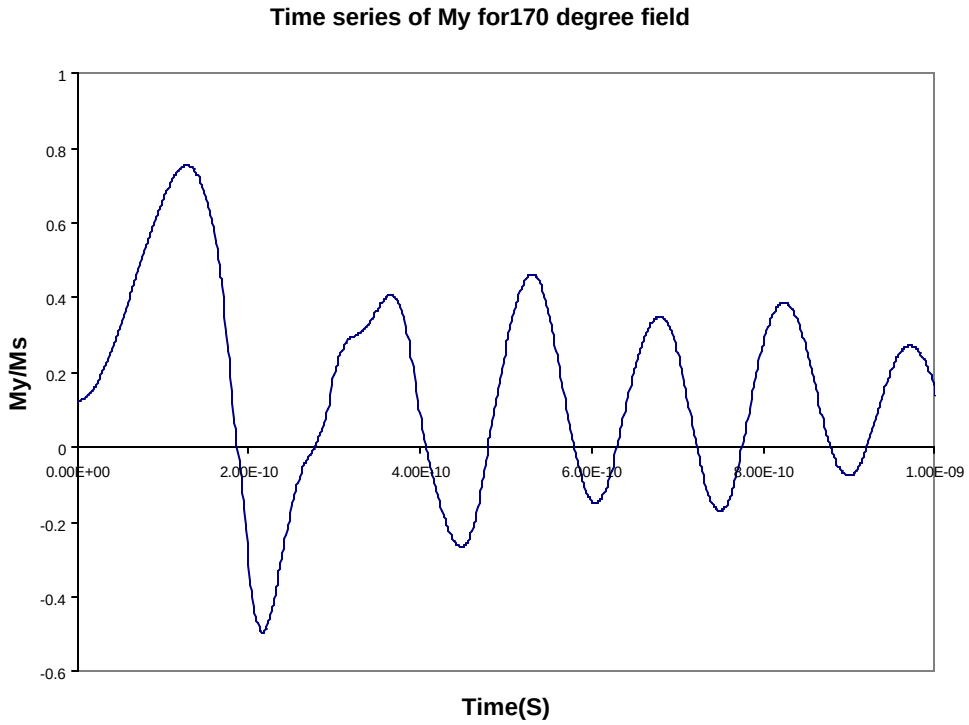

Figure 5. Time series of M_y for H_{z1}, up to 1ns

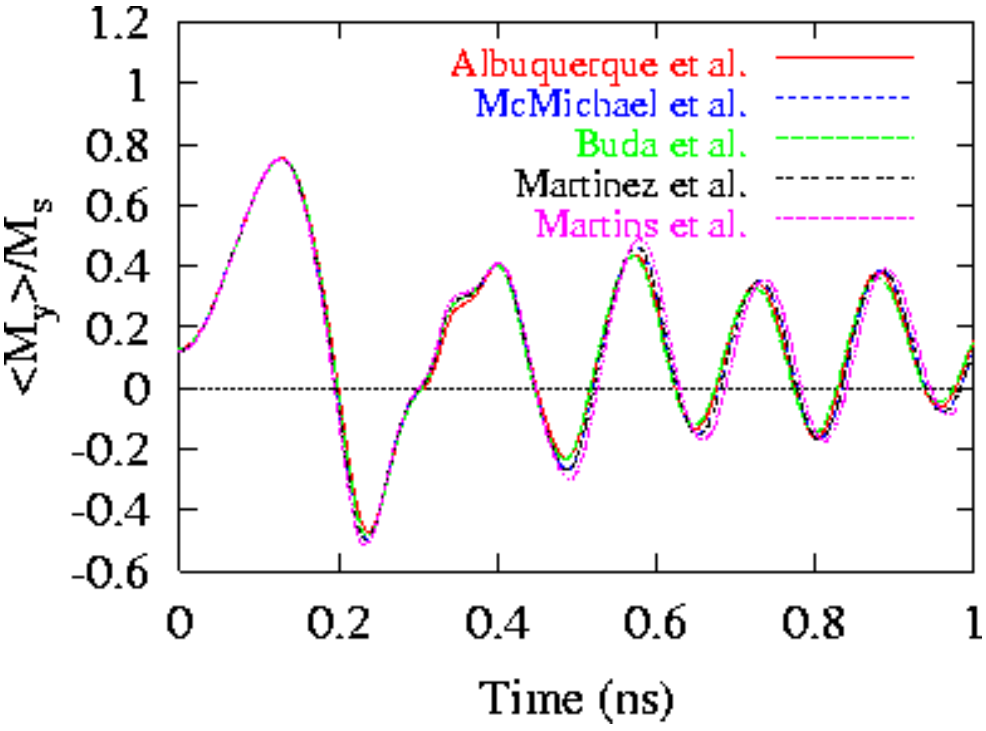

Figure 6. Reported time series of M_y for H_{z1}

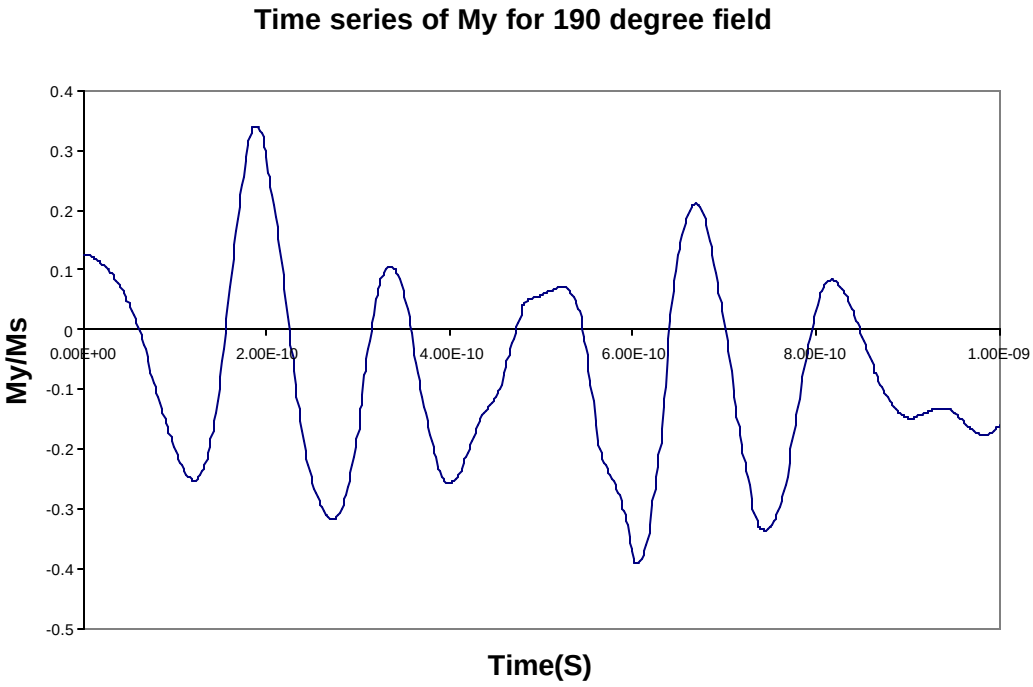

Figure 7. Time series of M_y for H_{z2}

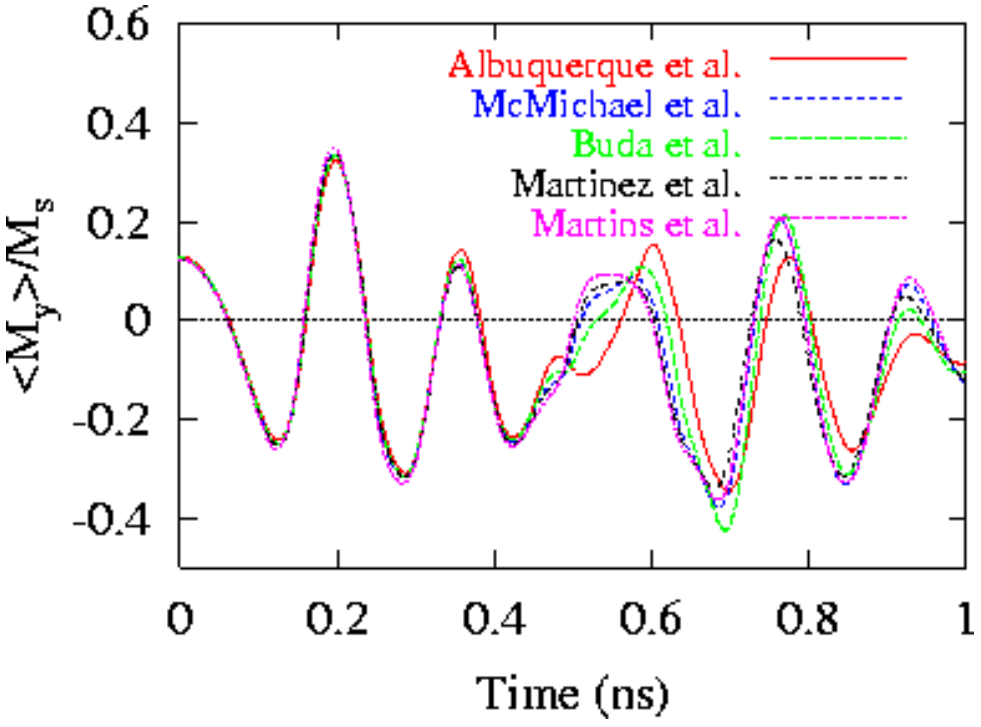

Figure 8. Reported time series of M_y for H_{z2}

Chapter 4 Tuning Reversal Behavior of Nano Permalloy Ring by Geometric Modification

4.1 Introduction

In order to achieve high density for magnetic information storage media, micron and deep submicron magnetic samples are necessary. For samples in this size range, their magnetic properties are drastically different from bulk properties. Properties such as remanent, coercivity and switching field are determined by the competition between anisotropy, magnetostatic and exchange energy. Shape effects play an important role in determining these properties through the magnetostatic interaction.

For Magnetic Random Access Memory (MRAM) applications, well defined remanent states and simple and repeatable switching processes are critical. On one hand, a small sample size is preferred to increase the possibility of coherent rotations. On the other hand, a small particle size reduces the thermal stability, because the stability depends exponentially on the volume of the magnetic particle.

Recently, ring elements have been proposed for MRAM applications.[36 ?38] Clockwise and counterclockwise vortices are observed at the remanent state and have been proposed in vertical MRAMs as mechanism for storing magnetic information. A "bit" is arranged as a stack of alternating hard magnetic material, non magnetic material and soft magnetic material. Magnetization reversal is conducted in the soft magnetic material rings. As a result, there has been a lot of research focused on soft magnetic

material, such as permalloy. Unlike the vortex state, which is favored for vertical switching, the two "onion" states observed in narrow rings are favored for in-plane switching.[39] With the help of defects formed during fabrication, fast switching through domain wall motion is observed. To create asymmetric defects, off-center rings are intentionally fabricated.

Sub-micron rings with various width and thickness have been fabricated and onion states are found by SEM and MEM to be stable for narrow rings with smaller thickness.[40] Vortex remanent states occur in both the vertical and in-plane reversal process.

Three switching mechanisms are observed for the ring elements.[41] The first is a single switching from an onion state to a reversed onion state. The second is a double switching from an onion state to a vortex and then from a vortex to a reversed onion state. The third is a triple switching that involves a vortex core forming. Due to the small size of the permalloy ring under our investigation, no vortex core forming is possible.

Problems that have been observed with ring-type storage devices are the wide switching field, the wide switching field distribution due to fabrication defects, and the poor reproducibility of the switching process.[39-41]

Attempts to overcome these problems by adding defects are unreliable, especially at elevated temperatures when local wall pining can be overcome by thermal excitations. However, asymmetry can be introduced in another way. Rather then unreliable defects, a narrow rectangular cross-tie can be added to a nano ring. Due to magnetostatic requirements, the spins in the cross-tie are forced to orient in the direction parallel to the tie, which we define as the X direction. The formation of vortex cores at the center of the

ring is thus eliminated and onion states exist under wider conditions. Also due to magnetostatic requirements, the spins in the tie flip with greater difficulty. This helps stabilize the two opposite onion states, denoted as bit “0” and bit “1”.

In this chapter, permalloy nano rings with cross-tie modifications are studied. The ring has an inner radius of 50nm, an outer radius of 100nm and a thickness of 5nm. It is discretized into 5nm cubic cells. To examine the effects of tie width, two cross-ties, with tie width of 10nm and 30nm, are added to the ring. The modifications introduce 40 or 120 cells into 980 discretized cells. Despite the small number of cells in the cross-ties, changes caused by them are significant.

Cross-ties break the symmetry and thus cause anisotropy effects. To examine the anisotropy effects, we have examined the hysteresis with applied field parallel to the tie direction, the hysteresis with applied field perpendicular to the tie direction and the hysteresis with applied field in diagonal direction. Obviously, the ring without the cross-tie behaves identically for all three applied field directions.

Simulations were conducted with the Micromag program. Standard permalloy magnetic parameters were used. Along with other program control parameters, they are summarized in Table 4. No temperature effects are studied.

Table 4. Permalloy Micromag parameters

$Ms\left(A/M\right)$	$A\left(J/M\right)$	$K_1\left(J/M^3\right)$	$K_2\left(J/M^3\right)$	a	$\Delta t_{\max}$	$t_{\max}$
8.6×10^5	1.3×10^{-11}	0	0	0.75	0.1 $\left(0.526ps\right)$	10^{-5}degree

The ring is created with the region constrained by the inequality

$100 \le X^2 + Y^2 \le 400$. The cross-ties with 10nm and 30nm widths are created with additional regions constrained by $\begin{cases} X^2 + Y^2 \le 100 \\ 9 \le Y \le 10 \end{cases}$ and $\begin{cases} X^2 + Y^2 \le 100 \\ 7 \le Y \le 12 \end{cases}$ respectively.

The external fields are applied at $0°, 45°$ and $90°$ relative to the X axis. Applied field was scanned from $1500 \text{K}\,{}^{\text{A}}\!/_{\text{M}} (18.77\text{KOe})$ to $-1500 \text{K}\,{}^{\text{A}}\!/_{\text{M}} (-18.77\text{KOe})$ at an $100 \text{K}\,{}^{\text{A}}\!/_{\text{M}}$ interval and from $100 \text{K}\,{}^{\text{A}}\!/_{\text{M}} (1.25\text{KOe})$ to $-100 \text{K}\,{}^{\text{A}}\!/_{\text{M}} (-1.25\text{KOe})$ was scanned at a $10 \text{K}\,{}^{\text{A}}\!/_{\text{M}}$ interval. For both cross-tie structures, refined scans starting from the metastable configuration at $20 \text{K}\,{}^{\text{A}}\!/_{\text{M}}$ and ending at the metastable configuration at $-20 \text{K}\,{}^{\text{A}}\!/_{\text{M}}$ were performed at a $0.5 \text{K}\,{}^{\text{A}}\!/_{\text{M}} (6.26\text{Oe})$ interval to examine details in the reversal process.

The geometric shapes and applied fields are illustrated in Figure 9. In Figure 9, $H_{z,x}$, $H_{z,y}$ and $H_{z,xy}$ are the applied fields in the ring plane and parallel, perpendicular and diagonal to the cross-tie direction.

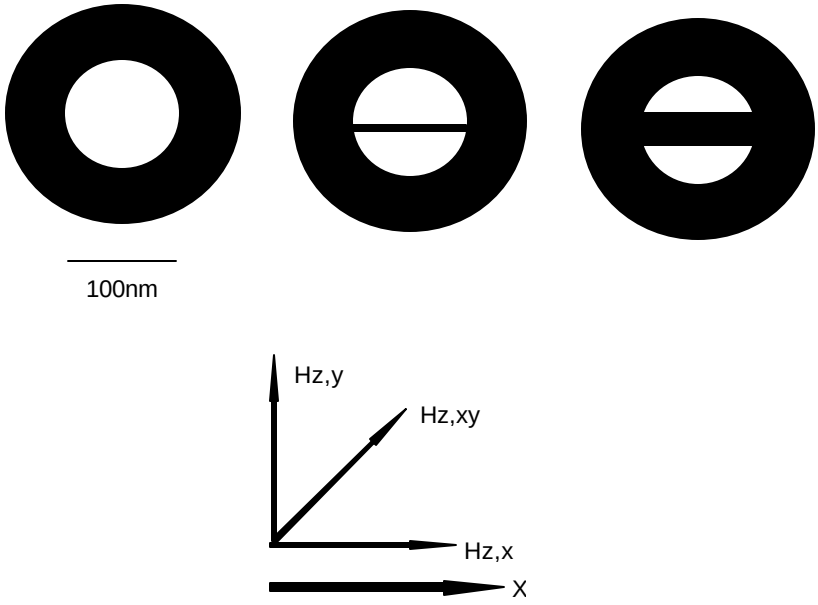

Figure 9. Applied field and geometry of ring and cross-tie modified ring

4.2 Results and Discussion

4.2.1 Hysteresis of the Ring

Nano ring magnetic elements have been extensively studied both experimentally and via modeling. For nano rings, the geometry is crucial in determining the remanent state, coercivity state and reversal process. Different size, inner/outer radius ratio or thickness may result in different reversal processes. To provide comparisons with the cross-tie structure, hysteresis for rings without the cross-tie was performed under exactly same conditions. Not surprisingly, hysteresis with applied fields in parallel, diagonal and perpendicular directions give identical results for three systems.

In all cases, the hysteresis was started from a random initial spin configuration with a strong applied field to saturate the magnetization. Due to the small specimen size, local nucleation is not likely to form in the rings.

The hysteresis loops are given in Figure 10. Both the parallel magnetization component relative to the applied field (Mp) and the vertical magnetization component (Mv) to the applied field are plotted. For the diagonal hysteresis, Mp is given by $M_x \cos\frac{p}{4} + M_y \sin\frac{p}{4}$ and Mv is given by $M_y \cos\frac{p}{4} - M_x \sin\frac{p}{4}$. The switching field is about $200 K_{/M}^{A}$.

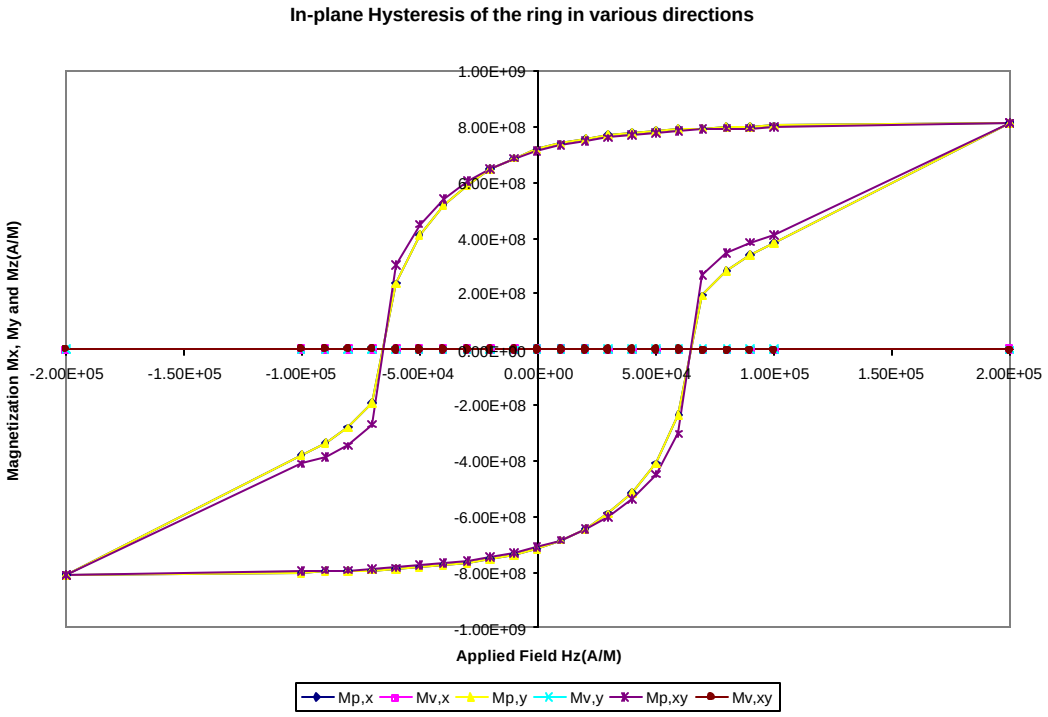

Figure 10. In-plane hysteresis of the ring in various directions

The initial onion states in parallel, vertical and diagonal hysteresis are illustrated in Figure 11. As seen in this figure, the domain patterns in the remanent states are the same as in the initial states. The coercive states are illustrated in Figure 12.

The spins in the sections parallel to the applied filed direction are pinned while the spins in diagonal sections rotate. The spins in regions I and III (upper right, lower left) rotate clockwise and the spins in regions II and IV (upper left, lower right) rotate counterclockwise. In coercive states, the spins in the diagonal sections are flipped, but the remaining spins are still pined in the positive X direction. This reversal pattern has also been observed by Zhu[36] for Cobalt rings with a strong anisotropy. The pinned spins in parallel and perpendicular sections are gradually flipped in stronger applied field in the –X direction. These factor results in the undesired non-squareness of the hysteresis loop

and the wide switching field distribution.

Permalloy is an extremely soft magnetic material. The crystalline anisotropy constant is around $3\,{}^{J}\!/_{M^3}$. Thus, thermal stability should be estimated using the shape anisotropy which is $6.5\times10^4\,{}^{A}\!/_{M}$. This shape anisotropy was estimated from Figure 10 from the coercive field $K_u = \frac{m_0 M_s}{2} H_c = 3.51\times10^4\,{}^{J}\!/_{M^3}$.

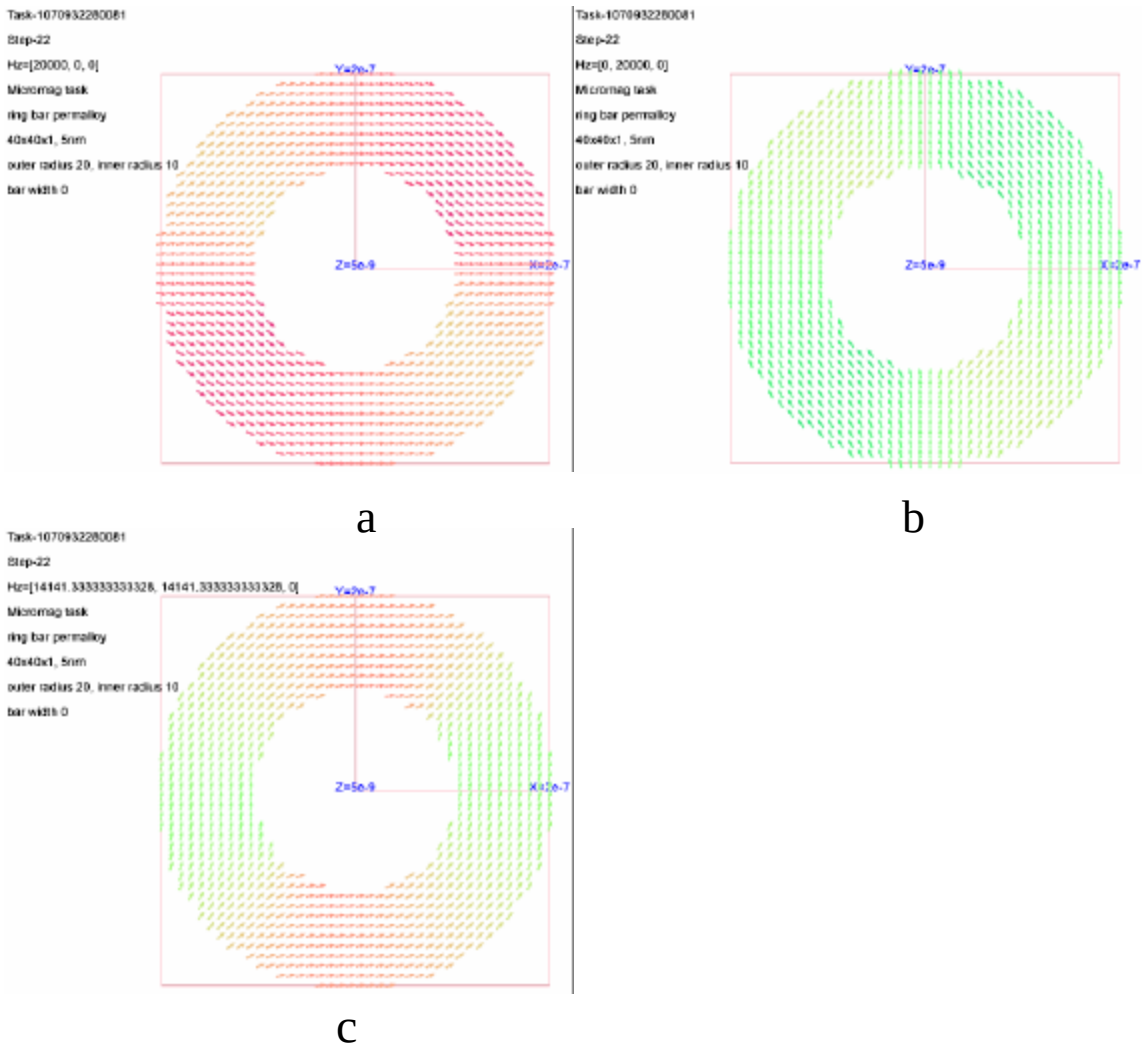

Figure 11. Initial onion states in horizontal (a), vertical (b) and diagonal (c) hysteresis. Applied field is 20K ${}^{A}\!/_{M}$

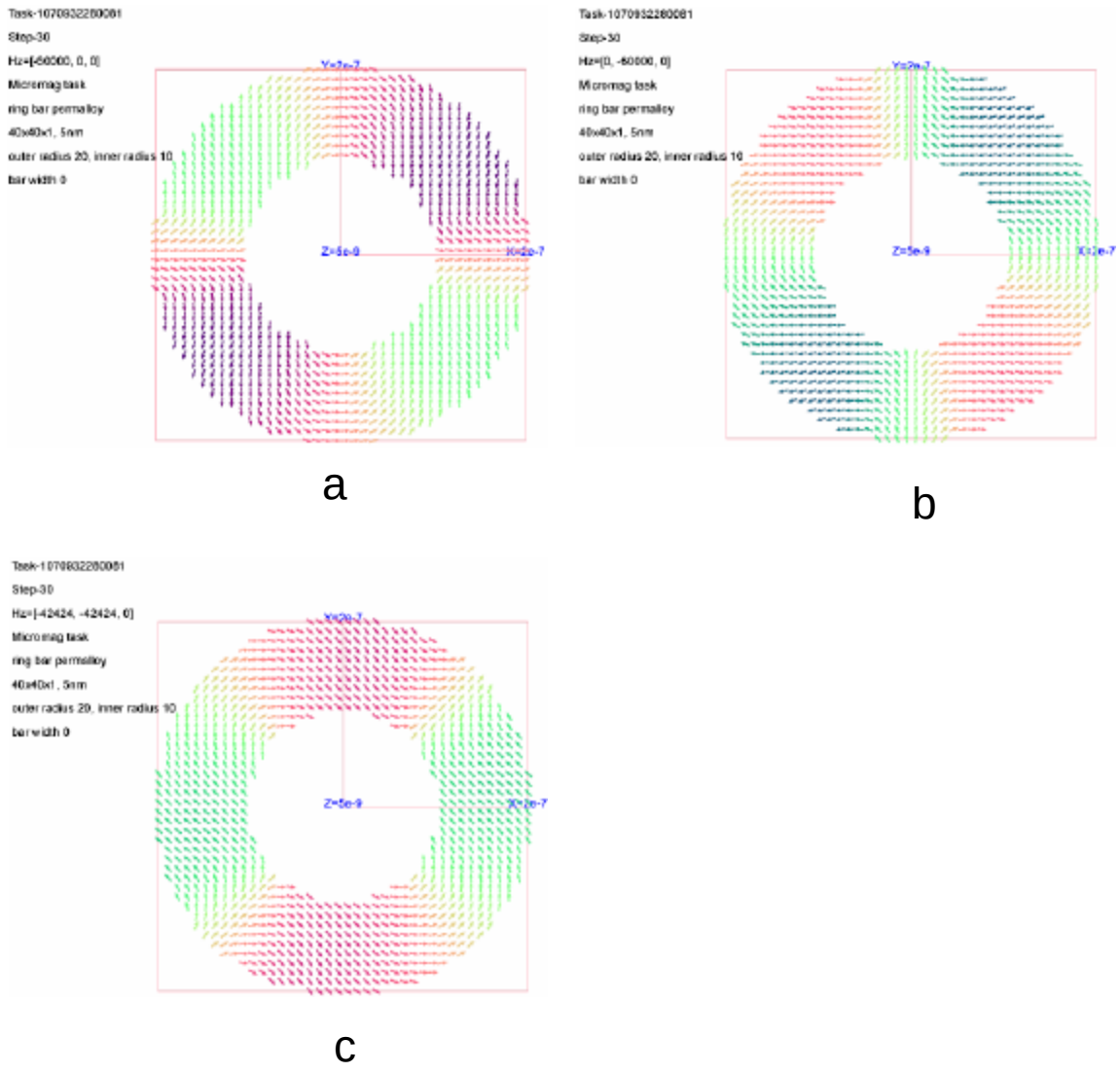

Figure 12. Domain pattern immediately before coercive state in parallel (a), horizontal (b) and diagonal (c) hysteresis at-60K A/M

The response time is defined as the time required to achieve a new metastable state in response to a changing applied field. Owing to the artificially large damping coefficient used to speed up simulations, the response time does not agree well with the experimental value. The response time is a property that most micromagnetics simulations don't report. However, a longer response time is related to more complex

intrinsic spin movements in achieving a metastable state. The switching time is calculated by accumulating the response times of every hysteresis step in the switching range. The simulated switching time is 6.43ns.

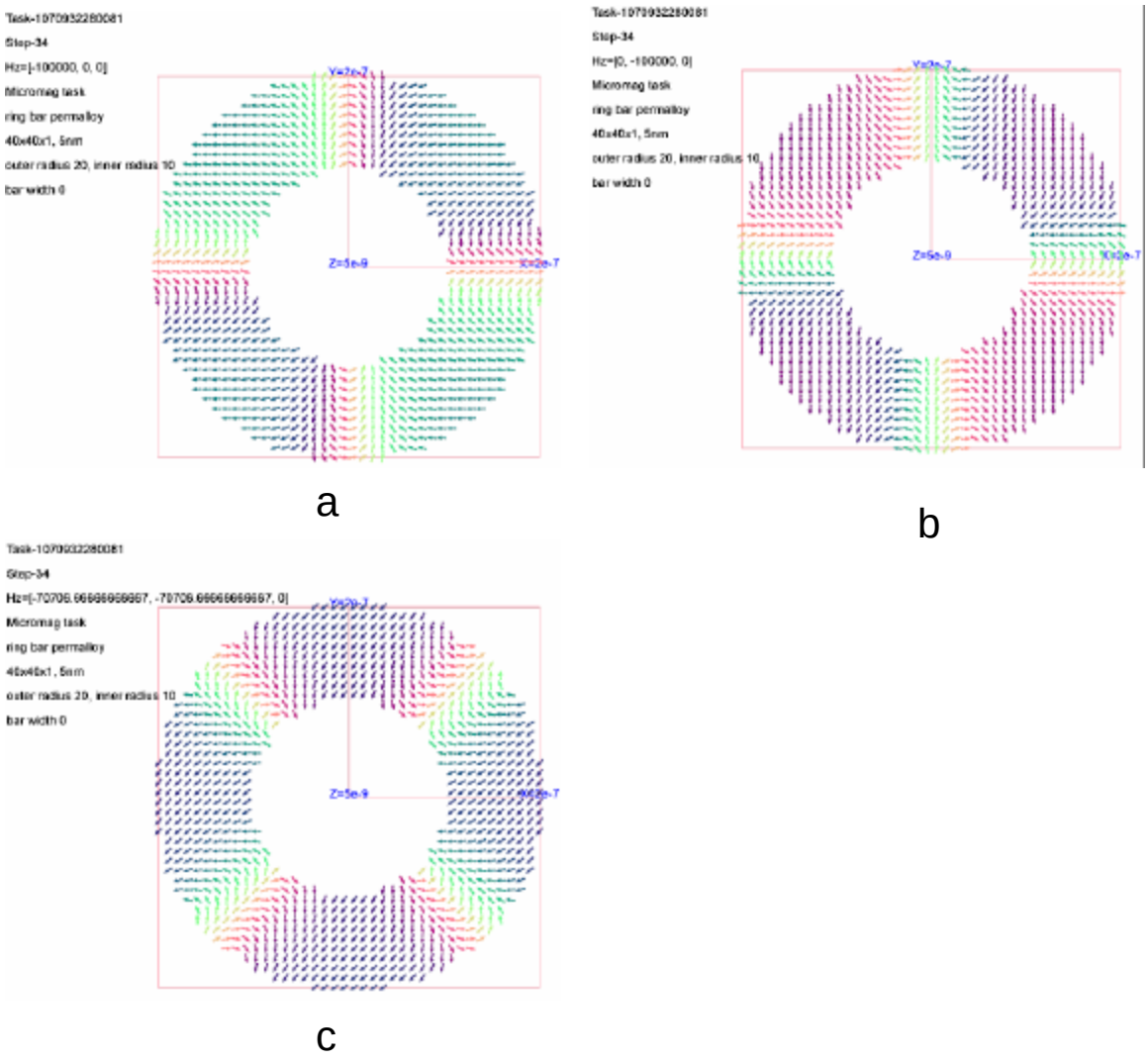

Figure 13. Last stages of ring versal in parallel, perpendicular and diagonal direction at 100K $A/_M$. a: Parallel. b: perpendicular. c: diagonal

4.2.2 Parallel Hysteresis of the Cross-Tie Structure

The spins in the cross-tie prefer to align in X direction, which is coincident with the direction of the pinned spins in the ring. Thus, magnetization reversal is harder for the

cross-tie modified rings. However, because the spins in the cross-tie and the pinned spins in the ring act as a single domain, the reversal process for the modified rings in the direction of applied field parallel to the cross-tie direction is not much different from the reversal process for the ring without a cross-tie. The magnetostatic field contribution from the spins in the cross-tie is in the opposite direction to the applied field. This helps the spins diagonal to the cross-tie to flip in response to a more positive applied field. The pinned spins in the top and bottom sections of the ring flip after the spins in the diagonal sections flip and are followed by the flipping of spins in the left and right sections of the ring. The spins in the cross-tie flip last and at a much stronger reversal field. *i.e.* the switching field is wider. The narrower the cross-tie width, the more obvious this effect is. Figure 14 illustrates the parallel hysteresis loops of the rings, both original and modified. The hysteresis loops are plotted as the normalized parallel magnetization component as a function of applied field. In Figure 14, mp0 is the normalized parallel magnetization component of the ring, mp1 is the normalized parallel magnetization component of the ring with 10nm wide cross-tie, and mp3 is the normalized parallel magnetization component of the ring with 30nm wide cross-tie. Note that, although the switching fields are slightly different, the remanent states and coercivity states are exactly the same. The simulated switching time for the 10nm cross-tie structure is 13ns. For the 30nm cross-tie structure, it is 25ns. This can be understood in terms of longer time needed to reverse the spins in the ties. Caution must be taken in interpreting the switching fields and switching times simulated in the parallel hysteresis, because the interval taken from $300 K A/M$ to $200 K A/M$ is not small enough to reveal the details of the reversal process.

The domain patterns at a later step (H_z = -200K A/M or-2.5KO$_e$) of the parallel

hysteresis loops are illustrated in Figure 15. Note that, the last step of the reversal process is the flipping of spins in the cross-tie structure. This process starts from both ends of the cross-tie.

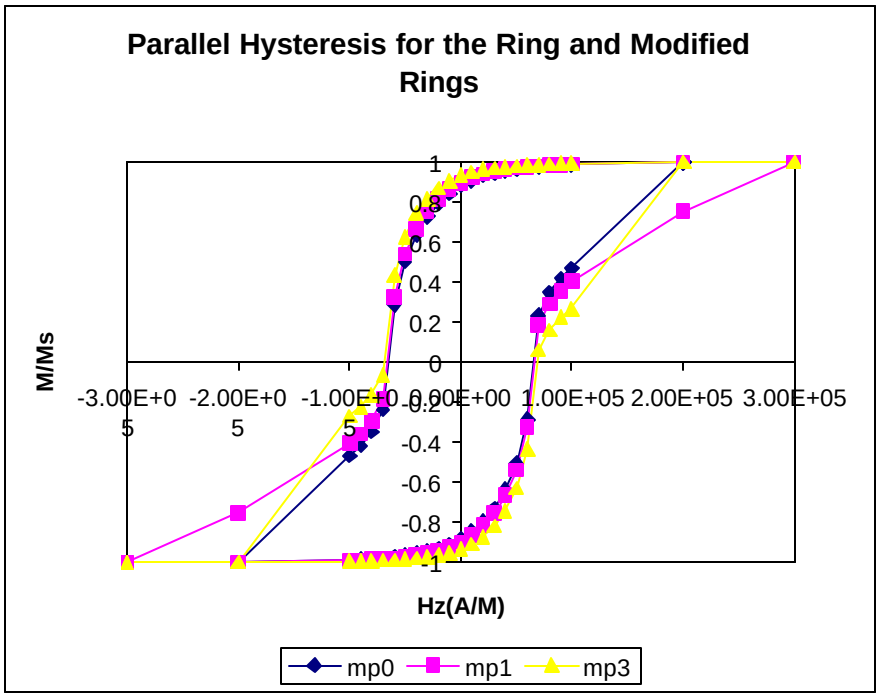

Figure 14. Normalized parallel magnetization components as functions of applied field. mp0 corresponds to the ring, mp1 corresponds to the structure with 10nm wide cross-tie and mp3 corresponds to the structure with 30nm wide cross-tie. The magnetizations are normalized relative to their saturated values.

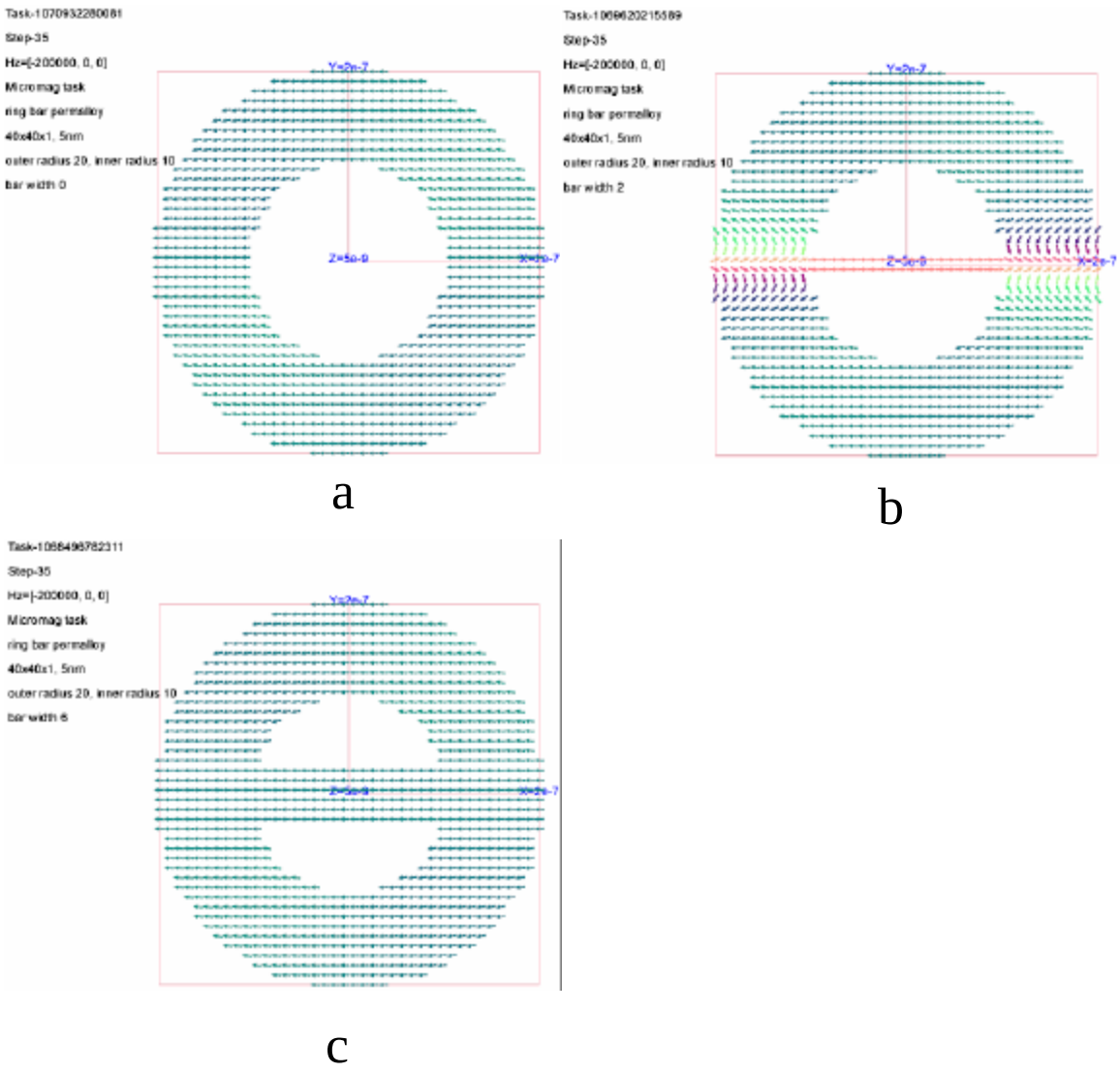

Figure 15. Late stages of parallel hysteresis for the ring and modified rings at 200K $^{A}/_{M}$

4.2.3 Perpendicular Hysteresis of the Cross-Tie Structure

The applied field is in the ring plane, but perpendicular to the cross-tie. The applied field doesn't favor the magnetostatic requirements of the spins in the cross-tie. The spins in the cross-tie can be forced to be perpendicular to the cross-tie direction when the applied field is very large. But, they tend to align in the parallel direction when the applied field is reduced. In other words, the switching processes have long tails, because the second stage of the switching process, the rotations of the spins in the cross-ties,

happens at a much stronger applied field. The spins in the cross-ties flip through "s" intermediate states. Once the "s" states are formed, the demagnetizing contribution from the spins in the cross-tie is in horizontal direction. This additional field rotates the domain walls. Thus, a fast coherent rotation switching process is achieved.

The hysteresis loop of the ring without the cross-tie when the applied field is in the perpendicular direction has already been discussed. The hysteresis loops of the cross-tie structures are illustrated in Figure 16. For contrast, they are plotted for the same applied field range as the range of the ring in Figure 14. The apparent difference in Figure 16 is that the parallel magnetization components (Mx in this case) are no longer negligible. This is an indication of coherent rotation.

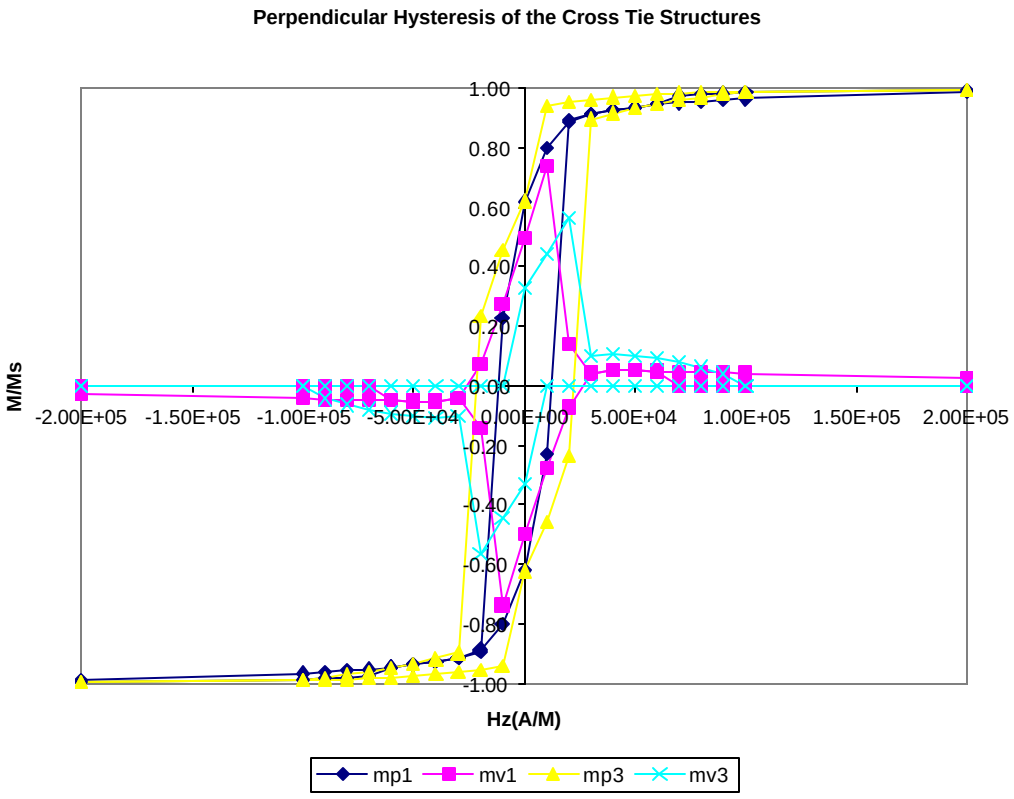

Figure 16. Perpendicular hysteresis of the cross-tie structure. mp1 and mv1 are the Y and X magnetization components of the ring with tie width 10nm, mp3 and mv3 are the Y and X magnetization components of the ring with tie width 30nm.

The formation of the "s" state of the narrow tie starts at $60 K_{A/M}$. For the wide tie, the field is $30 K_{A/M}$. Under the condition, the spins in the rings are in onion states. Due to the small number of spins in the ties, the total magnetizations are almost the same as those in the original rings, as shown in Table 5.

Table 5. Normalized magnetization in perpendicular hysteresis

Hz(A/M)	My1/Ms	Mx1/Ms	My3/Ms	Mx3/Ms	Hz(A/M)	My1/Ms	Mx1/Ms	My3/Ms	Mx3/Ms
600000	9.99E-01	1.43E-19	1.00E+00	5.78E-19	**-600000**	-9.99E-01	7.04E-19	-1.00E+00	-6.62E-19
500000	9.99E-01	-7.83E-19	9.99E-01	-3.41E-20	**-500000**	-9.99E-01	5.44E-20	-9.99E-01	-1.02E-19
400000	9.99E-01	8.87E-19	9.99E-01	1.51E-19	**-400000**	-9.99E-01	1.19E-18	-9.99E-01	-1.09E-18
300000	9.98E-01	4.08E-20	9.98E-01	4.43E-19	**-300000**	-9.98E-01	1.66E-18	-9.98E-01	-5.38E-19
200000	9.95E-01	4.51E-18	9.97E-01	-9.45E-19	**-200000**	-9.95E-01	-4.48E-18	-9.97E-01	1.22E-18
100000	9.86E-01	2.25E-15	9.90E-01	1.58E-18	**-100000**	-9.86E-01	-2.40E-15	-9.90E-01	4.00E-19
90000	9.84E-01	5.83E-13	9.88E-01	9.38E-18	**-90000**	-9.84E-01	-6.22E-13	-9.88E-01	-6.52E-18
80000	9.81E-01	2.23E-10	9.86E-01	2.58E-17	**-80000**	-9.81E-01	-2.38E-10	-9.86E-01	-2.85E-17
70000	9.78E-01	8.19E-08	9.84E-01	1.00E-16	**-70000**	-9.78E-01	-8.73E-08	-9.84E-01	-9.78E-17
60000	9.46E-01	5.00E-02	9.80E-01	4.90E-16	**-60000**	-9.46E-01	-5.00E-02	-9.80E-01	-4.66E-16
50000	9.38E-01	5.11E-02	9.76E-01	4.48E-15	**-50000**	-9.38E-01	-5.11E-02	-9.76E-01	-4.33E-15
40000	9.28E-01	5.11E-02	9.71E-01	8.74E-14	**-40000**	-9.28E-01	-5.11E-02	-9.71E-01	-8.45E-14
30000	9.15E-01	4.39E-02	9.63E-01	4.34E-12	**-30000**	-9.15E-01	-4.39E-02	-9.63E-01	-4.20E-12
20000	8.86E-01	-7.08E-02	9.53E-01	6.59E-10	**-20000**	-8.86E-01	7.08E-02	-9.53E-01	-6.38E-10
10000	7.99E-01	-2.77E-01	9.40E-01	3.48E-07	**-10000**	-7.99E-01	2.77E-01	-9.40E-01	-3.37E-07
0	6.21E-01	-4.98E-01	6.21E-01	-3.27E-01	**0**	-6.21E-01	4.98E-01	-6.21E-01	3.27E-01
-10000	2.27E-01	-7.37E-01	4.58E-01	-4.43E-01	**10000**	-2.27E-01	7.37E-01	-4.58E-01	4.43E-01
-20000	-8.95E-01	-1.41E-01	2.37E-01	-5.63E-01	**20000**	8.95E-01	1.41E-01	-2.37E-01	5.63E-01
-30000	-9.15E-01	-4.39E-02	-8.97E-01	-1.00E-01	**30000**	9.15E-01	4.39E-02	8.97E-01	1.00E-01
-40000	-9.28E-01	-5.08E-02	-9.17E-01	-1.09E-01	**40000**	9.28E-01	5.08E-02	9.17E-01	1.09E-01
-50000	-9.38E-01	-5.10E-02	-9.34E-01	-1.02E-01	**50000**	9.38E-01	5.10E-02	9.34E-01	1.02E-01
-60000	-9.45E-01	-4.99E-02	-9.48E-01	-9.14E-02	**60000**	9.45E-01	4.99E-02	9.48E-01	9.14E-02
-70000	-9.52E-01	-4.84E-02	-9.61E-01	-7.85E-02	**70000**	9.52E-01	4.84E-02	9.61E-01	7.85E-02
-80000	-9.57E-01	-4.67E-02	-9.72E-01	-6.31E-02	**80000**	9.57E-01	4.67E-02	9.72E-01	6.31E-02
-90000	-9.62E-01	-4.51E-02	-9.81E-01	-4.32E-02	**90000**	9.62E-01	4.51E-02	9.81E-01	4.32E-02
-100000	-9.65E-01	-4.34E-02	-9.90E-01	-1.49E-03	**100000**	9.65E-01	4.34E-02	9.90E-01	1.49E-03
-200000	-9.89E-01	-2.47E-02	-9.97E-01	1.90E-08	**200000**	9.89E-01	2.47E-02	9.97E-01	-1.90E-08
-300000	-9.98E-01	-3.29E-06	-9.98E-01	-3.94E-10	**300000**	9.98E-01	3.29E-06	9.98E-01	3.94E-10
-400000	-9.99E-01	4.71E-08	-9.99E-01	-1.35E-13	**400000**	9.99E-01	-4.71E-08	9.99E-01	1.35E-13
-500000	-9.99E-01	-2.26E-10	-9.99E-01	7.86E-16	**500000**	9.99E-01	2.26E-10	9.99E-01	-7.86E-16
-600000	-9.99E-01	-4.85E-12	-1.00E+00	2.69E-18	**600000**	9.99E-01	4.85E-12	1.00E+00	-2.57E-18

The magnitude of the torque for each spin indicates the stress the spin experiences. A larger magnitude for the torque means the spins have greater motion. Before the

formation of “s” states in the cross-ties, the field distributions are symmetric to the Y axes, the spins in the left half and their mirror spins in the right half have the same torque. But after with the formation of the “s” states, the upper left and lower right sections have spins with greater torque, as shown in Figure 17. From Figure 18, it is apparent that the spins in these two sections rotate first. These rotations are driven by the demagnetizing field contributions from the spins in the cross-tie. Unlike the parallel hysteresis, the reversal for the modified rings starts at reversed applied field. The reduced remanence for the narrow and wide tie structures are the same, but the coercivity ($110\text{K}\,{}^{A}\!/_{M}$ or 1.37KOe) of the narrow tie structure is smaller than the coercivity ($250\text{K}\,{}^{A}\!/_{M}$ or 3.13KOe) of the wide tie structure. At the remanent state, the parallel components for both cross-tie structures are not zero. Therefore, the remanent magnetization is in the diagonal direction. For this reason, hysteresis in the diagonal direction is preferred.

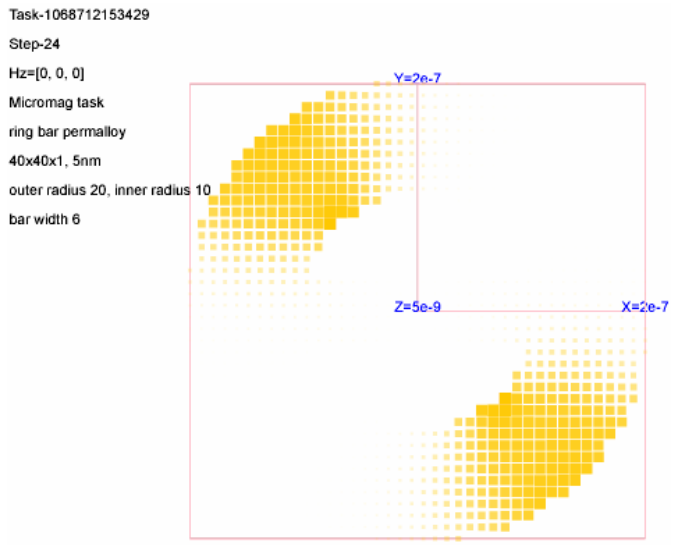

Figure 17. Torque distribution in the remanent state of the narrow tie structure. The size and intensity of the color for each cell are proportional to the relative magnitude of the torque.

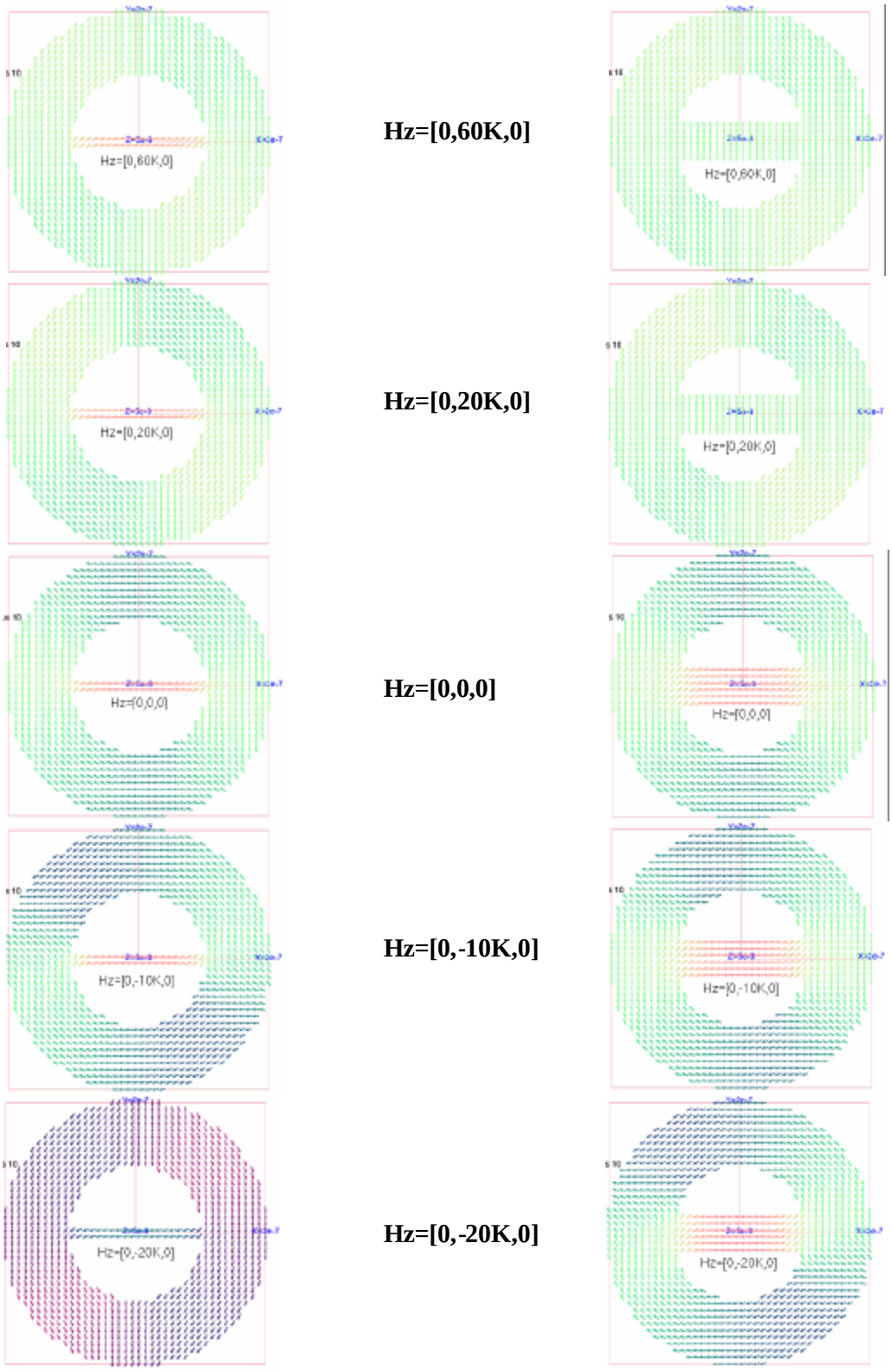

Figure 18. Domain patterns of the cross-tie structure in perpendicular hysteresis.

The simulated switching time for the narrow tie structure is 17.5ns. For the wide tie, it is 11ns, comparable to the switching times in parallel hysteresis.

Starting from a metastable state at $20K\,A/M$, a detailed field scan at $500\,A/M$ or 6.25Oe interval was performed until the applied field reached $-20K\,A/M$. This field range includes the remanent states of both narrow and wide tie structures and the coercive state of the narrow tie structure. The portions of hysteresis loop in the perpendicular direction are shown in Figure 19. Note, although the spins in the ties are aligned in the +X direction, more spins are oriented in the –X direction. The total X-components of magnetizations are negative. In Figure 19, it is clear that the spin flip for the narrow tie structure happens in a narrow range ($-10.5K\,A/M$ to $-11K\,A/M$). The jump at $18K\,A/M$ for the wide tie structure corresponds to the formation of the "s" state in the cross-tie.

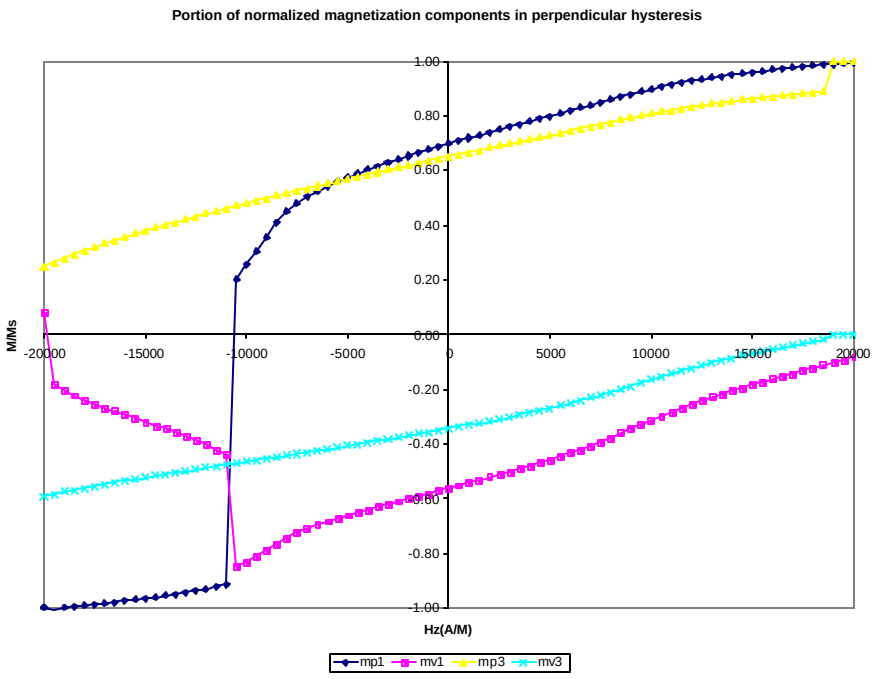

Figure 19. Magnetization components as functions of the applied field in perpendicular hysteresis

4.2.4 Diagonal Hysteresis of the Cross-Tie Structure

For the hysteresis in the diagonal direction, the parallel component of the applied field helps the spins in the cross-ties to align in the +X direction. Therefore, the “s” states in the cross-ties exist at the very beginning. In addition, the parallel components force the spins in the ties to flip at earlier stages. As discussed before, the remanence is higher and the coercivity force is smaller. Therefore, the squareness of diagonal hysteresis is greater.

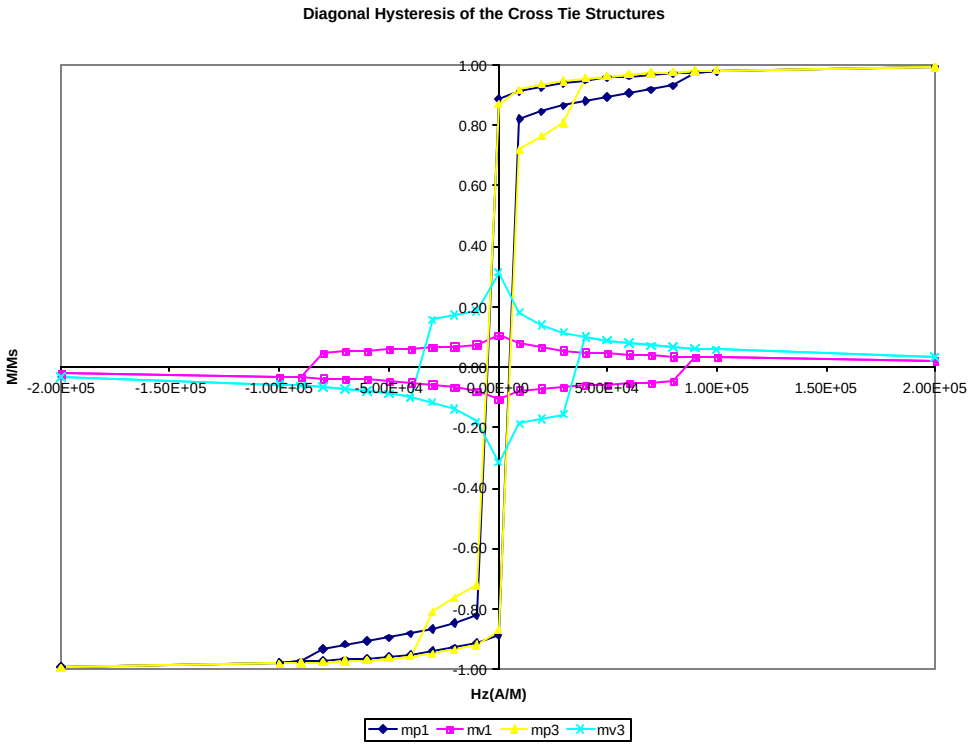

Figure 20. Diagonal hysteresis of the cross-tie structure

The reversal process is similar to that for the perpendicular hysteresis. More importantly, the remanent states in diagonal hysteresis are exactly the same as those in the perpendicular hysteresis. For this orientation the domain walls rotate clockwise, instead of counterclockwise, as in the case of perpendicular hysteresis. The reversals have two distinct stages. The first corresponds to the rotation of domain walls and the second corresponds to the reversal of spins in the cross-ties. Rotations of domain walls occur in a very narrow range of applied fields. For the narrow tie structure, it is $-6K\,{}^{A}\!/_{M} \sim -6.5K\,{}^{A}\!/_{M}$ or $-75Oe \sim 81Oe$. For the wide tie structure, the range is $-2K\,{}^{A}\!/_{M} \sim -2.5K\,{}^{A}\!/_{M}$ or $-25Oe \sim -31Oe$. The applied field range in which the spins in the ties flip is $-125Oe \sim -1131Oe$ and $-125Oe \sim -502Oe$ for the narrow tie and wide tie structures, respectively. However, even though the spins in the ties are not flipped, the

total magnetization domains are in stable configurations in reversing field as weak as -80Oe for both modified ring elements. This characteristic makes them good candidates for magnetic memory devices. The simulated times taken to rotate domain walls for the narrow tie and wide tie structures are 8.5ns and 5.8ns, respectively.

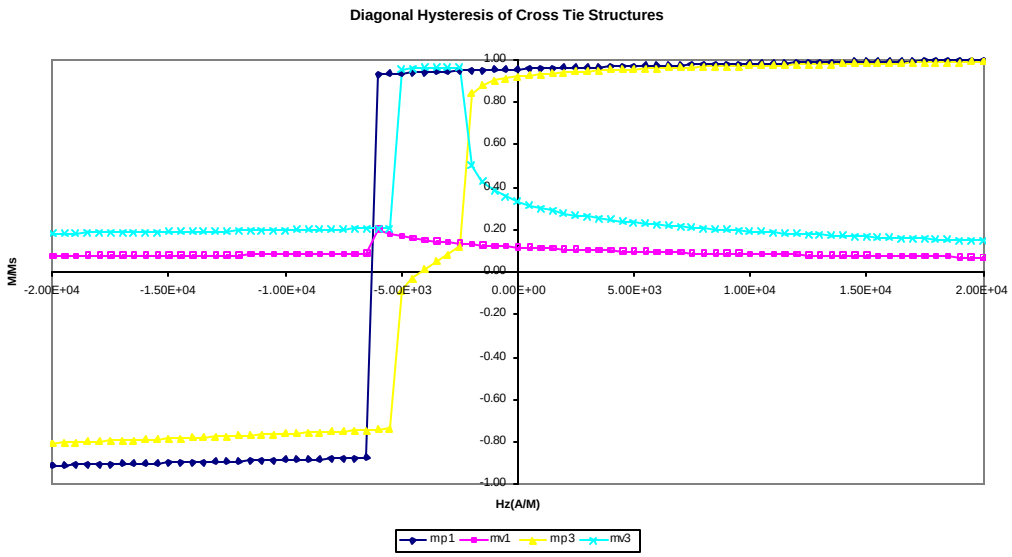

Figure 21. Diagonal hysteresis (part) of the cross-tie structure. mp1 and mv1 are the normalized components parallel and perpendicular to the applied field for the narrow tie structure. mp3 and mv3 corresponds to the wide tie structure.

A detailed scan with the applied field changing from 20K $^{A}/_{M}$ to -20K $^{A}/_{M}$ at 500 $^{A}/_{M}$ intervals was performed for the cross-tie structure. The normalized magnetization components are plotted as functions of applied field in Figure 21.

The rotation of domain wall is indicated by the angle between the magnetization and the cross-tie direction. Figure 22 gives the angle as a function of time during the domain wall motion process.

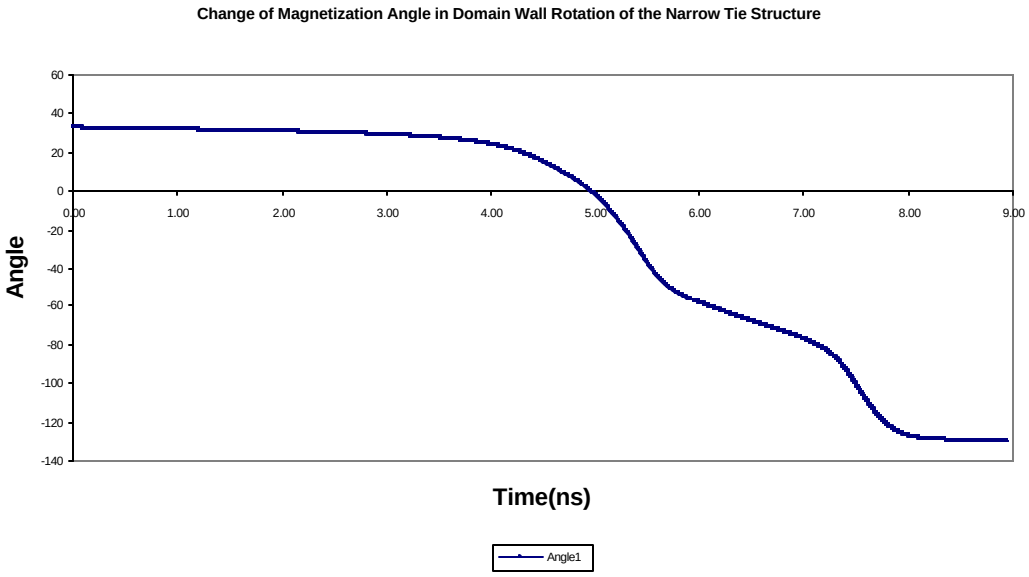

a. Change of magnetization angle with time in domain wall rotation of the narrow tie structure at -6.5K $^{A}/_{M}$.

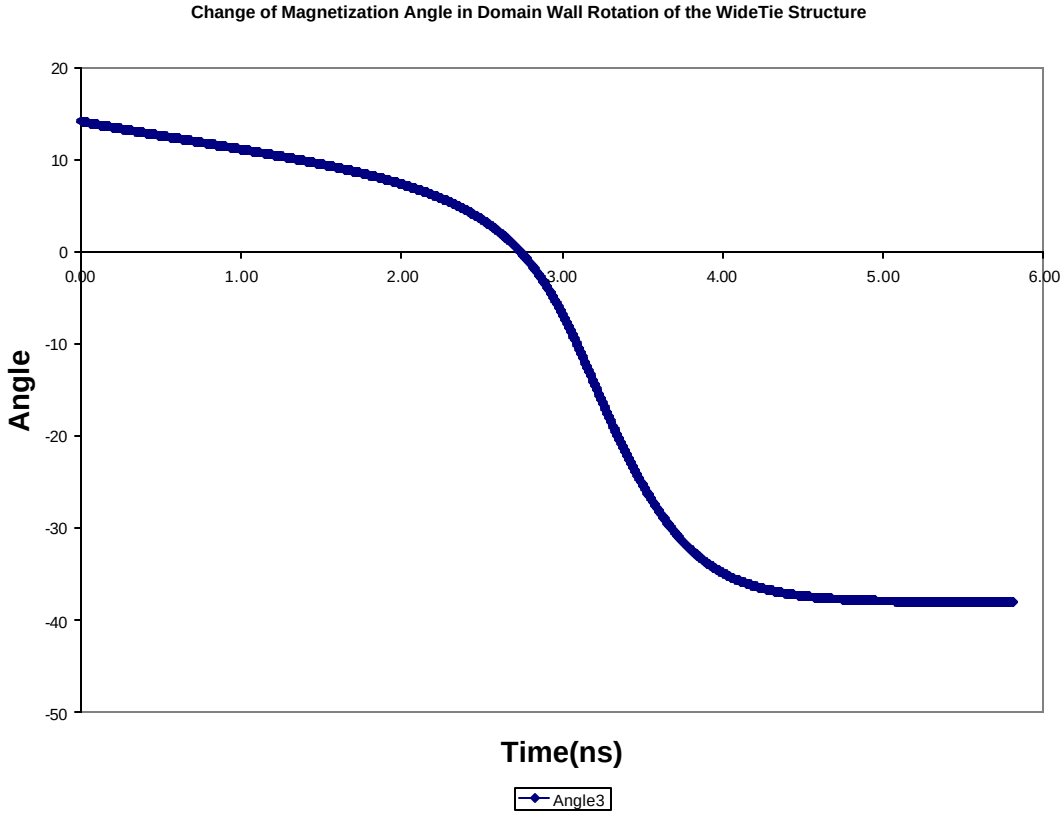

Figure 22. b. Change of magnetization angle with time in domain wall rotation of the wide tie structure at -2.5K $^{A}/_{M}$.

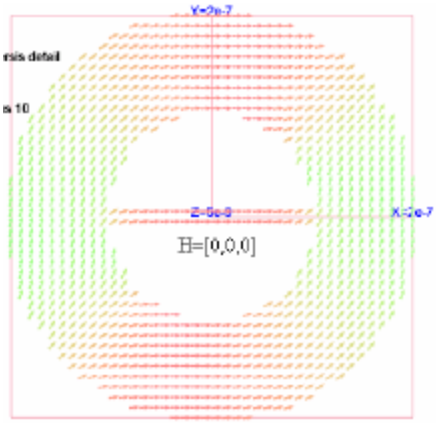

H=[0,0,0]

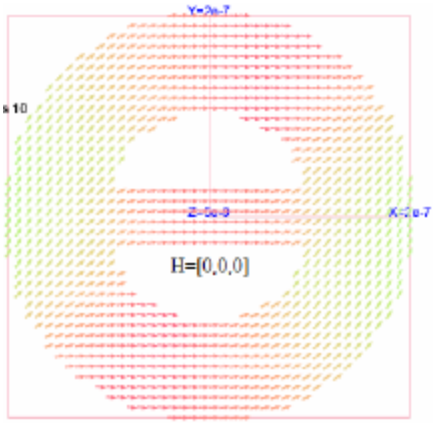

H=[0,0,0]

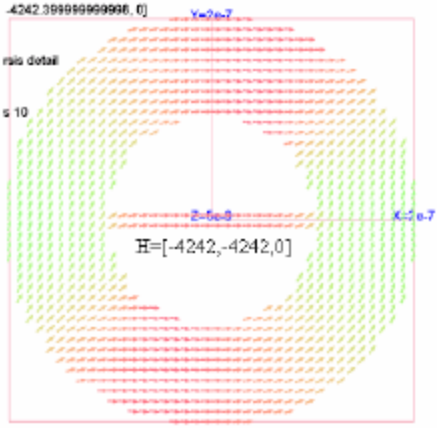

H=[-4242,-4242,0]

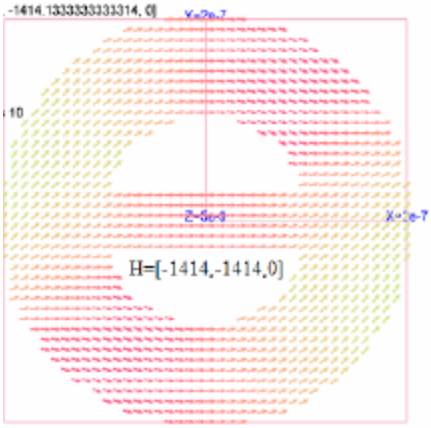

H=[-1414,-1414,0]

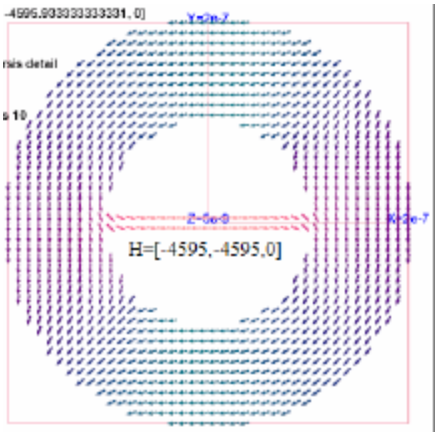

H=[-4595,-4594,0]

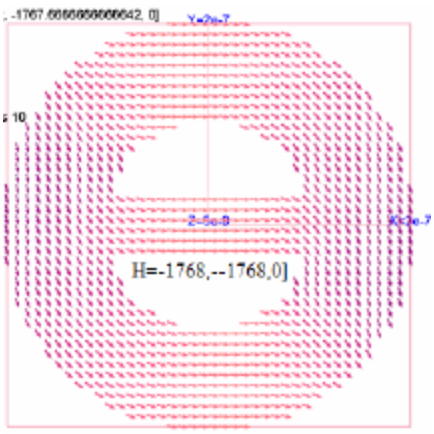

H=[-1768,-1768,0]

Figure 23. Domain configuration of the cross-tie structure in diagonal hysteresis

Figure 23 shows the domain patterns at the remanent states and before and after domain wall rotation of the cross-tie structure. For the wide tie structure, the domain wall rotation can be further divided into two stages. The first stage is to change the sign of the Y component, while the X component reaches its maximum. The second stage is the change in the sign of the X component, which is done in another jump at $-5\mathrm{K}\,A/M$.

4.3 Thermal Stability

The thermal fluctuation field can be estimated using $h\sqrt{2\frac{a\,k_B T}{(1+a^2)\,m_0 M_s^2 V \Delta t}}$

where h is a Gaussian random number. See the appendix and section 2.3.2 for discussions of the thermal fluctuation field strength. Given the parameters in Table 4 and the dimensionless time step is 0.1, or 0.66ps, the magnitude of thermal field for each cell is on the order of $0.26M_s = 228\mathrm{K}\,A/M$ at room temperature, which is comparable to magnetostatic and exchange fields when the anisotropy field is absent. This implies that a stochastic calculation with the thermal field included, instead of deterministic calculation, is needed. However, the total thermal field averaged over all cells is as small as $0.0082M_s = 6.8K\,A/M$.

Thermal stability is measured by the attempted frequency of flipping $f = f_0 e^{-\frac{\Delta E_B}{k_B T}}$ where f_0 is in the order of $10^{10} H_z$ and the anisotropy energy contributes to the energy barrier of flipping. In the absence of a magnetocrystalline anisotropy field, the thermal stability is estimated using shape anisotropy only. Shape anisotropy affects the attempted frequency of flip for the spins in the sample. At room

temperature, the factor of attempted frequency is given by $e^{-\frac{\Delta E_B}{k_B T}}$ according to Neel's law (Eq. 2.6), where ΔE_B, the energy barrier to flipping is estimated as the energy difference between remanent states along different magnetization paths.

Table 6 shows the stabilizing factors of the cross-tie structure due to shape anisotropy. The remanent states for the narrow tie structure in perpendicular and diagonal hysteresis are both thermally stable, but the remanent state for the wide tie structure in perpendicular hysteresis is thermally unstable.

Table 6. Thermal stabilizing factors of the cross-tie structure

Structure	$E_{\parallel}\left(\times 10^{-18} J\right)$	$E_{\angle}\left(\times 10^{-18} J\right)$	$e^{-\frac{\Delta E_{B\angle}}{k_B T}}$	$E_{\perp}\left(\times 10^{-18} J\right)$	$e^{-\frac{\Delta E_{B\perp}}{k_B T}}$
Narrow Tie	2.4465	2.3747	2.93×10^{-8}	2.4032	2.87×10^{-5}
Wide Tie	2.4999	2.4579	3.93×10^{-5}	2.5707	2.67×10^{7}

4.4 Conclusions

Shape anisotropy is introduced into permalloy ring elements by modifying the ring with a cross-tie. The geometric modification provides reliable and repeatable stabilization of the two desired "onion" states. While the modification with a cross-tie structure keeps the reversal process with the applied field parallel to the cross-tie unchanged, the reversal process with the applied field either perpendicular or along a diagonal change to domain wall rotations without involving a vortex intermediate state. This modification produces a structure that is more reliable than defect induced domain wall rotation that often involves vortex states.

The shape of the perpendicular and diagonal hysteresis for the cross-tie structure

is more desirable for MRAM applications. They are narrower, more square and with a narrower switching field distribution.

The wide tie structure exhibit similar property changes in reversal process. However, the reversal is not a single stage process. Thus, wide tie structure is not recommended for MRAM application.

For the narrow tie structure, the reversal of the “onion” states occurs in one simple jump, in both the perpendicular and diagonal hysteresis loops. The remanent states are thermally stabilized by shape anisotropy, with the remanent state in diagonal hysteresis even more stabilized. Due to its weak crystalline anisotropy, a permalloy ring is not preferred for MRAM application. However, geometric modification suggested here makes the modified rings ideal as ultrahigh density MRAM media.

Chapter 5 Magnetic Reversal of Pac-Man Magnetic Elements

5.1 Introduction

The switching field of a submicron MRAM element varies with the end shape and roughness of the element.[42] To reduce the magnetic defects made with fabrication, traditional MRAM device shapes are usually linear with modified ends, such as hexagonal or ellipse. Circular magnetic elements tend to form vortex states, and thus don't have the problems associated with non-circular shapes. Vortex states are more stable in ring elements than in circular discs.[43] The magnetic reversal of mesoscopic discs usually involves the formation of vortex cores and motion of the vortex core from one end of the magnetic element to an opposite end.[44] Intermediate "C" states are observed in the vortex core motion. Geometric modification of discs has been studied in various forms.[45] Particular geometries that remove the high energy off-center vortex cores of the discs have been proposed, fabricated and studied.[46] These elements are referenced as "Pac-Man" elements by the authors. Pac-Man shapes are sectors of discs and are characterized by the angle of the two slots. Two types of Pac-Man shapes, one modified from a circular disc (PM I) and the other modified from a half disc (PM II) have been examined, with various slot angles. Domain patterns of PM I elements depend on the slot angle. While PM I with small slot angle forms two domains, PM I with large slot angle forms a single domain and PM II elements form single domains. The hysteresis loops of PM II element array reveal better switching field distribution and switching field value

properties than hexagonal and ellipse elements of the same size.

It is generally found that the reversal process of Pac-Man magnetic elements depends on the size, thickness, slot angle and aspect ratio. This research attempts to investigate the effects of aspect ratio on the magnetic reversal process. Two Pac-Man permalloy elements are studied. The PM I type element is a 3/4 disc with radius 400nm and thickness 10nm. The PM II type element is a half disc with two slots crossing at 126.87 degrees. Figure 24 illustrates the two Pac-Man elements. The simulations were carried out using 10nm cubic cells with the same magnetic parameters of permalloy as those used in the ring simulations. The maximum dimensionless step size was set as 0.4, which is equivalent to 2.1ps. The damping coefficient was set as 0.75.

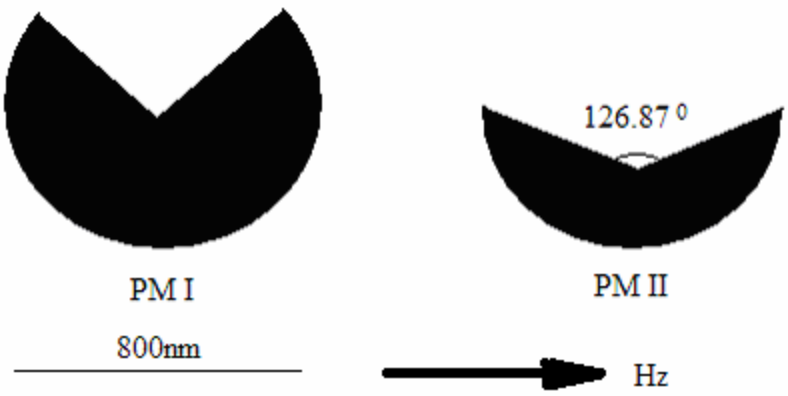

Figure 24. Geometry of the two Pac-Man elements

5.2 Reversal Process of the PM I element

The hysteresis of the PM I element was started from a uniform initial configuration for which all spins align in the +X direction. Two remanent states are expected, namely the "C" state and the reversed "C" state. The applied field is in the +X direction in the disc plane, ranging between $50K\,A/M\,(628.3Oe)$ and $-50K\,A/M\,(-628.3Oe)$.

The field is scanned at $5K\,{}^{A}/_{M}$ interval between $50K\,{}^{A}/_{M}$ and $5K\,{}^{A}/_{M}$, and $5K\,{}^{A}/_{M}$ to $-5K\,{}^{A}/_{M}$ at $500\,{}^{A}/_{M}$ interval. Figure 25 shows the hysteresis loop of the PM I element. The switching field is found to be $25K\,{}^{A}/_{M}$ or $314Oe$.

Clearly, the hysteresis curve does not meet MRAM application requirements.

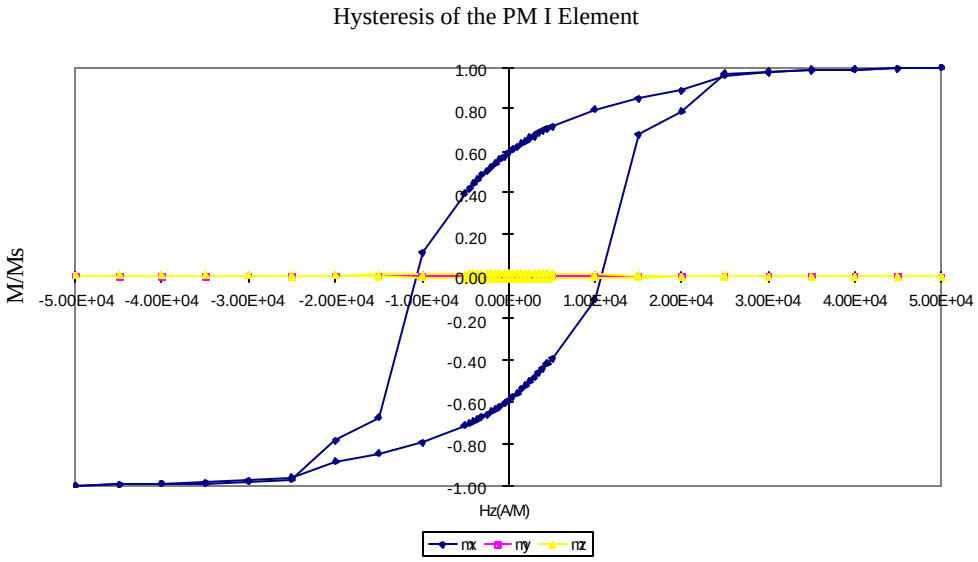

Figure 25. Hysteresis of the PM I Element

Unlike the thicker PM I element at a 90 degree slot crossing angle, which has two domains[46], the thinner PM I element in wider dimension forms one domain in the reversal process. The domain patterns encountered in the hysteresis of the PM I element can basically be explained in terms of magnetostatic effects. The spins in the rounded ends of the slot want to align in the vertical direction, the spins close to the slot edges want to align along the edge, and the spins in the bulk have more freedom to orient along any direction. The reversal starts from the rounded ends and occurs in two stages: the formation of a vortex core and the dissipation of the vortex core. Note, the two halves of the PM I element are not symmetric because the applied field is perpendicular to the

vertical symmetric axis. With the reduction of the applied field, the spins in the left end rotate clockwise to align vertically down, while the spins in the right end rotate counterclockwise to align vertically up. The remanent state can best be described as a "U" state, where about 30% of the spins near the right and left edges align up and down, respectively. During the reversal process, the spins near the edge of the element experience highest internal field and energy. But, the highest magnitude of torque does not occur on the edge, as shown in Figure 26. The areas with the most stress are also the areas with the greatest motional freedom. In the reversed applied field, the spins in these areas flip first, followed by the spins near the slot edges. With the increase of applied field in -X direction, the domain wall between the flipped spins and those not flipped moves down. When a sufficient number of reversed spins is established in the middle of the element, a vortex core is formed at the middle lower part of the element. This vortex core is gradually dissipated. The maximum magnitude of torque shifts to the vortex core once it is formed. This change is shown in Figure 26.

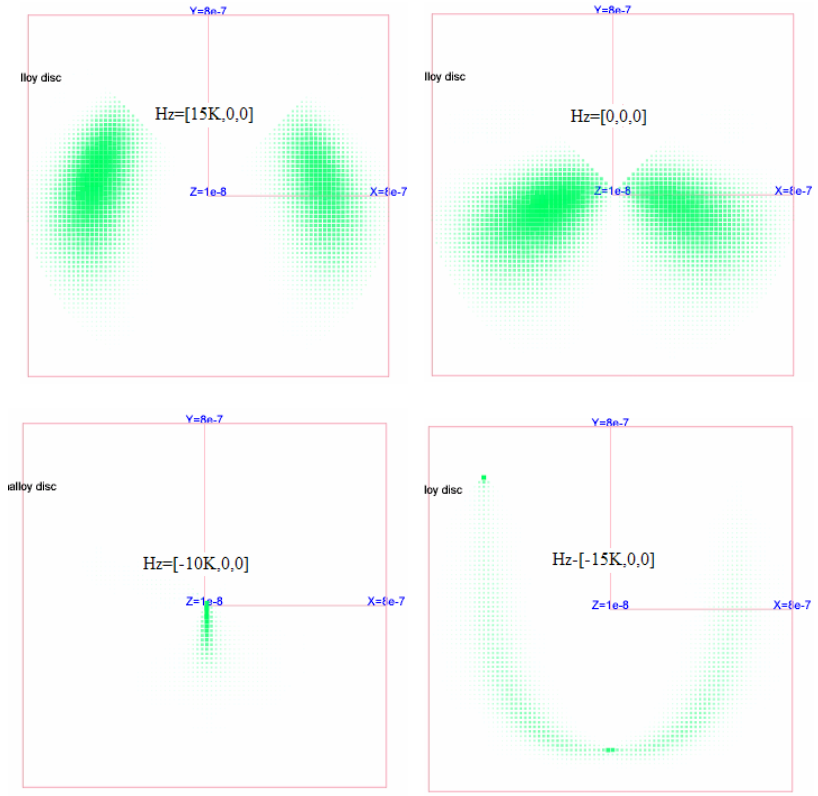

Figure 26. Torque map of the PM I element in hysteresis

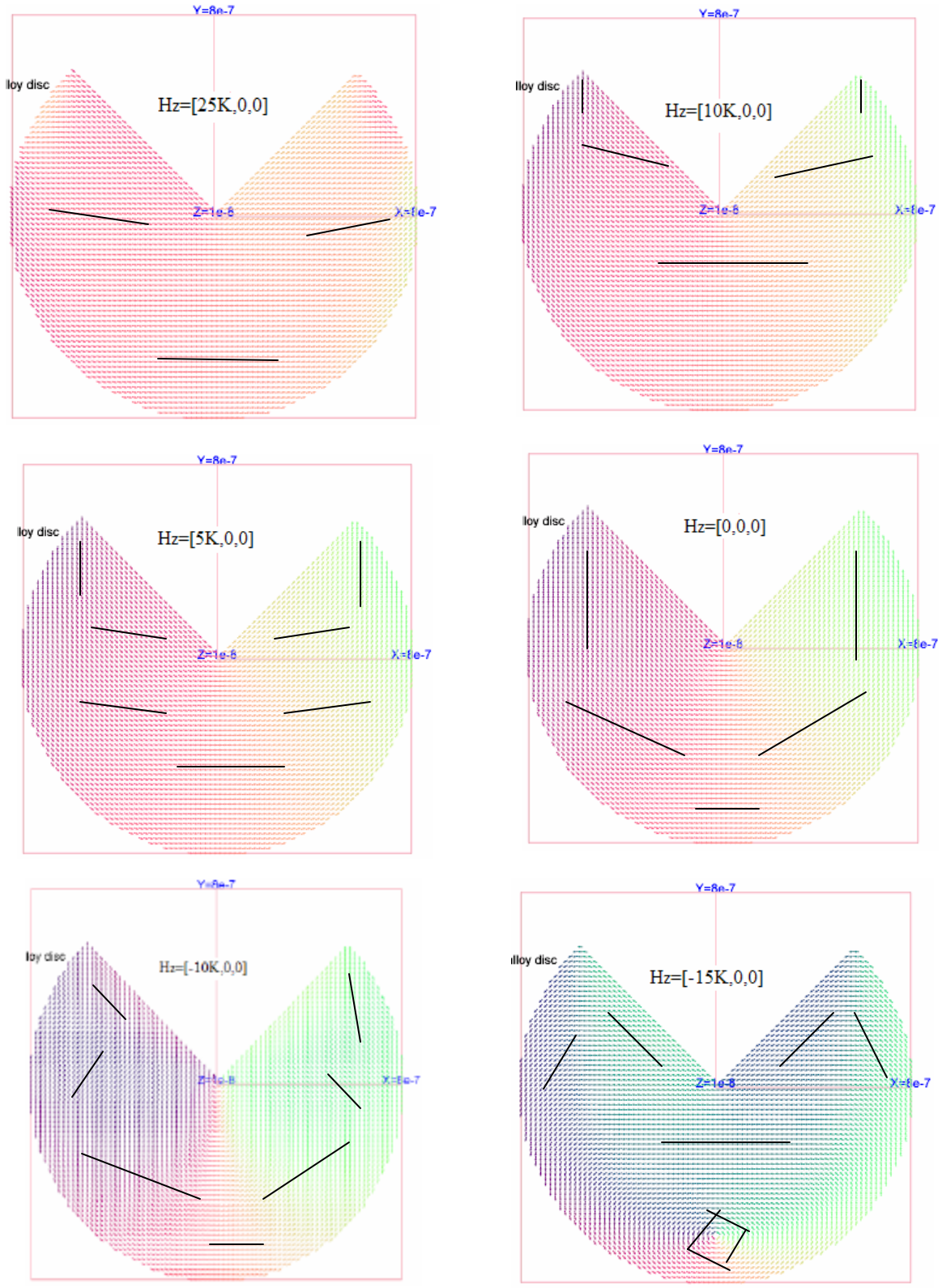

Figure 27. Domain configuration of the PM I element in hysteresis

5.3 Reversal Process of the PM II Element

The PM II element is bound by an $80\times40\times1$ grid. The two slots are defined by the constraints $X-2Y\geq0$ and $X+2Y\leq80$. The reversal process of the PM II element is much simpler. As shown in Figure 28, the reversal process is a one-stage process with a single jump. The switching field is approximately the same as that of the PM I element, but the switching field distribution is much narrower. At a reduced applied field, the spins are less well aligned in order to compromise with the more restricted shape requirements. Due to the larger aspect ratio, the spins close to the slot edges are forced to align horizontally, and have a higher energy barrier to flip. Thus, significant changes in the horizontal component of the magnetization happen in the negative applied field range and lead to greater squareness of the hysteresis loop. The remanent state is a single domain "C" state. The reversal mechanism is similar to that of the first stage of the PM I element, except that it happens in a much narrower applied field range.

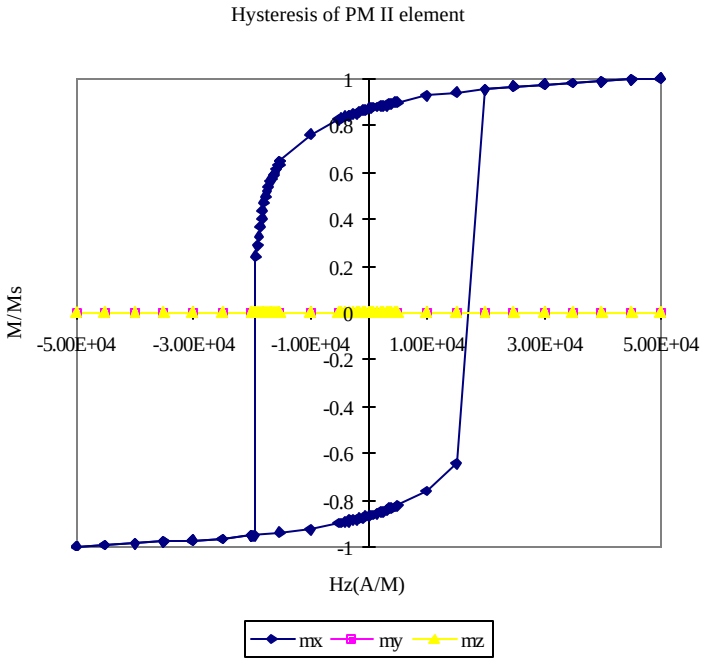

Figure 28. Hysteresis of the PM II element

A detail scan for the applied field changing from -15K $^{A}/_{M}$ to -20K $^{A}/_{M}$ at 250 $^{A}/_{M}$ or 3.14Oe interval was conducted on the metastable state at -15K $^{A}/_{M}$ applied field. The results are combined with the hysteresis loop in Figure 28. The hysteresis loop gives a switching field of 19250 $^{A}/_{M}$. Although the maximum magnitude of torque still occurs in the left and right center areas, the distribution of the torque magnitude is more even across the magnetic element. The torque map does not display the range of torque values as that of the PM I element and it reveals wider position changes of the most stressful areas. The difference in torque between the two elements is caused by the larger aspect ratio. The torque changes during the hysteresis loop are shown in Figure 30. The most important change is that no vortex core is formed in the reversal process of the PM II

element. This is a result of the limited room for vortex core formation. Hence the switching is faster and the switching field distribution is narrower.

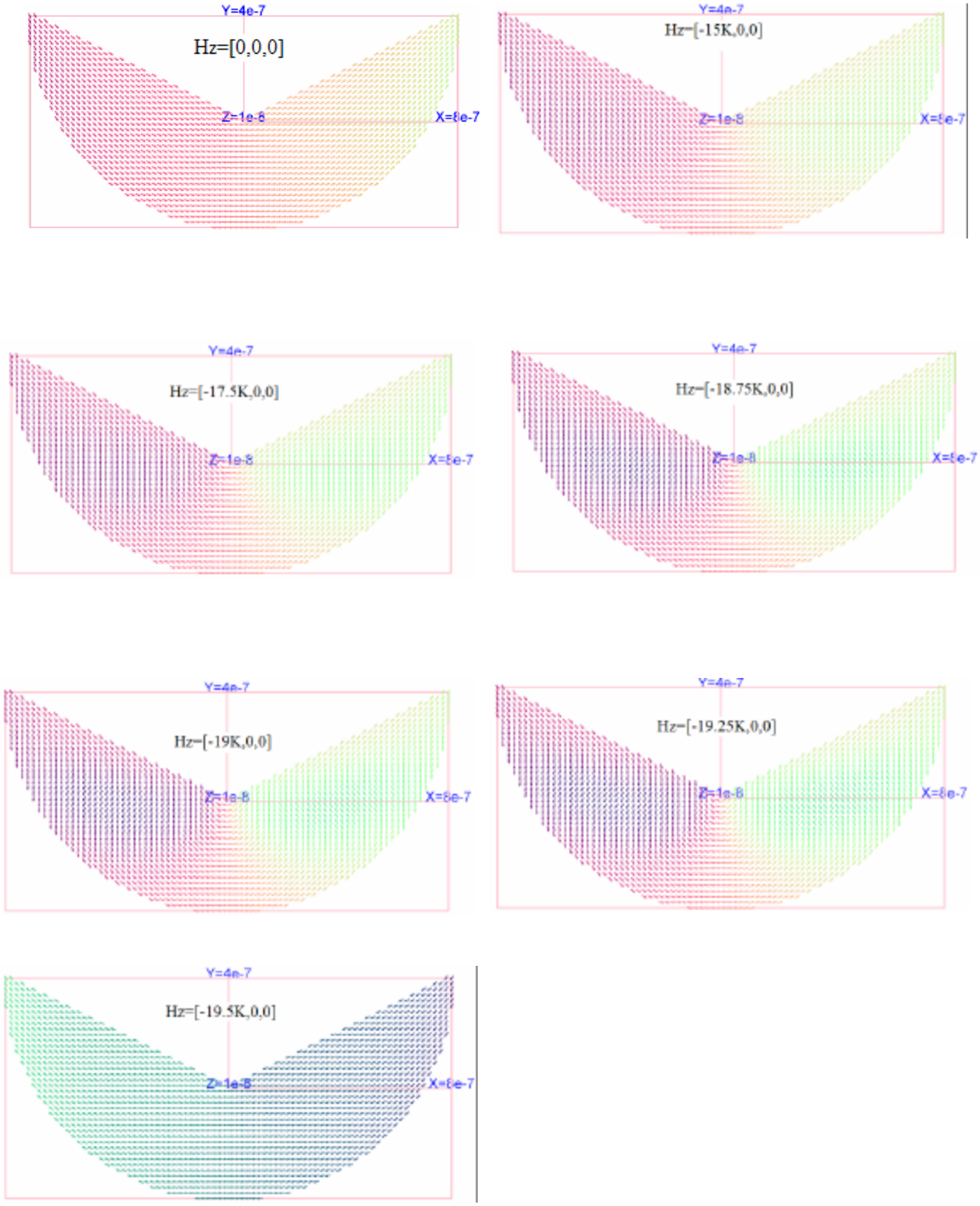

Figure 29. Domain configuration of the PM II element in hysteresis

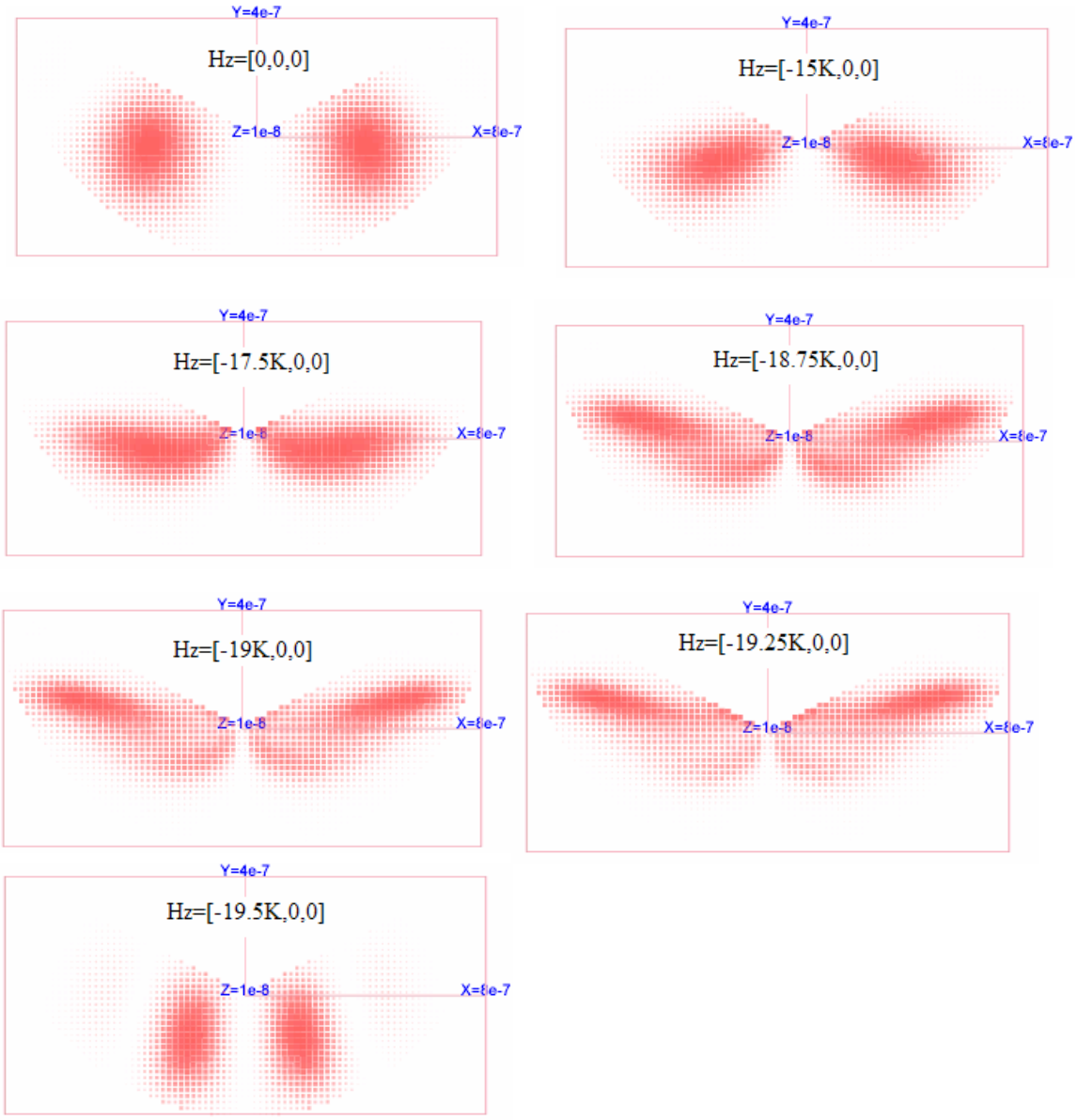

Figure 30. Torque map of the PM II element in hysteresis

An interesting result for these magnetic elements is that the internal energy profile is relatively flat in the hysteresis loop, except near the switching event, as shown in Figure 31. The direct consequence is that the spontaneous flipping of spins is difficult. Thus, the remanent “C” state and reversed remanent “C” state are thermodynamically separated.

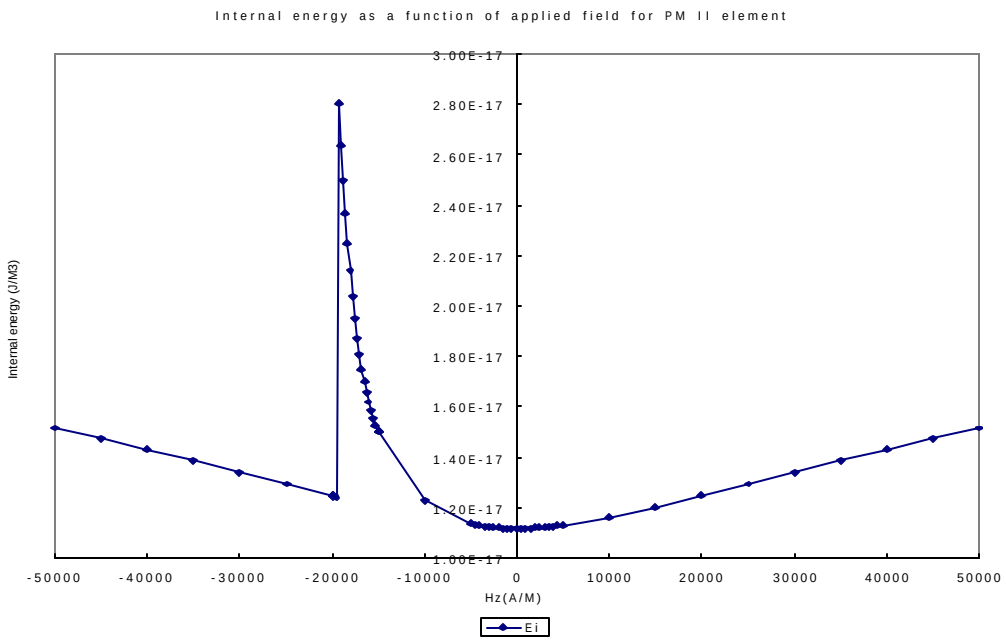

Figure 31. Internal energy as a function of the applied field in the PM II hysteresis

5.4 Conclusions

Compared with the experimental and simulation results of PM I and PM II elements from Ref. 46 with different geometric parameters, the results demonstrate that thinner element is found to have a hysteresis curve more suitable for MRAM devices. The PM I element switches over a large range of applied field through local nucleation and vortex core formation and movement, while the PM II element lacks the vortex core formation due to its larger aspect ratio. The reversal process of PM II element is a one-stage jump occurring in a very narrow applied field range. The distribution of torque for the PM II element is broader than that for the PM I element. The internal energy profile of the PM II element is flat with a sharp peak. These properties suggest that the PM II element is favored for MRAM applications. Thus, as indicated by Ref. 46, a PM II element is suitable candidate for an MRAM device.

Chapter 6 Hysteresis of FM-FM coupled core-shell Spheres

6.1 Exchange Spring Core-Shell

Magnetic multilayers, especially those composed of alternating soft and hard magnetic layers, are attracting interest due to their potential exploitation as high-performance magnets.[47] In these structures the exchange interaction at the interface plays an important role in the magnetization process through the pinning of the soft layer magnetization to the hard layer interface. When the soft layer is thick enough to form a Bloch wall, the spins in the soft layer can rotate reversibly during the magnetization process. Such materials are referred as "exchange spring" magnets. A theory of the soft layer switching behavior has been developed.[48] For "exchange spring" materials, the soft layer nucleation field is inversely proportional to the square of the soft layer thickness. When the soft layer is thin, no Bloch wall will form and the soft and hard layers are exchange coupled and reverse cooperatively.[49] Micromagnetic simulations have been performed on the exchange coupled ferromagnetic nanolayers.[50,51] Hysteresis in layered spring magnets has been investigated by numeric modeling through the integration of the LLG equation.[52] The nucleation field is inversely proportional to the soft layer thickness for a thin soft layer, to the square of the soft layer thickness for a thick soft layer, or to the soft layer thickness raised to a negative power between 1 and 2. The First Order Reversal Curve (FORC) method can be used to examine the irreversible field beyond which the

magnetization does not reverse.[53] The Kerr effect has also been used to study exchange coupling in multilayers.[54]

This work focuses on exchange coupling in nano particles with a core-shell structure, rather than multilayer thin films. Core-shell nano particles can be prepared though self-assembly, [55] deposition in oxidative atmosphere, through simultaneous reduction of metal salts or thermal decomposition of organometallic components in the presence of mixed surfactants.

The core-shell structure studied in this project contains a hard magnetic material and a soft magnetic material. It should not be confused with the high performance hard-soft composite magnets[56]. The later is an intergranular alloy that is composed of grains of high coercivity hard magnetic material mixed with grains of high saturation magnetization soft magnetic materials. The principle interaction in the hard-soft composite magnet is the intergranular exchange coupling between neighboring hard and soft grains. The core-shell structure has only one hard-soft interface and the interaction on the interface is due to spin exchange coupling.

6.2 Parameters of the Core-Shell Structure

Five core-shell structures are investigated in this project. Every structure has a cobalt core covered with a permalloy shell. The nano particles are 210nm diameter spheres bound by a $21\times21\times21$ grid. Figure 32 illustrates the geometry shapes of the core-shell structures.

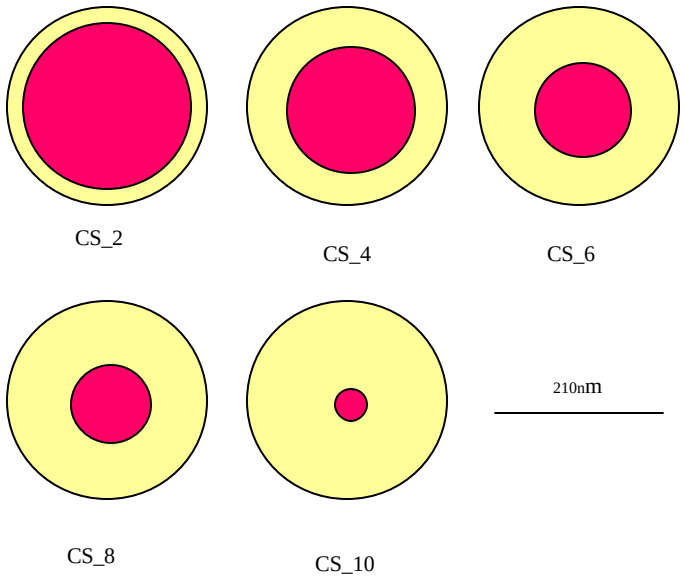

Figure 32. Core-Shell structure

Each cell is a 10nm cube. For each particle, the uniaxial cobalt core has an easy axis in +Z direction. The permalloy shell has no anisotropy. The thickness of the permalloy shell varies from 20nm to 100nm, at a 20nm interval. The structures correspond to shell to sphere volume ratios of 2060/4169(49%), 3244/4169(78%), 3912/4169(94%), 4135/4169(99%) and 4168/4169(100%) respectively.

Standard micromagnetics parameters of the cobalt and permalloy elements were used in the modeling, as shown in Table 7. The exchange coupling between cobalt and permalloy cells on the core-shell interfaces was assumed to be ferromagnetic-ferromagnetic (FM-FM) coupling. The coupling constant was taken to be the geometric average of the exchange stiffness of the two elements. The damping constant is 0.5 for both materials. The maximum allowed step size is 0.4. It is equivalent to 2.10ps for permalloy or 1.29ps for cobalt. The maximum magnitude of torque has been used as convergence criterion. The maximum allowed torque is 10^{-5} in reduced units. It is

equivalent to $24.6\ {}^{J}/_{M^3}$ for cobalt or $9.29\ {}^{J}/_{M^3}$ for permalloy. A uniform initial spin pattern has been applied to all structures. The initial spins for both the cobalt and the permalloy elements are initially aligned to the easy axis of the cobalt element.

Table 7. Parameters of the core-shell structures

Material	$Ms\left({}^{A}/_{M}\right)$	$A\left({}^{J}/_{M}\right)$	$A_{ij}\left({}^{J}/_{M}\right)$	$K_1\left({}^{J}/_{M^3}\right)$	a	$\Delta t_{\max}$	$t_{\max}$
Cobalt	1.4×10^{6}	3.0×10^{-11}	2.0×10^{-11}	5.2×10^{5}	0.5	0.4 $(1.29ps)$	10^{-5}degree $\left(26.4\ {}^{J}/_{M^3}\right)$
Permalloy	8.6×10^{5}	1.3×10^{-11}		0	0.5	0.4 $(2.10ps)$	10^{-5}degree $\left(9.29\ {}^{J}/_{M^3}\right)$

6.3 Hysteresis of the Core-Shell Structure

The external magnetic field has been applied in the Z direction, varying from 400K ${}^{A}/_{M}$ (5.03KOe) to -400K ${}^{A}/_{M}$ (-5.03KOe) with 400K ${}^{A}/_{M}$ to 200K ${}^{A}/_{M}$ scanned at 40K ${}^{A}/_{M}$ interval, 200K ${}^{A}/_{M}$ to 100K ${}^{A}/_{M}$ scanned at 10K ${}^{A}/_{M}$ interval and 100K ${}^{A}/_{M}$ to -100K ${}^{A}/_{M}$ scanned at 5K ${}^{A}/_{M}$ interval.

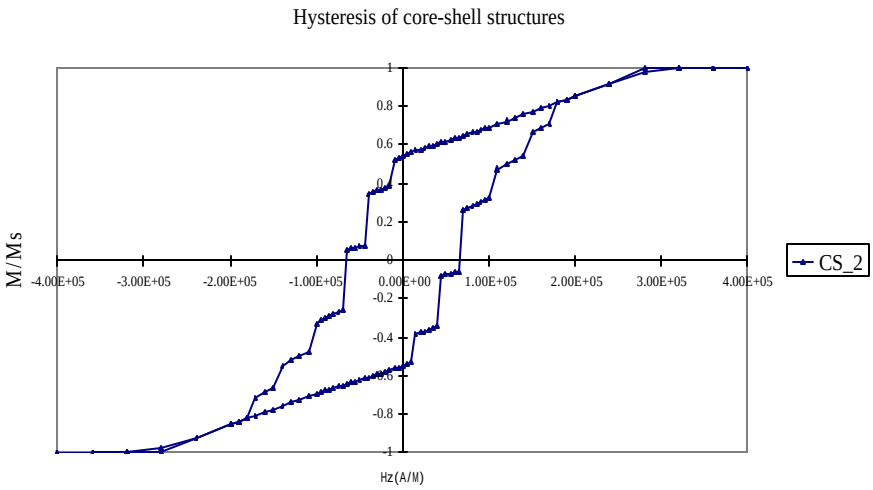

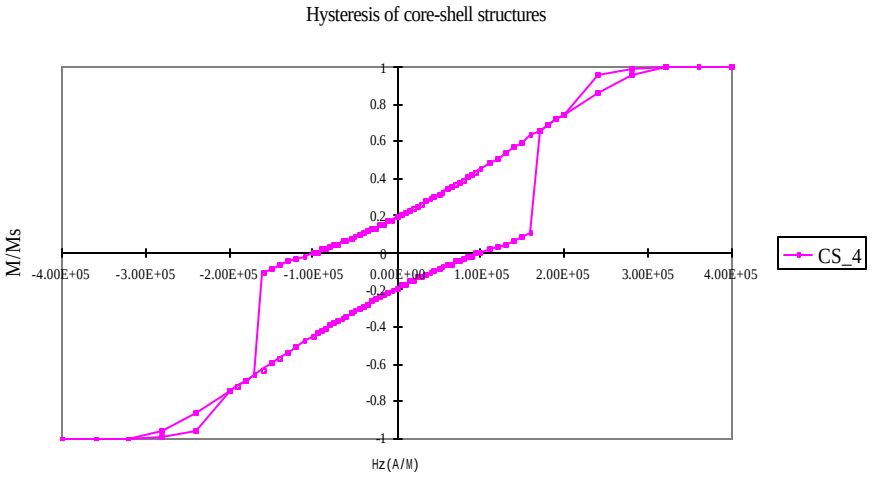
Hysteresis of core-shell structures
M/Ms
Hz(A/M)
CS_4
1
0.8
0.6
0.4
0.2
0
-0.2
-0.4
-0.6
-0.8
-1
-4.00E+05
-3.00E+05
-2.00E+05
-1.00E+05
0.00E+00
1.00E+05
2.00E+05
3.00E+05
4.00E+05

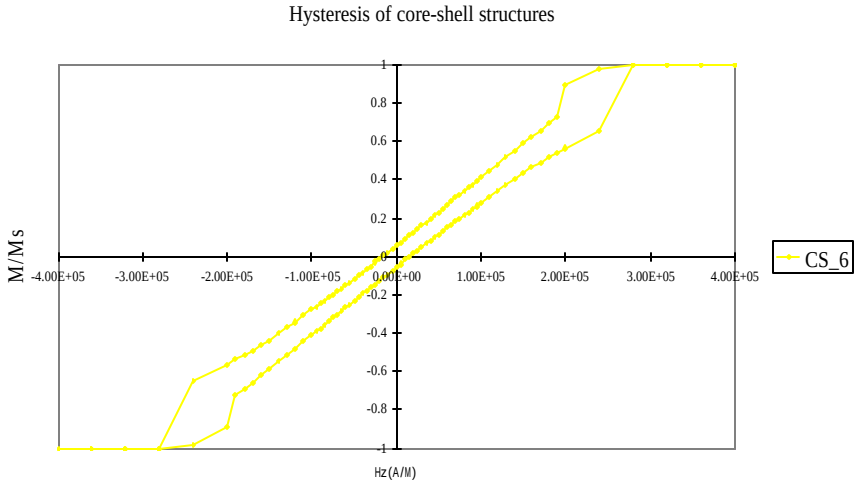
Hysteresis of core-shell structures
M/Ms
Hz(A/M)
CS_6
1
0.8
0.6
0.4
0.2
0
-0.2
-0.4
-0.6
-0.8
-1
-4.00E+05
-3.00E+05
-2.00E+05
-1.00E+05
0.00E+00
1.00E+05
2.00E+05
3.00E+05
4.00E+05

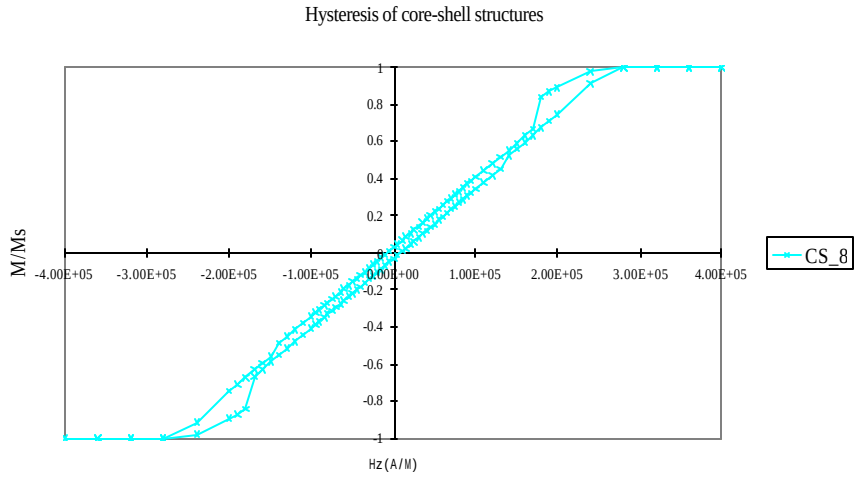
Hysteresis of core-shell structures
M/Ms
Hz(A/M)
CS_8
1
0.8
0.6
0.4
0.2
0
-0.2
-0.4
-0.6
-0.8
-1
-4.00E+05
-3.00E+05
-2.00E+05
-1.00E+05
0.00E+00
1.00E+05
2.00E+05
3.00E+05
4.00E+05

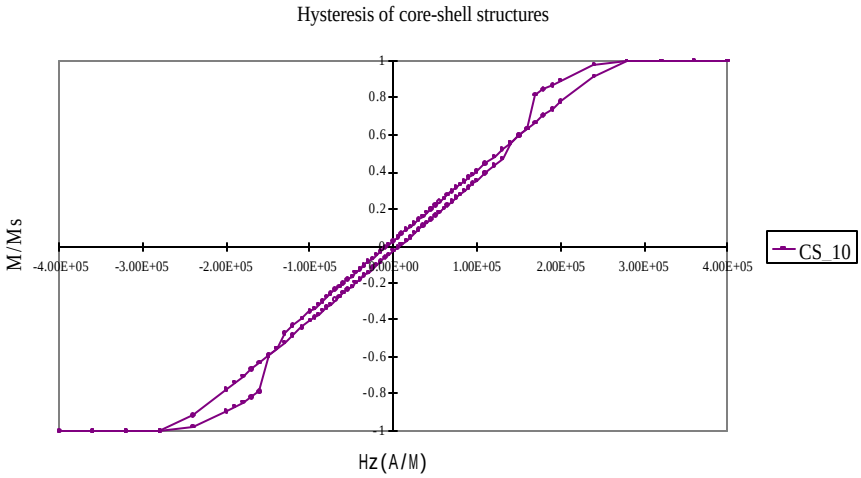

Figure 33. Hysteresis of the core-shell structure. CS_2, CS_4, CS_6, CS_8 and CS_10 correspond to the normalized Z magnetization component of particles with shell thickness 20nm, 40nm, 60nm, 80nm and 100nm respectively.

Figure 33 shows the hysteresis loops of all particles. Although the particles with different shell thickness have the same number of total cells, the saturation magnetization for different particles is different due to different compositions of the two elements. In the hysteresis loop of each particle, the magnetization has been normalized to its saturation value.

6.3.1 Remanent state domain pattern

Table 8. Core-Shell structure remanent state statistics

Item	CS_2	CS_4	CS_6	CS_8	CS_10	Remark
Ncell	4169	4169	4169	4169	4169	total number of cells
Nco	2109	925	257	34	1	number of co cells
Npy	2060	3244	3912	4135	4168	number of py cells
Vco%	50.59%	22.19%	6.16%	0.82%	0.02%	co cell volume percentage
Vpy%	49.41%	77.81%	93.84%	99.18%	99.98%	py cell volume percentage
Mco/Ms,co	1961.18	904.76	253.14	32.39	1.00	reduced co magnetization
Mpy/Ms,py	-240.53	-571.03	-172.40	74.11	110.76	reduced py magnetization
mco	92.99%	97.81%	98.50%	95.25%	100.00%	co alignment percentage
mpy	-11.68%	-17.60%	-4.41%	1.79%	2.66%	py alignment percentage
Pco%	58.12%	31.01%	9.52%	1.26%	0.04%	co magnetization percentage
Ppy%	-4.38%	-12.02%	-3.98%	1.77%	2.66%	py magnetization percentage
Ms(A/M)	4.72E+09	4.08E+09	3.72E+09	3.60E+09	3.59E+09	total saturation magnetization
M(A/M)	2.54E+09	7.76E+08	2.06E+08	1.09E+08	9.67E+07	total remanence
m	0.537	0.190	0.055	0.030	0.027	total reduced magnetization
Ee,co(J)	9.68E-17	2.62E-17	4.94E-18	9.80E-19	5.15E-20	co exchange energy
Ee,py(J)	1.19E-16	1.03E-16	5.54E-17	4.21E-17	4.12E-17	py exchange energy
Ed,co(J)	4.11E-16	8.61E-17	1.89E-17	3.43E-18	1.50E-19	co demag energy
Ed,py(J)	-4.61E-17	-1.64E-17	1.51E-17	2.58E-17	2.80E-17	py demag energy
Eco(J)	6.37E-16	1.33E-16	2.77E-17	5.04E-18	2.02E-19	co total energy
Epy(J)	7.29E-17	8.63E-17	7.06E-17	6.79E-17	6.92E-17	py total energy
Eco%	89.74%	60.57%	28.22%	6.91%	0.29%	co total energy percentage
Epy%	10.26%	39.43%	71.78%	93.09%	99.71%	py total energy percentage
E(J)	7.10E-16	2.19E-16	9.83E-17	7.29E-17	6.94E-17	total energy

The core-shell structure is similar to exchange-coupled multilayers[54] in terms of magnetic properties. The remanence of the core-shell structure reveals strong composition dependence. Table 8 summarizes the statistics of remanent states of all particles. While the cobalt cells align in +Z direction at the remanent state, the permalloy spins near the interface are exchange coupled to the core and tend to align in the same direction. However, the coupling extends to only one or two layers in the soft magnetic material. The outmost permalloy spins either align horizontally to form vortexes in the horizontal cross-section or align in the –Z direction. Due to angular symmetry, the X and Y components of magnetization of all particles in the hysteresis are virtually zero. The alignment percentage is calculated as the ratio of the total Z magnetization component of a material to the expected magnetization if all spins of the material align to the Z direction. A negative alignment percentage means the spins align to the –Z direction. The

alignment percentage of cobalt shows a peak at a shell thickness of 60nm, or a cobalt core diameter of 90nm. The alignment percentage of permalloy shows a minimum at a shell thickness of 40nm. For thinner shells, the alignment percentage of permalloy is negative, in order to offset the positive cobalt magnetization. Notably, the surface magnetization, which is composed of a contribution from permalloy only, is in the –Z direction for thinner shells as can be seen in Figure 34. The magnetization percentage denotes the ratio of the total Z magnetization component of a material to the total magnetization of the entire sample. At the remanent state, the cobalt spins are well aligned. Thus, the cobalt magnetization percentage decreases when volume percentage of cobalt decreases. The permalloy magnetization percentage for thinner shells is negative, in agreement with the alignment percentage of the thinner shells. Although the volume percentage of thick shells CS_6, CS_8 and CS_10 are greater than 90 percent, the net magnetization contribution form the permalloy spins is very small, because the permalloy spins in the thick shell tends to form closure domains at zero field. A domain wall in the permalloy shell is found in all particles. With the increase of the shell thickness, the domain wall thickness also increases. The center of the vortex moves towards the core when the shell thickness increases but stops at a position half way to the core for thicker shells. The total energy contribution from permalloy cells is insensitive to the increase of the number of cells, since their exchange energy decrease is offset by the increase in magnetostatic energy. Interestingly, 180 degree domain wall is achieved in thin shell structures, but not in thick shell structures. The latter builds 90 degree Bloch wall instead.

From the top view of the cross-section of the remanent states, the equators of the spheres always form vortices, either clockwise or counterclockwise. Stronger exchange

coupling in the cobalt interface cells is found for thin shells, where the horizontal components for those cells also form vortices. The radial distribution of the rotation angles in the cobalt cells is obvious, as in Figure 34. (The magnitudes of the arrows are proportional to the horizontal components of the spins in top view of the cross-sections).

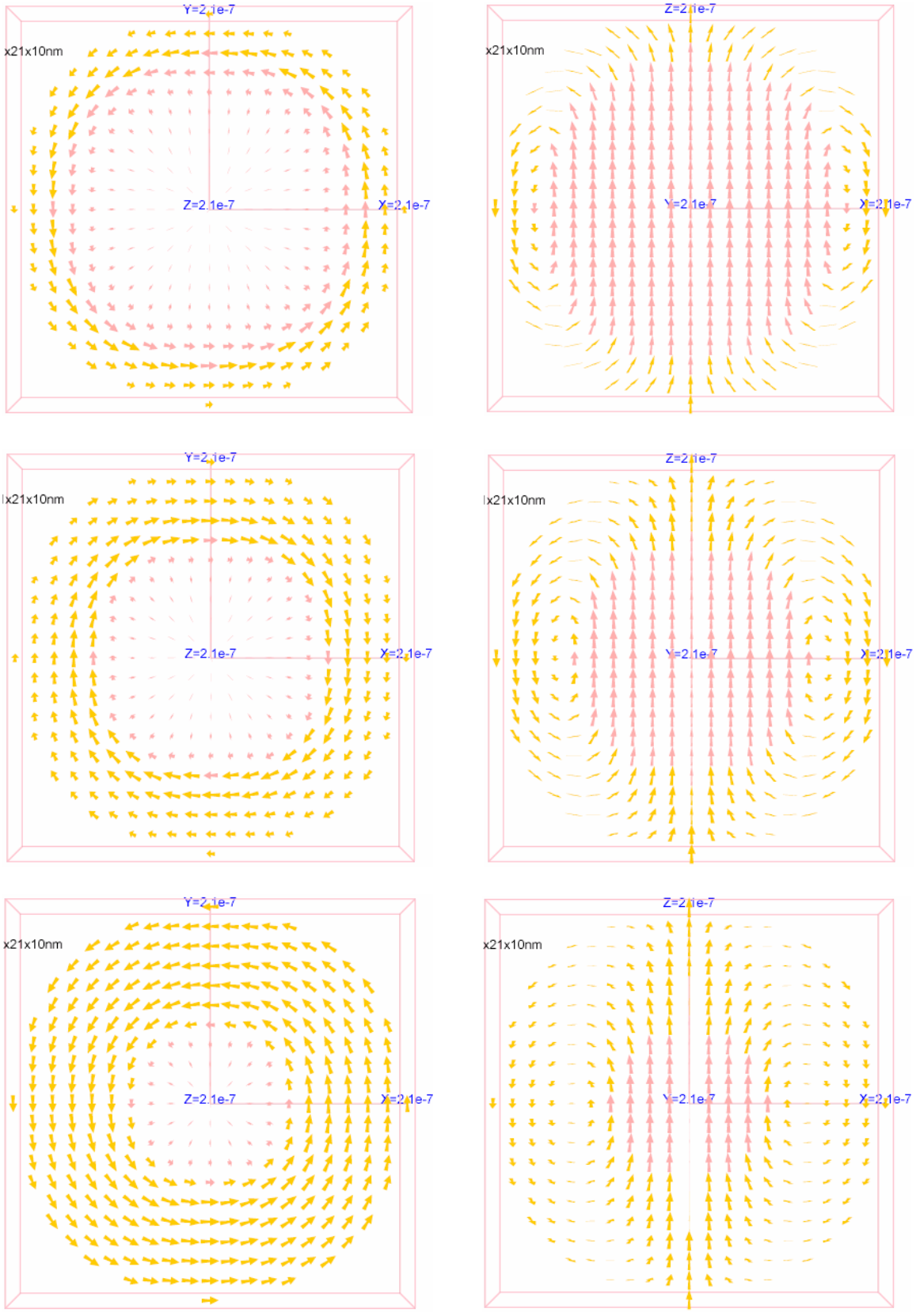
Y=2.1e-7
x21x10nm
Z=2.1e-7
X=2.1e-7
Z=2.1e-7
x21x10nm
Y=2.1e-7
X=2.1e-7
Y=2.1e-7
x21x10nm
Z=2.1e-7
X=2.1e-7
Z=2.1e-7
x21x10nm
Y=2.1e-7
X=2.1e-7
Y=2.1e-7
x21x10nm
Z=2.1e-7
X=2.1e-7
Z=2.1e-7
x21x10nm
Y=2.1e-7
X=2.1e-7

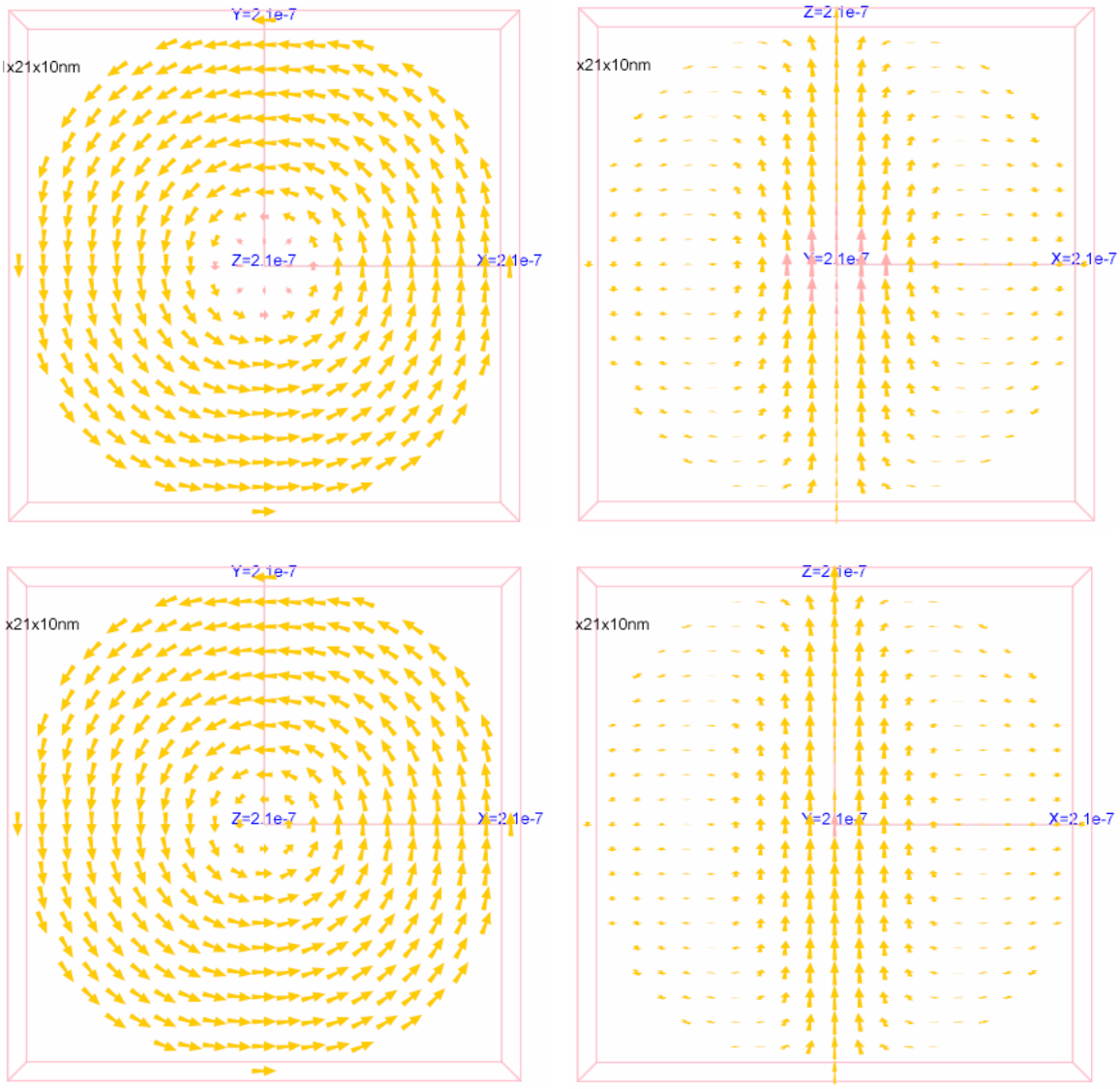

Figure 34. Remanent state domain patterns of the core-shell structure. Left: top view of the z=10 cross-section. Right: side view of the y=10 cross-section. From top down, the shell thickness is 20nm, 40nm, 60nm, 80nm and 100nm respectively.

6.3.2 Coercive state domain pattern

As to the remanent states, the same procedure of analysis has been applied to the coercive states. The statistics of the coercive states are summarized in Table 9. Compared to the remanent states, an apparent change is that the net magnetization contribution from permalloy cells are negative, in order to offset the positive contribution from cobalt cells

in the core. The alignment percentage of cobalt cells in the thick shell particles CS_6, CS_8 and CS_10 remain the same. Therefore a stronger applied field in –Z direction is needed to create a more negative net contribution to the magnetization from the permalloy cells. This explains the decrease of coercive field with the increase of shell thickness for the above three particles. The maximum coercive field occurs in the case of CS_4. In this case, a thick 180 degree Bloch wall is formed on the core-shell interface. Stronger external field is needed to align the permalloy spins near the core-shell interface to –Z direction. Although the cobalt spins on the interface participate in forming the domain wall, they are well aligned, just like the other core spins. Note a cycle of permalloy spins align horizontal to form a vortex. This is the center of the Bloch wall. For the thinnest shell particle CS_2, Bloch wall is not able to form in the soft magnetic material layer, thus, there is no Bloch wall in the coercive state. Some cobalt spins simply align anti-parallel to achieve magnetization transition in orientation. This results in the highest exchange energy in cobalt core. Consequently, the CS_2 particle has the smallest cobalt cell alignment percentage.

Table 9. Core-Shell structure coercive state statistics

Item	CS_2	CS_4	CS_6	CS_8	CS_10	Remark
Hz(A/M)	-65000	-100000	-15000	-10000	-5000	Coercive field
Mco/Ms,co	911.42	877.68	252.78	32.34	1.00	reduced co magnetization
Mpy/Ms,py	-1194.33	-1439.16	-396.36	-83.25	31.45	reduced py magnetization
mco	43.22%	94.88%	98.36%	95.13%	100.00%	co alignment percentage
mpy	-57.98%	-44.36%	-10.13%	-2.01%	0.75%	py alignment percentage
Pco%	27.01%	30.08%	9.50%	1.26%	0.04%	co magnetization percentage
Ppy%	-21.74%	-30.30%	-9.15%	-1.99%	0.75%	py magnetization percentage
M(A/M)	2.49E+08	-8.93E+06	1.30E+07	-2.63E+07	2.84E+07	total remanence
m	0.053	-0.002	0.003	-0.007	0.008	total reduced magnetization
Ee,co(J)	3.96E-16	4.89E-17	5.40E-18	1.05E-18	5.37E-20	co exchange energy
Ee,py(J)	5.60E-17	1.23E-16	5.83E-17	4.33E-17	4.18E-17	py exchange energy
Ed,co(J)	8.33E-17	5.20E-17	1.56E-17	3.14E-18	1.46E-19	co demag energy
Ed,py(J)	3.34E-18	-1.69E-18	1.65E-17	2.56E-17	2.77E-17	py demag energy
Eco(J)	7.53E-16	2.99E-16	3.20E-17	5.43E-18	2.08E-19	co total energy
Epy(J)	-2.45E-17	-3.46E-17	6.84E-17	6.80E-17	6.96E-17	py total energy
Eco%	103.37%	113.08%	31.88%	7.39%	0.30%	co total energy percentage
Epy%	-3.37%	-13.08%	68.12%	92.61%	99.70%	py total energy percentage
E(J)	7.28E-16	2.64E-16	1.00E-16	7.35E-17	6.98E-17	total energy

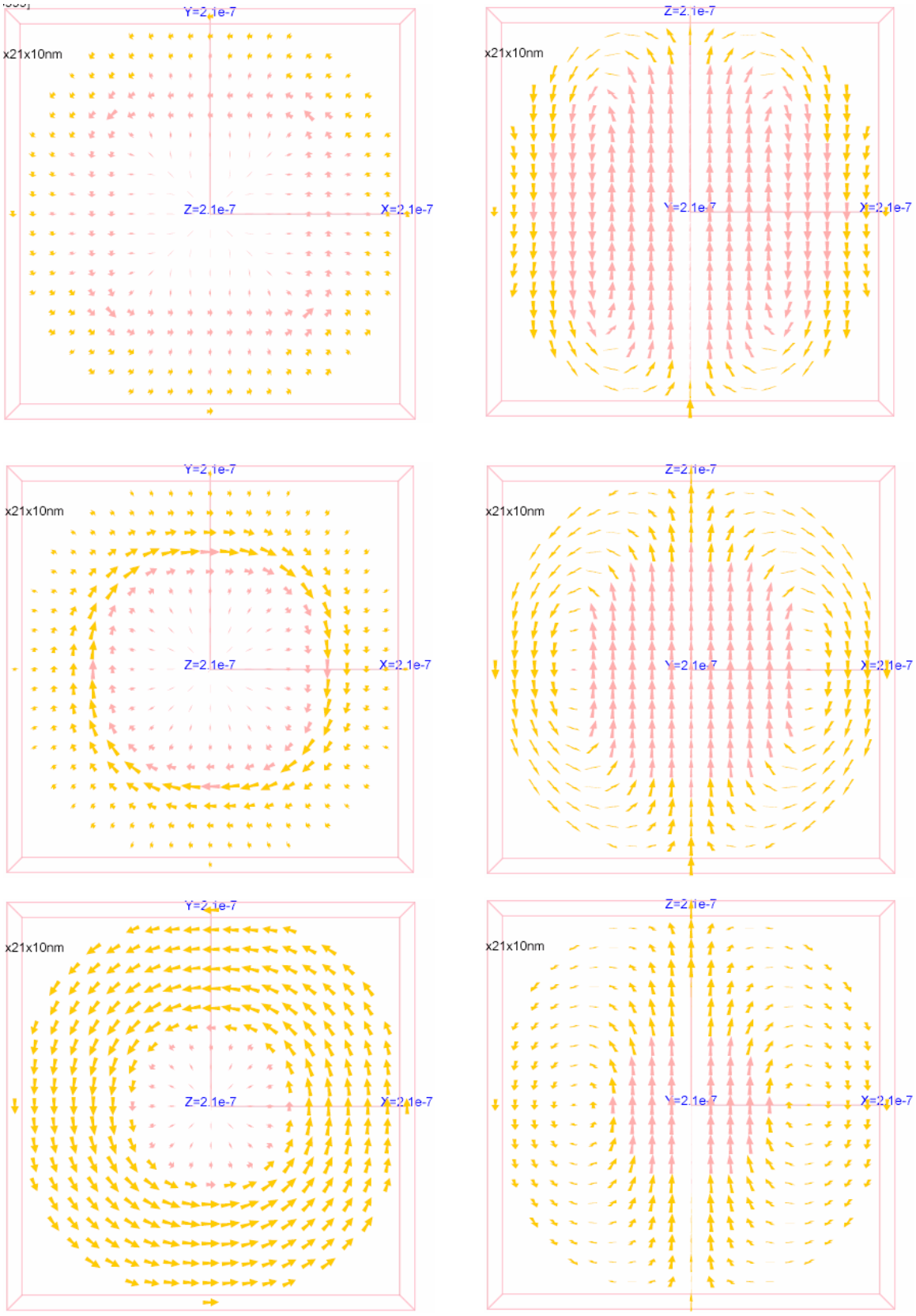
Y=2.1e-7
x21x10nm
Z=2.1e-7
X=2.1e-7
Z=2.1e-7
x21x10nm
Y=2.1e-7
X=2.1e-7
Y=2.1e-7
x21x10nm
Z=2.1e-7
X=2.1e-7
Z=2.1e-7
x21x10nm
Y=2.1e-7
X=2.1e-7
Y=2.1e-7
x21x10nm
Z=2.1e-7
X=2.1e-7
Z=2.1e-7
x21x10nm
Y=2.1e-7
X=2.1e-7

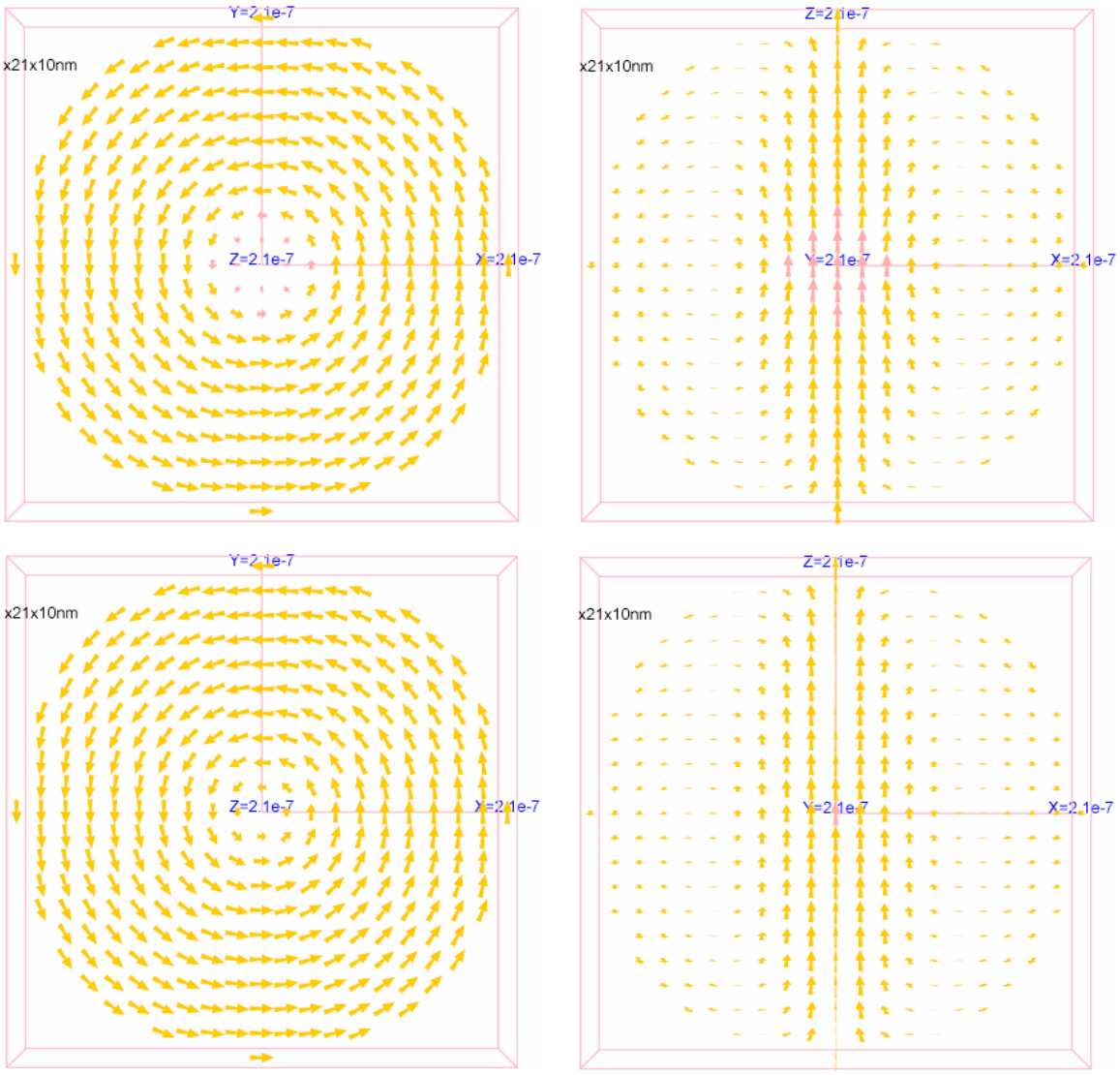

Figure 35. Coercive state domain patterns of the core-shell structure. Left: top view of the z=10 cross-section. Right: side view of the y=10 cross-section. From top down, the shell thickness is 20nm, 40nm, 60nm, 80nm and 100nm respectively.

6.3.3 Hysteresis of individual core-shell particles

Unlike FM-AFM exchange coupled multilayers, exchange bias is not found for all particles. This is probably due to the facts that the applied field is along the symmetry axis and the exchange coupling is FM-FM. The reversal process starts from the outmost permalloy cells. At the beginning of the reversal, the cobalt spins in the core align

uniformly in +Z direction. The permalloy spins align in the +Z direction, not uniformly, but form a flower state. For thin shells, the flower state also involves cobalt cells near the core-shell interface. The first stage of hysteresis is the rotation of the equator permalloy spins to form a horizontal vortex. With the reduction of the applied field, the outmost spins rotate to create a vertical closure. A domain wall is formed and moves towards the core of the sphere. The applied field associated with the formation of horizontal vortex in the equator is shell thickness dependent. It decreases along with the increase of the shell thickness. In a smaller applied field, the horizontal vortex contracts and moves towards the Z axis. The spins in the equator and the spins next to them rotate to align in –Z direction, in order to form a vertical closure domain. This movement results in a reduction of the magnetization. For thick shell particles, the reduction is gradual, as the smooth hysteresis curve reveals in Figure 33. For particle CS_2, no Bloch wall is formed. The movement of the vertical closure domain is fulfilled by the flipping of cobalt spins. Thus, the reduction of the magnetization is more abrupt. This accounts for the five step jumps in the hysteresis of CS_2. An important feature for the CS_2 particle is the movement of the equator spins. The spins are first aligned up, then align horizontally to form a counterclockwise vortex, then align down to participate in the vertical closure domain, then raise horizontal again to form counterclockwise vortex when the center of the vertical closure moves close to the Z axis and they are less influenced by the vertical closure. The spins eventually align down after the core flips in a strong reverse field.

For all particles, the last jump in the first half of hysteresis loop corresponds to the reversal of the cobalt core. The permalloy surface spins at the two axial poles (top and

bottom areas) flip right before the core flips, because they are exchange coupled with the already flipped surface spins. The domain patterns in the reversal are shown in Figure 36.

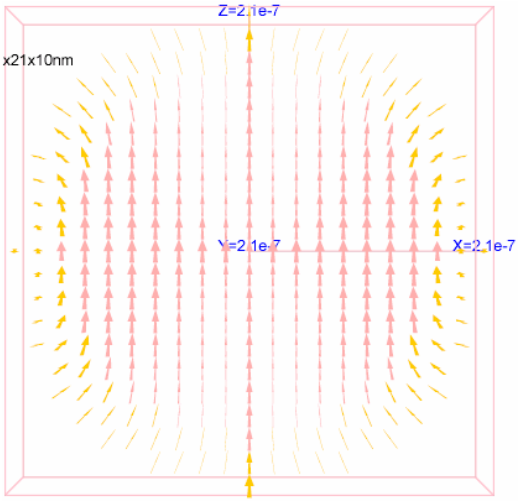
Z=2.1e-7
x21x10nm
Y=2.1e-7
X=2.1e-7

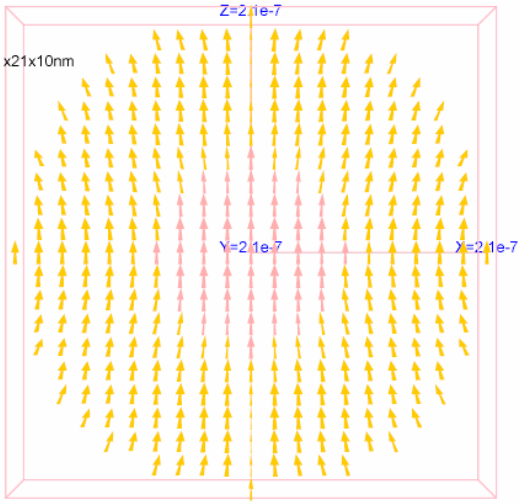
Z=2.1e-7
x21x10nm
Y=2.1e-7
X=2.1e-7

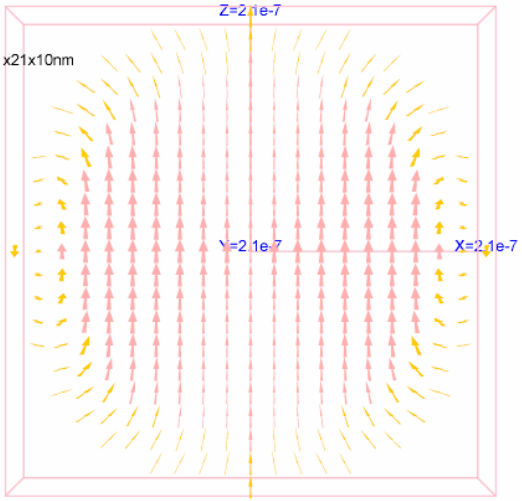
Z=2.1e-7
x21x10nm
Y=2.1e-7
X=2.1e-7

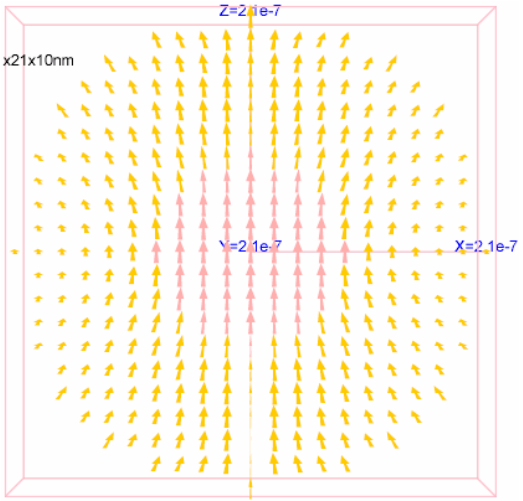
Z=2.1e-7
x21x10nm
Y=2.1e-7
X=2.1e-7

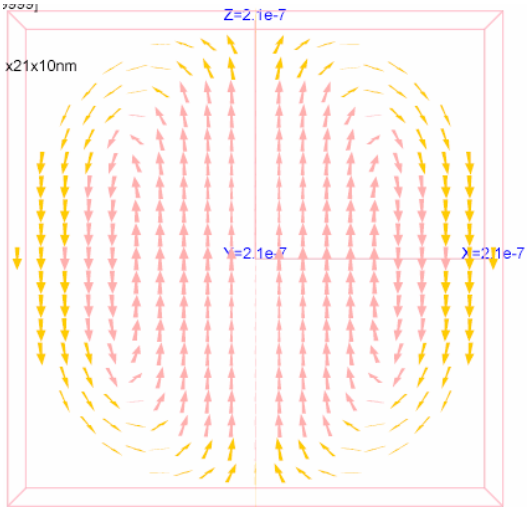
Z=2.1e-7
x21x10nm
Y=2.1e-7
X=2.1e-7

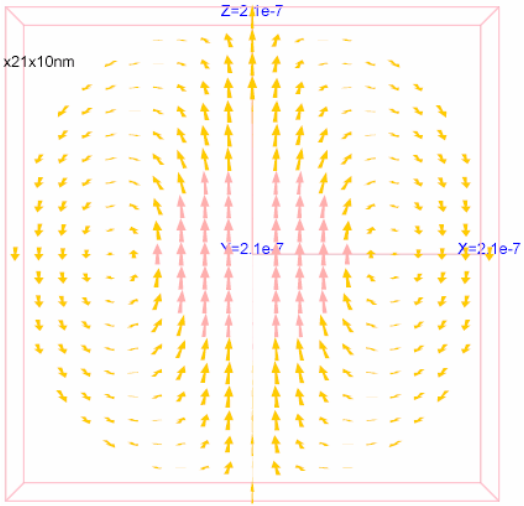
Z=2.1e-7
x21x10nm
Y=2.1e-7
X=2.1e-7

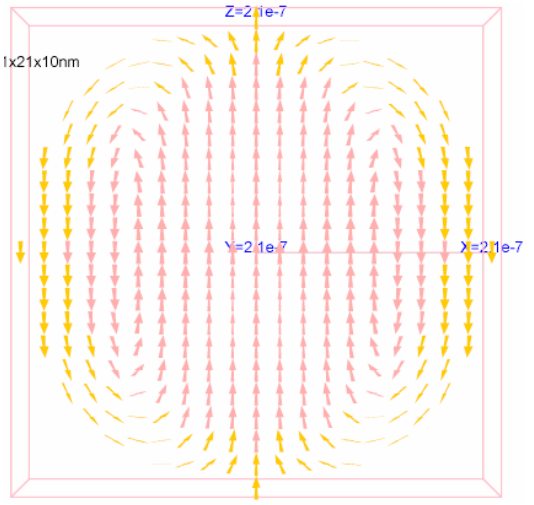
Z=2.1e-7
1x21x10nm
Y=2.1e-7
X=2.1e-7

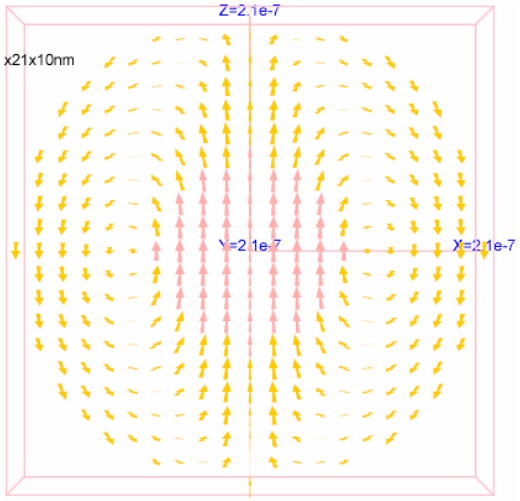
Z=2.1e-7
x21x10nm
Y=2.1e-7
X=2.1e-7

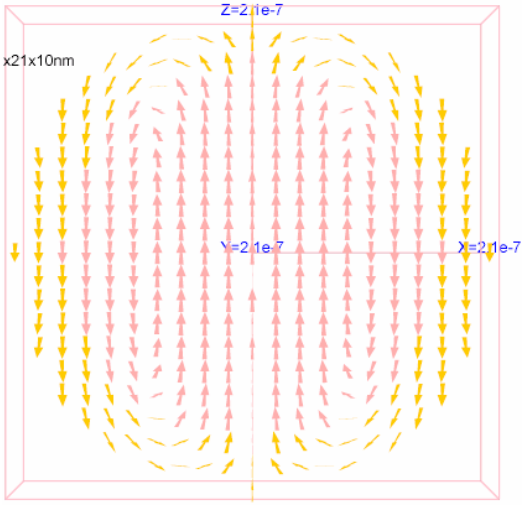
Z=2.1e-7
x21x10nm
Y=2.1e-7
X=2.1e-7

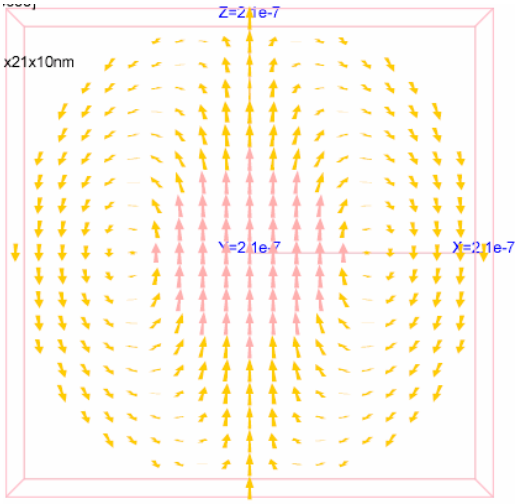
Z=2.1e-7
x21x10nm
Y=2.1e-7
X=2.1e-7

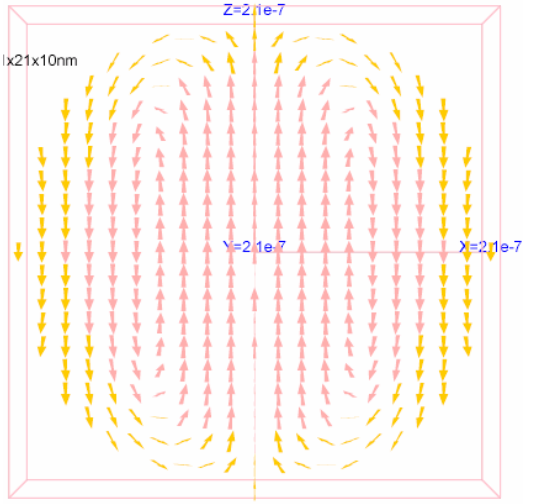
Z=2.1e-7
x21x10nm
Y=2.1e-7
X=2.1e-7

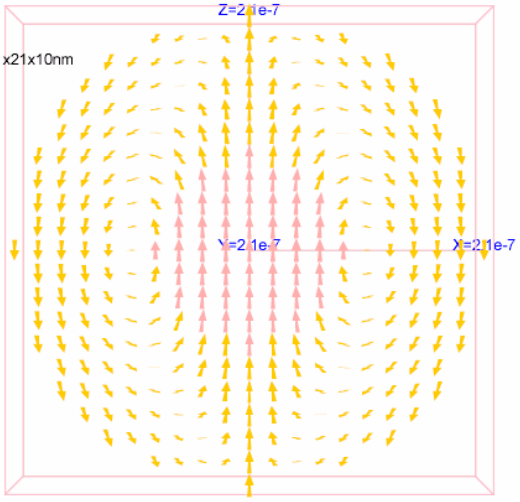
Z=2.1e-7
x21x10nm
Y=2.1e-7
X=2.1e-7

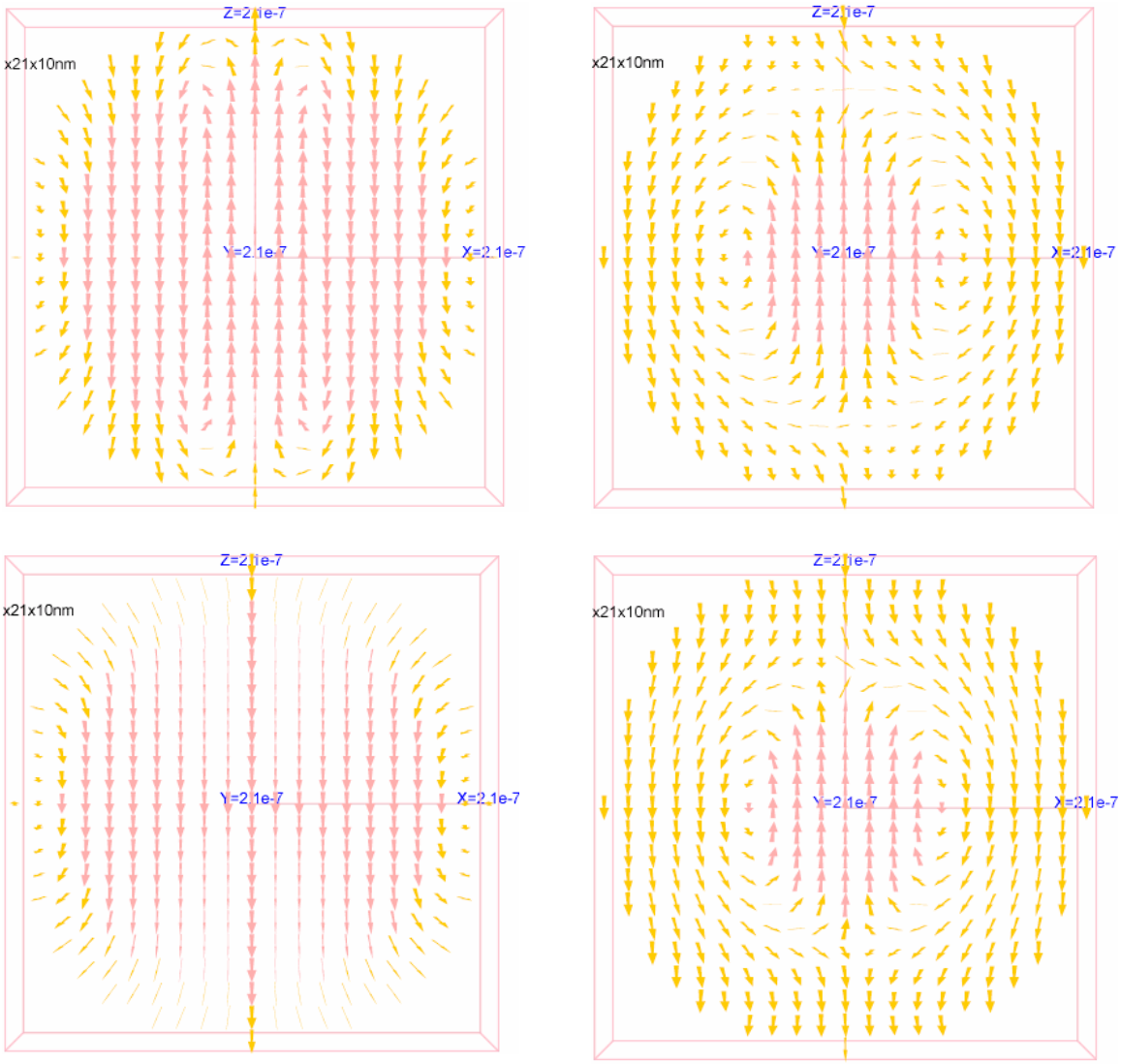

Figure 36. Domain pattern of the core-shell particles in hysteresis. Left: side view on the y=10 cross-section of the CS_2 particle. Right: side view on the y=10 cross-section of the CS_6 particle. From top down, the applied field is 200K A/M, 150K A/M, -15K A/M, -55K A/M, -65K A/M, -100K A/M, -150K A/M and -200K A/M in +Z direction respectively.

The spin configuration in the particles should not be confused with bidomains, because the domain configuration is rotational symmetric. In the thin shell particle, the reversal is through the movement of the center of the vertical closure domain towards the Z axis. No uniform or coherent reversal in the cobalt core is observed. In the thick shell

particles, the spins in the soft permally shell have more freedom in motion. Most of the domain pattern changes occur in the soft magnetic material region. The vertical closure domain consists permalloy spins only. The center of the vertical closure domain in the z=10 cross-section moves towards the Z axis, but the movement stops when it meets the hard-soft material interface, because the spins in the hard material are tightly coupled through exchange and no orientation other than vertical are preferred due to the strong anisotropy field. Alternatively, the spins in the vertical closure domain above and below the Z=10 cross-section still find a path in the soft magnetic material region to move toward the Z axis. The top and bottom ends of the vertical closure center merges when all spins in the soft magnetic material region flip. At this time the surface spins at the poles flip under the influence of exchange coupling. Thus, the hard magnetic material region, or the cobalt core, is surrounded by the reversed spins of soft magnetic material and it flips, to a large extent, coherently. The applied field at which the core flips depends on the radius of the core. It increases along with the shell thickness for thin-shell particles where the reversal mechanism involves no Bloch wall. The peak is found for CS_6 particle. It decreases when the core radius decreases for thick-shell particles where the reversal mechanism involves movement of the Bloch wall center and the coherent reversal of the core. The corresponding values are around 150, 160, 240, 150 and 140K $A/_M$ for the CS_2, CS_4, CS_6, CS_8 and CS_10 particles, respectively. Note the tend in reversal field change for the core is in agreement with the cobalt alignment percentage in the remanent and coercive states (Table 8 and 9). This explains the change in cobalt alignment percentage, as it is influenced by whether the Bloch wall is formed or not in the reversal.

The coercive field also has a maximum. It is for the CS_4 particle, rather than for the CS_6 particle, due to the higher remanence. CS_4 has a reversal mechanism with some characteristics of the reversal mechanism of CS_2 and some characteristics of the mechanism of CS_6.

Not surprisingly, for all particles, the cobalt spins on the hard-soft interface have higher exchange energy than other spins at the remanent state. But, after the formation of the vertical closure, the eye of the closure domain has the highest exchange energy, regardless weather the exchange is between the permalloy spins, between the cobalt spins or between the permalloy spins and the cobalt spins. However, the region with the maximum magnitude of torque is not associated with the region with the maximum exchange torque. In most cases, the region with the maximum torque is located in the soft magnetic material where the spins are oriented horizontal, in other words, perpendicular to the applied field. This region is the equator at early steps of the hysteresis, coincides with the eye of the vertical closure in the middle of the reversal process, or on the surface of the hard cobalt core at very late steps of the hysteresis, when the core is ready to flip. Despite the variation in the nucleation field, the switching field and switching field distribution for all particles are found to be more or less equal. The switching field is basically determined by permalloy. Furthermore, the permalloy shell acts as a “buffer” that isolates the hard material core from the external field.

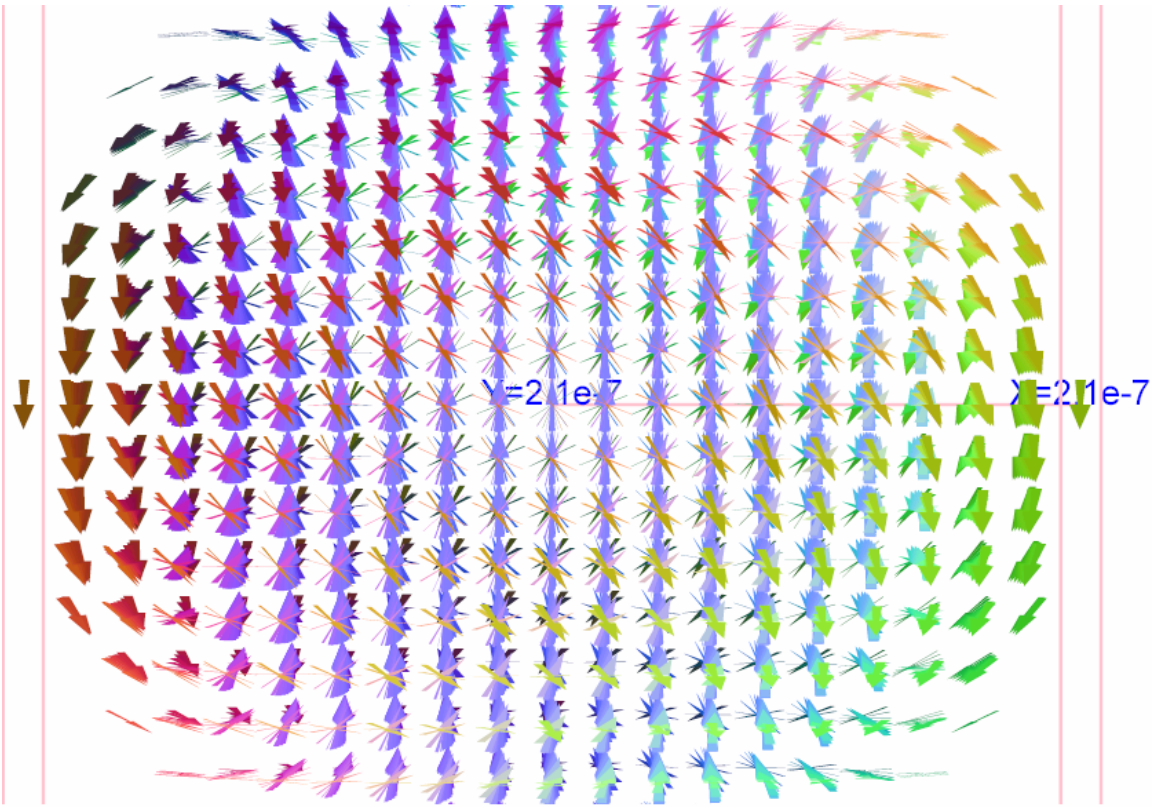

Figure 37. The spin configuration in the remanent state of CS_2 particle. This is a side view. The spins with the same X and Z coordinates appear one on top of the other. The hard cobalt core is in uniform spin magnetization with slight deviation. Radial angle distribution is apparent. The surface spins, exclusively permalloy, are in the opposite direction from the core.

The characteristic rotation of the spins in soft magnetic material in thin-film exchange-spring magnets is observed in the core-shell structure. Figure 37 shows a global view of the rotation and radial angular distribution of the orientation of spins. This is the prospective side view of all spins in the CS_2 particle at the remanent state. Besides rotational symmetry, the X and Y components of magnetization also show point reflective symmetry. The two symmetry properties exist in all spin configurations in the reversal for all particles. Another associated characteristic, the oscillation of the spin orientation normal to the hard-soft interface is also observed.

An interesting observation is for the thin-shell particles CS_2 and CS_4, the magnetization in the first half and the second half of the hysteresis loop is exactly the same for the applied filed ranging between $\pm 180 \mathrm{K}\, A/M$ and $\pm 200 \mathrm{K}\, A/M$. However, the direction of the horizontal vortices formed by the spins in the eye of the vertical closure domain, or the surface permalloy spins, as shown on the horizontal cross-sections, has been changed.

It changed from counterclockwise to clockwise for CS_2 and from clockwise to counterclockwise for CS_4. This change is due to the continuous rotation of the spins in the areas after saturation when the applied field reverses. This change does not affect the magnetization and the total energy in the aforementioned applied field range, but it does change the curve of the hysteresis in the successive steps. In the successive steps, the magnetization of the core is in the reversed direction, which prefers a reversed vortex.

Remarkably, the hysteresis curves of the core-shell particles, whether they are smooth or piecewise, are convex functions, contrary to the normal concave functions. In other words, the second derivative of the magnetization with respect to the applied field $\frac{\partial^2 M}{\partial H^2}$, is positive. The reason is not clear, but possibly is due to a “buffer” effect since the core is not as sensitive as the shell to the applied field.

6.4 Comparison with a Soft-Soft Core-Shell Sphere

For comparison, another core-shell particle was modeled. This is a sphere with 150nm radius. The core is a permalloy sphere with 140nm radius and the shell is soft cobalt. To simulate the polycrystalline structure of cobalt, the cobalt is assumed to have no effective anisotropy. Other than this constraint, the other magnetic properties of the two materials, including the coupling exchange constant, are exactly the same as those in Table 7. The modeling was done with 5nm cubic cell. Other program control parameters are similar to the parameters for the modeling of the hard-soft core-shell structure.

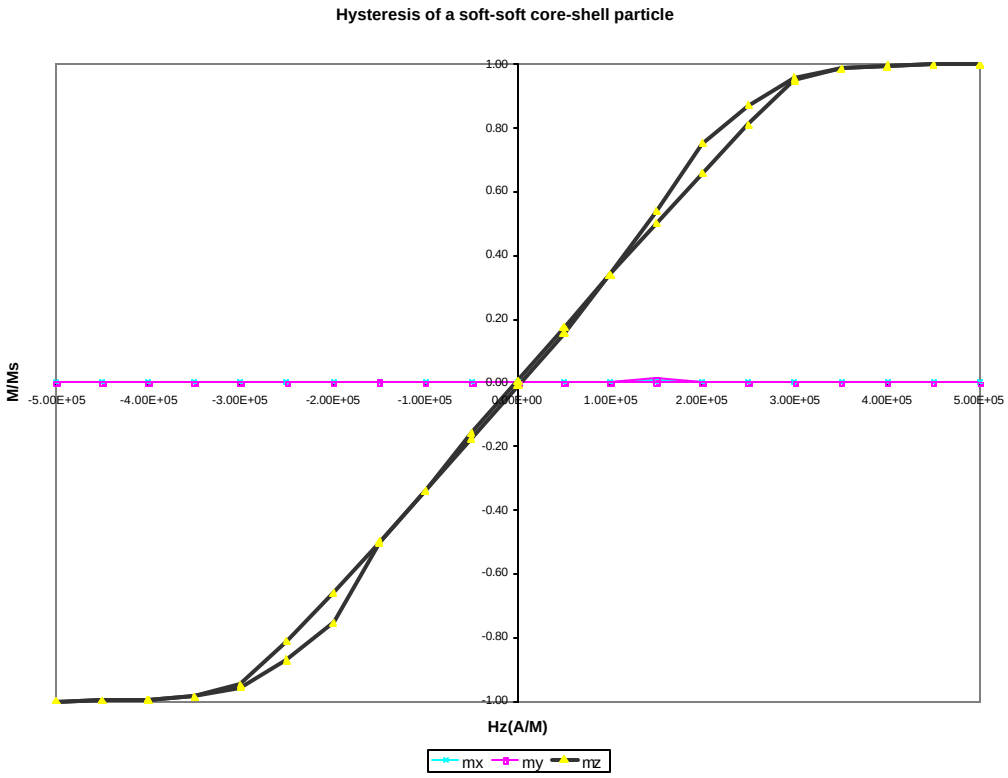

Figure 38. Hysteresis of a soft-soft core-shell particle

The soft-soft core-shell particle shows no remanence at zero field. The coercive field is also zero. The hysteresis is similar to the hysteresis of the CS_10 particle, as shown in Figure 38. However, the reversal mechanism is quite different. In the particle,

no crystalline anisotropy exists and the soft-soft interface is not as important as a hard-soft interface. The cobalt spins in the shell are exchange coupled with the permalloy spins in the core and the spins in two different materials act as a unit as if the soft-soft interface does not exist. The particle reverses through nucleation in the interior of the core. At first, one nucleation is formed on one side. The X and Y components of the magnetization form a horizontal vortex which spans only a few cells. A domain wall between the vortex and the remaining spins is formed and the domain wall moves from one side to the other side of the particle. Successively, another horizontal vortex is formed on the other side of the particle and the domain wall motion stops. At zero applied field, the two horizontal vortices are equal and the domain wall evenly divides the magnetization into two domains. In a reversed field, the spins rotate coherently until the magnetization is saturated. The X and Y components of the magnetization form one horizontal vortex in a reversed field. Since the spin configurations in the reversal are not symmetric, the net horizontal component of magnetization is not always zero.

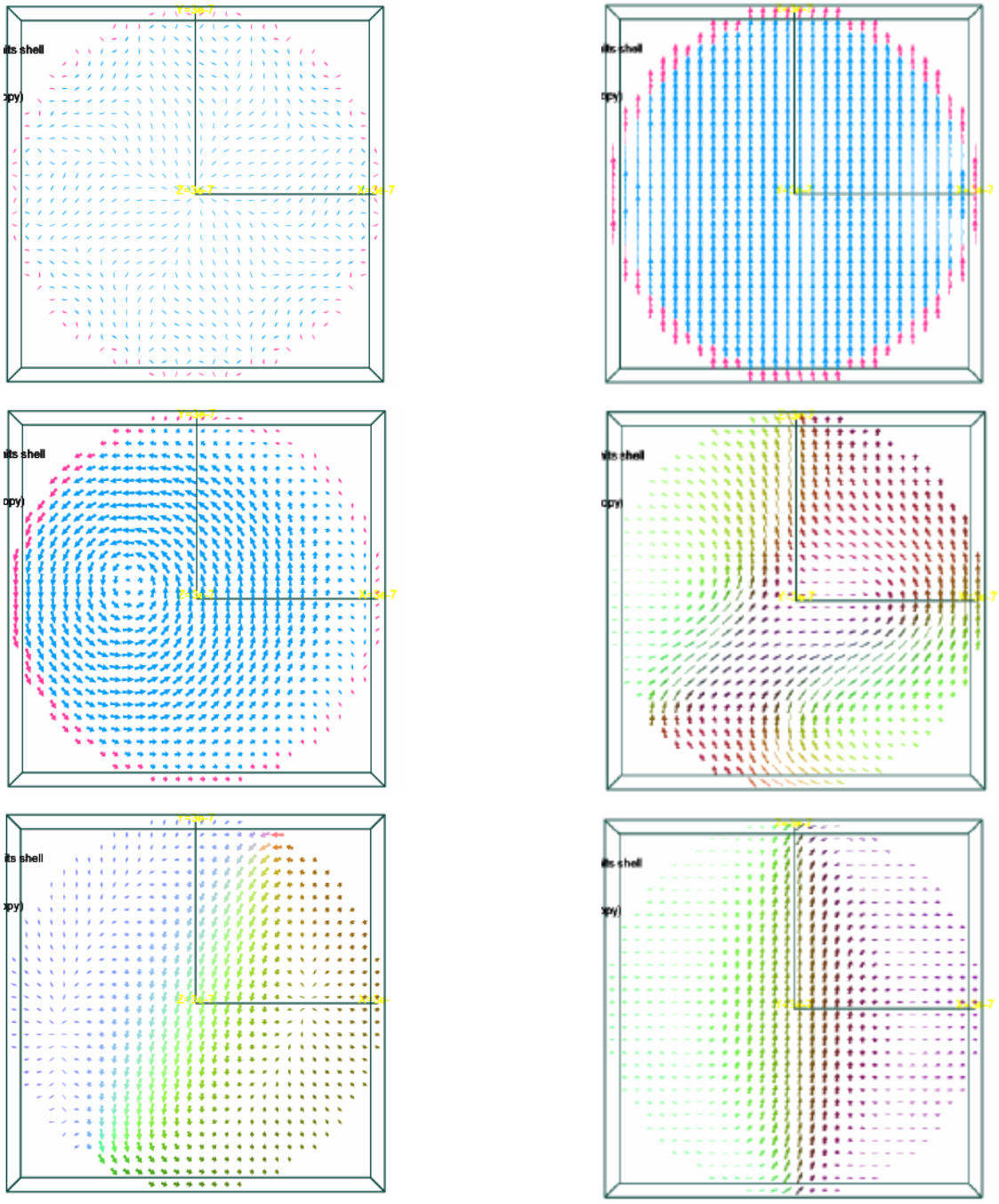

Figure 39. Domain patters of a soft-soft core-shell particle in hysteresis. The particle is a polycrystalline cobalt coated permalloy sphere. Both cobalt and permalloy have no crystalline anisotropy. Left: top view of the z=14 (center) cross-section of the sphere. Right: side view of the y=14 (center) cross-section of the sphere. From top down, the applied field is 350K $A/_M$, 150K $A/_M$ and 0 in +Z direction. When the applied field reverses to –Z direction, the magnetization reverses coherently.

6.5 Conclusions

The remanence of the core-shell structure depends on the thickness of the shell. Precisely, it depends on the volume percentage of the core of hard magnetic material. Two reversal mechanisms exist, depending on whether a Bloch wall is formed or not. Both mechanisms involve the formation of a vertical closure domain. If the shell is not thick enough to form a Bloch wall, anti-parallel alignment in the hard magnetic material creates the vertical closure domain and the center of the closure domain moves towards the Z axis till it reaches the Z axis, where all spins flip. The spins in the soft equator rotates back and forth, depending on the distance to the center of the vertical closure domain. If the shell is thick enough to form a Bloch wall, the vertical closure domain is formed with both hard and soft magnetic materials participating. But, the center of the vertical closure domain is always formed by the spins in the soft magnetic material. The center of the vertical closure domain forms horizontal vortices. It moves towards the Z axis, but it can not penetrate the hard-soft interface. When the center of the vertical closure domain merge near the two poles, all spins of the soft magnetic material flip, followed by the coherent flip of the spins in the hard magnetic material. Transition from the first reversal mechanism to the second mechanism is found. Particles with different shell thickness show different ratio of mixing of the two mechanisms. Characteristics of exchange-spring magnets, such as the angular distribution in soft magnetic material spins normal to the hard-soft interface, rotation and oscillation of the soft magnetic material spins have been observed. But exchange bias, which normally exists in AFM-FM exchange coupled multilayer thin films, has not been observed.

A exchange coupled core-shell particle consisting two soft magnetic materials has

a different reversal mechanism. Without crystalline anisotropy, the spins on the axis need not to align to the axis. Thus, rotational symmetry is broken and local nucleation and multiple domains exist during the reversal. The reversal occurs through local nucleation and domain wall motion at the beginning of the process, followed by coherent rotation.

Chapter 7 Micromagnetics Modeling of Miscellaneous Magnetic Samples

7.1 Domain Pattern of Magnetic Samples with Various Shapes

Micromag, the micromagnetics modeling program, is capable of modeling magnetic samples with arbitrary shape, multiple magnetic materials and various magnetic properties. This chapter briefly reports the modeling attempts of various magnetic samples. All of them are original immature work of this research, unless explicitly stated as reproductions of other authors' published work, or reproductions of well known results, for the verification of the modeling program. For all the results reported in this chapter, modeling with Micromag gives greater insights into the magnetic phenomena. Unless explicitly stated, the standard OOMMF micromagnetics parameters are used as defaults for all materials involved.

7.1.1 Reversal of a narrow cobalt ring

Klaui and Lopez-Diaz *et. al.* fabricated and measured narrow cobalt and permalloy rings.[39] They used OOMMF to model the hysteresis of a narrow cobalt ring with 1200nm outer radius, 900nm inner radius and 15nm thickness. The modeling results and MOKE measurement both reveal the reversal from an onion state to a reversed onion state through domain wall motion in which one domain grows while the other domain contracts. The polycrystalline cobalt is assumed to have no anisotropy. Therefore, K_1 was

set to zero. Other then this, standard OOMMF parameters were used in simulation. The simulation was reproduced in this work with exactly the same set of geometric and magnetic parameters. The experimental hysteresis was conducted on an array of narrow cobalt rings. Our simulation on an individual ring is in remarkable agreement with the experimental results. Figure 40 gives the comparison between experimental hysteresis and the hysteresis modeled with Micromag. Figure 41 gives the remanent and intermediate states in the reversal.

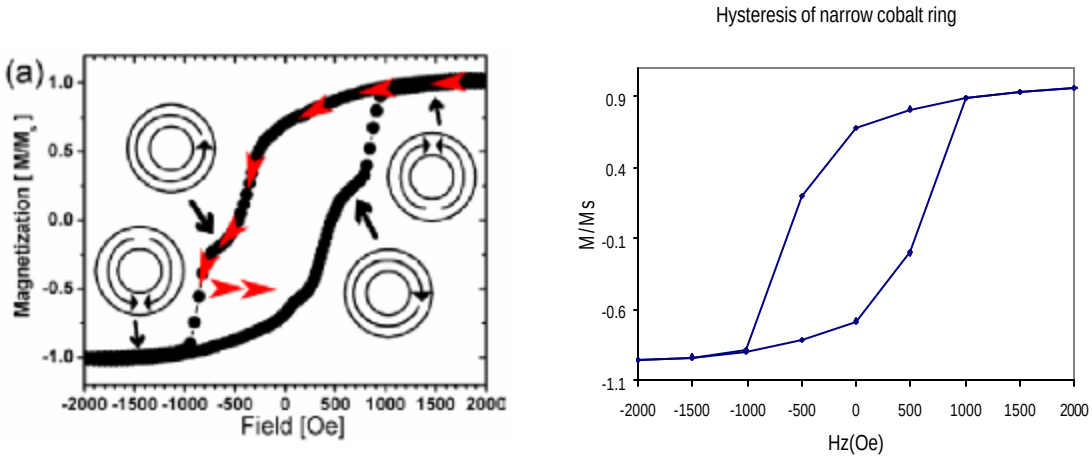

Figure 40. Experimental and simulated hysteresis of a narrow cobalt ring. Left: from ref. 39. Right: this work.

In our simulation, the applied filed scan interval was not small enough. Because of this, the vortex intermediate states were not recorded in the hysteresis loop. But they were observed during the calculation when the small domain was eventually dissipated. The onion state is not shown. It is similar to the remanent state except more spins are aligned to the X axis, the direction to which the applied field is aligned.

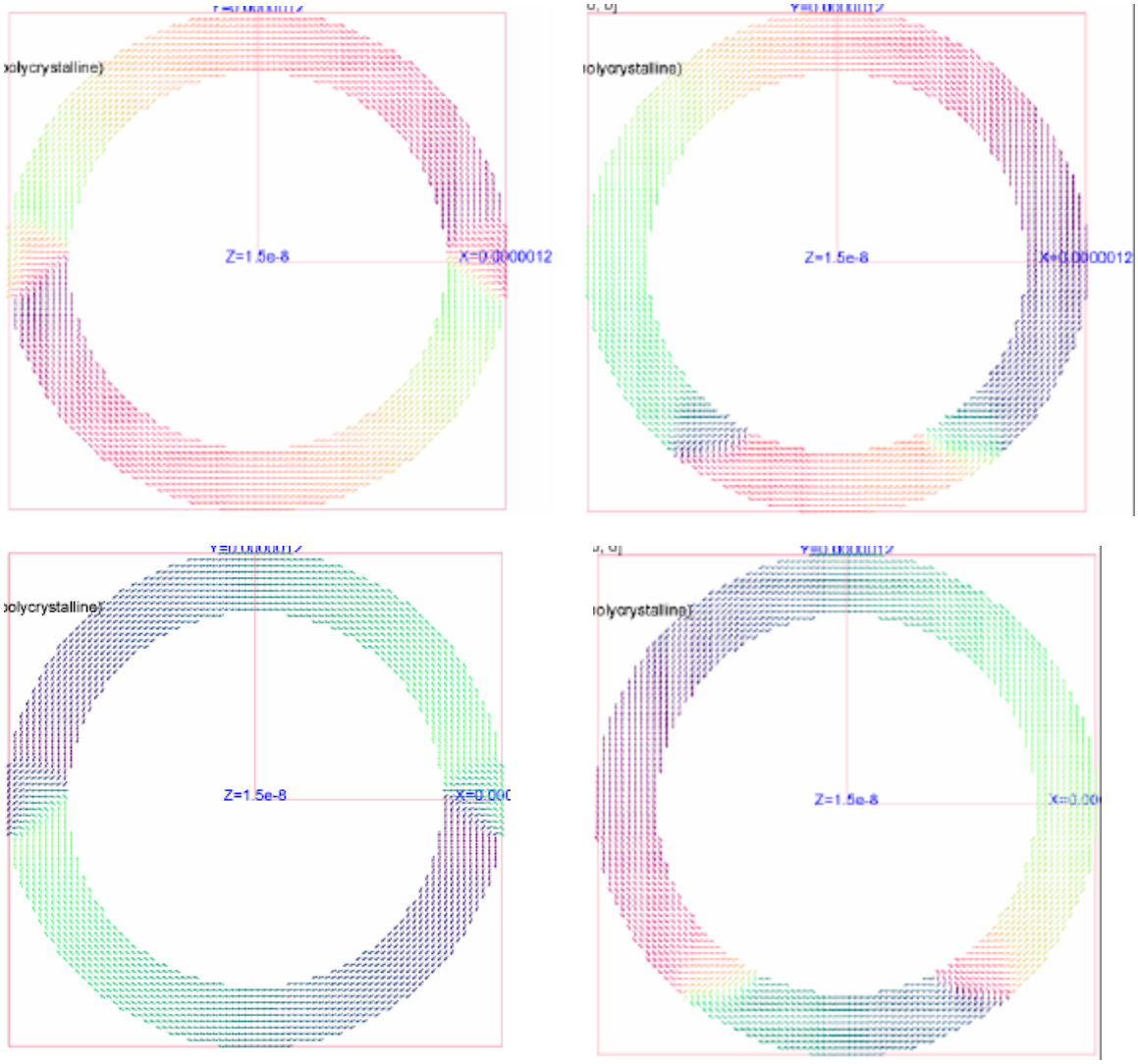

Figure 41. Remanent state and intermediate state of a narrow cobalt ring. The intermediate is at 40K A/M (5KOe) applied field. Upper row corresponds to the backward path in hysteresis and lower row corresponds to the forward path in hysteresis. Both domain walls move down in the reversal process. The backward hysteresis path forms a largely clockwise circle and the forward hysteresis path forms a largely counterclockwise circle. The intermediate state is also found in a permalloy donut (wide ring) with outer radius of 100nm, inner radius of 50nm and thickness of 5nm at zero field, as a resulting spontaneous magnetization configuration from randomly oriented initial spins.

7.1.2 Spontaneous Spin Configuration in Tip Ends

It is well known that a soft magnetic material forms a “C” state in a nano triangular thin film, or a symmetric “Y” state in the case of an equilateral triangular thin

film. For a triangle with a sharp angle, the magnetostatic constraint requires the spins in the sharp end to align to the edges of the sample. The spins in the base may also align to the edges, either in one direction ("C" state) or in two opposite directions ("Y" state). The interior spins show a transition from the vertical alignment in the vertex to the horizontal alignment in the base. Research interest has risen in the phase diagram for the "C" and the "Y" states as a function of the geometric aspect ratio. An isosceles cobalt triangle with 105nm base, 135nm height and 5nm thickness was modeled on a 5nm cubic cell grid. The easy axes of cobalt cells are uniformly in the Y direction. The spontaneous spin configuration starting from randomly oriented spins is found in the "C" state. A three dimensional tip end, or a cone, is modeled. The magnetization in the vertical center cross-section is found in the "Y" state. The permalloy cone has a base diameter of 55nm and 55nm height. It was modeled using a 5nm cubic cell grid. The spontaneous spin configuration starting from randomly oriented spins eventually arranged to form spiral-like stream lines. The spiral-like configuration is common for circular soft magnetic material with magnetization normal to the circular bases. For instance, it was observed in the areas near the two poles in the core-shell particle studied in Chapter 6. The resulting spin configuration of the cone is merely the balance between exchange and magnetostaric forces. Figure 42 illustrates the spontaneous spin configuration of the two tip ends. In the cone, the base cells have the maximum effective field, magnetostatic field, exchange field, magnitude of torque, demag, exchange and total energy.

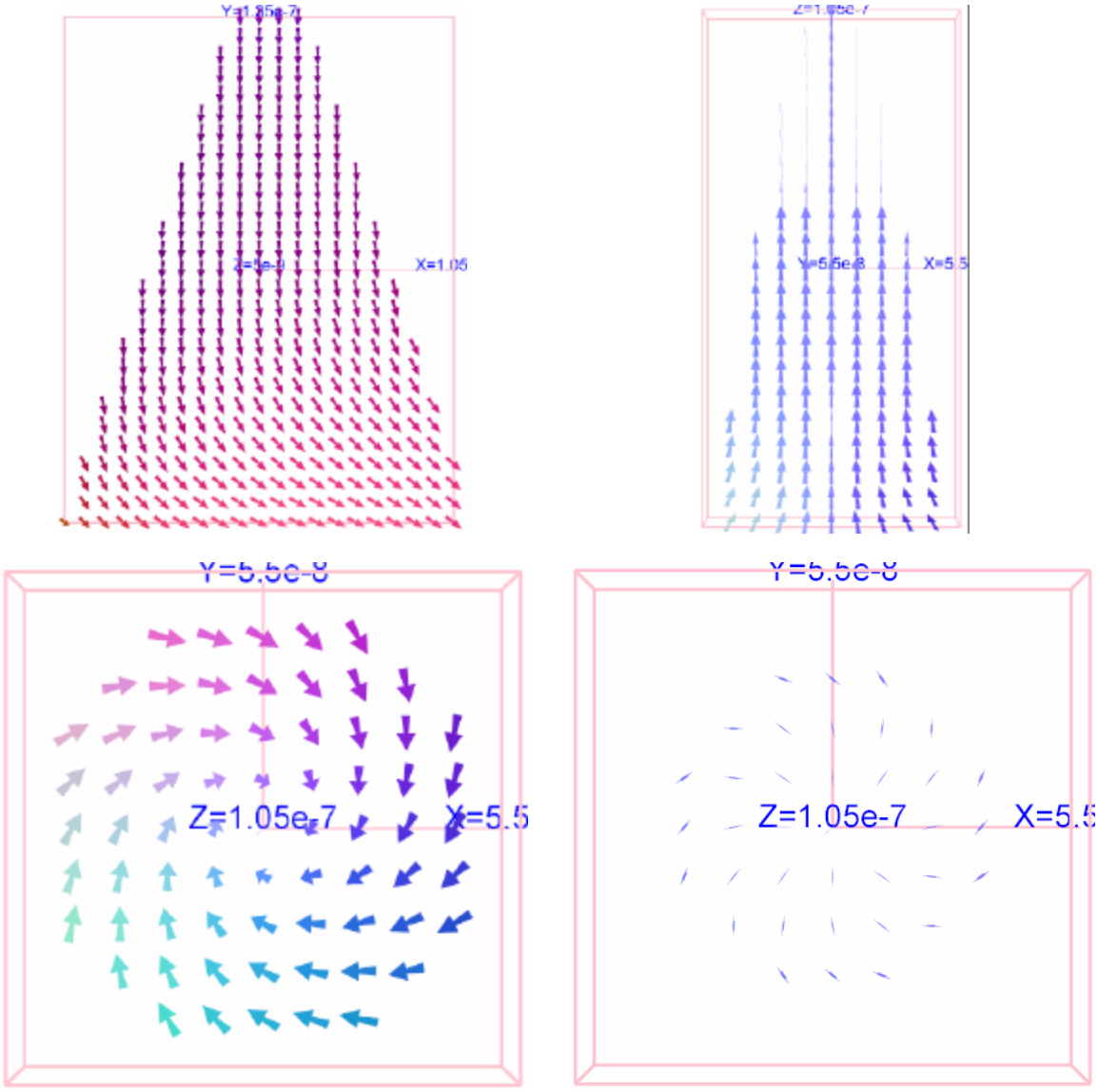

Figure 42. Spontaneous spin configuration in magnetic tip ends. Upper left: "C" state of a isosceles triangle. Upper right: side view of the "Y" state of the cross-section at y=5 of a cone. Lower left: top view of the spiral stream lines in the cross-section at z=0. Lower right: top view of the stream lines in the cross-section at z=5. Spins are aligned in +Z direction in this cross-section.

7.1.3 Hysteresis of a Porous Cobalt Cubic Mesh

In experiments, the magnetic material can coexist with a nonmagnetic material. One form of coexistence is that the nonmagnetic material is surrounded by the magnetic material. Nanoporous ferromagnetic material has been fabricated[57] and its applications in

quantum wires,[58,59] membranes,[60] tunneling junctions are attracting more and more research interests. Common nanoporous ferromagnetic materials are produced by depositing magnetic material into nanoporous substrates such as aluminum thin films and nanotubes, or through chemical reactions. In this modeling work, a cobalt cube with 8 vertexes replaced by non magnetic spheres is studied, in order to investigate the reversal process of a porous magnetic material. The 300nm cube has a $\frac{1}{8}$ spherical vacancy with 100nm radius at each vertex and is modeled on a 10nm cubic cell grid. The easy axis of cobalt cells is in +Z direction, so is the applied field.

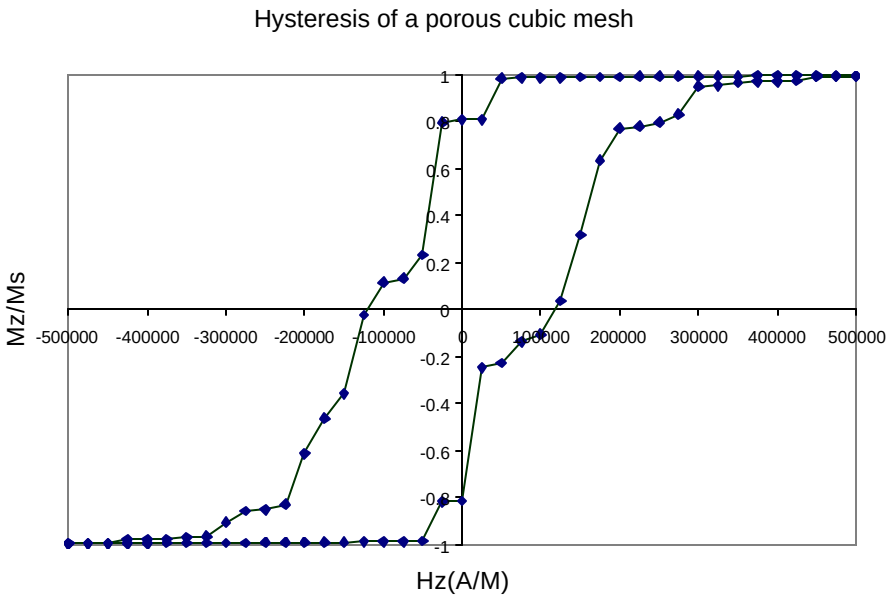

Figure 43. Hysteresis of a porous cobalt cubic mesh.

The magnetization is first saturated in +Z direction, as shown in Figure 44. The remanent state, coercive state and a finish state are also shown in Figure 44. The reversal is a multi-stage process with the spins on spherical surfaces flipping first, followed by the spins in the center. For the interior spins, reversal starts from one side and spreads to the other side through domain wall motion. Spins on the spherical surface have more

flexibility than interior spins in terms of rotation. At the coercive state, spins form a closure domain with greater torque on the surfaces and at the center.

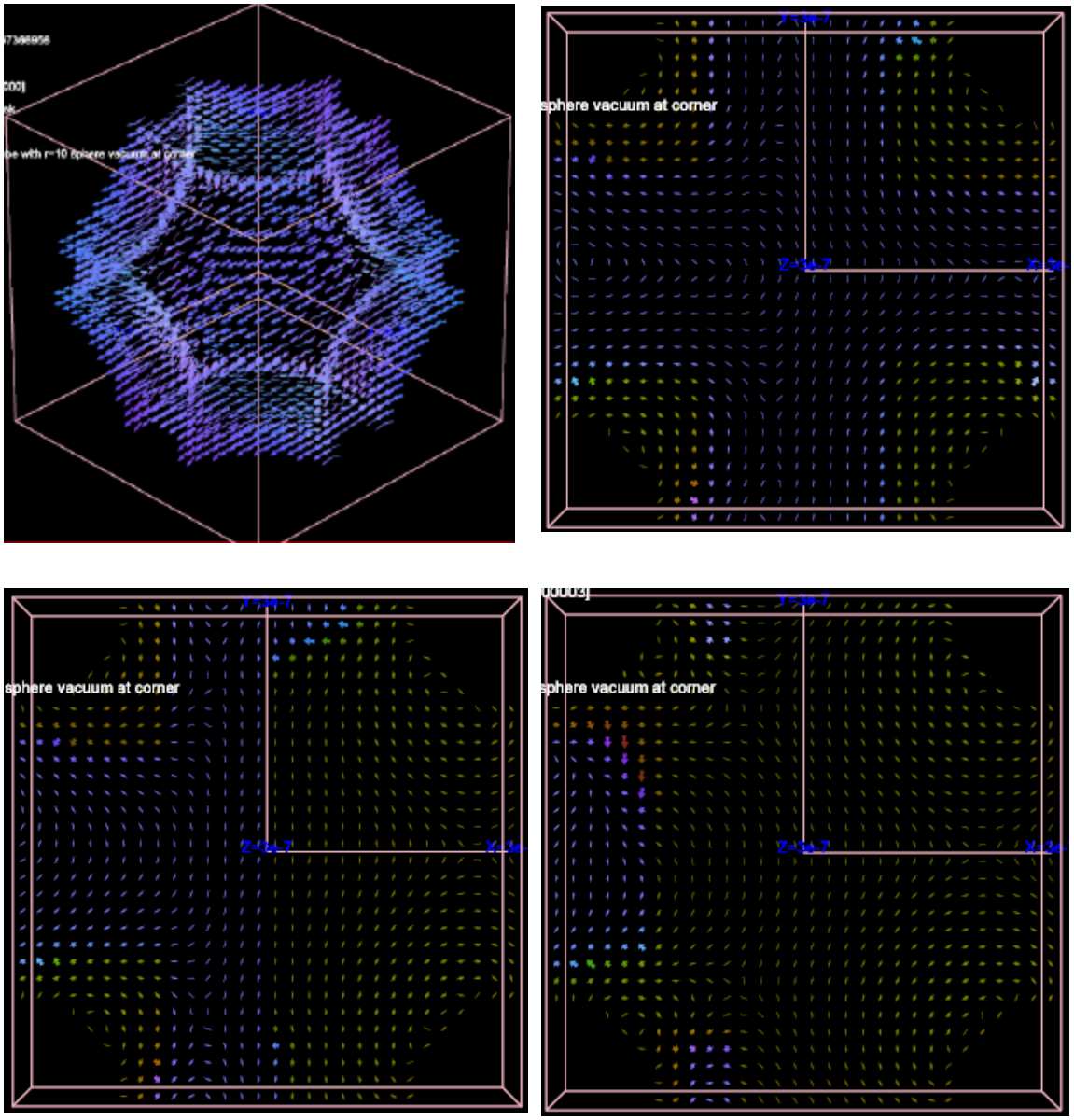

Figure 44. Domain patterns in the reversal of a cubic mesh. Top left: the uniform alignment of the surface spins in the saturated state. Top right: top view of the center z=14 cross section in the remanent state. The spins near the spherical surface are more flexible and less aligned in the vertical direction. Bottom left: the same cross section in the coercive state. The domain wall moved from the center to the left side. The applied field was -125K $^{A}/_{M}$. Bottom right: the same cross section in a finish state. The domain wall moved further left and was about to be dissipated. The applied field was -225K $^{A}/_{M}$.

7.2 Magnetic Coupling between Cobalt and Iron

Iron is a cubic anisotropy material. The standard micromagnetics parameters of iron are listed in Table 10. The second anisotropy constant of iron is used in the modeling. The coupling exchange constant between iron and cobalt is taken as the geometric average of exchange stiffness of cobalt and iron.

Table 10. Micromagnetics parameters of Iron.

Material	$Ms\left(A/M\right)$	$A\left(J/M\right)$	$A_{ij}\left(J/M\right)$	$K_1\left(J/M^3\right)$	$K_2\left(J/M^3\right)$	a
Iron	1.7×10^{6}	2.1×10^{-11}	2.6×10^{-11}	4.8×10^{5}	5.0×10^{4}	0.75

In Figure 45, a cobalt cylinder with 15nm radius and 10nm height is embedded in an iron square with 50nm length and 5nm height. The remanent state, which starts from a higher symmetric state, has lower symmetry (C_s) then its geometric symmetry (C_{4v}). The top picture illustrates a top view of the magnetization configuration and the bottom picture illustrates a side view of the magnetization.

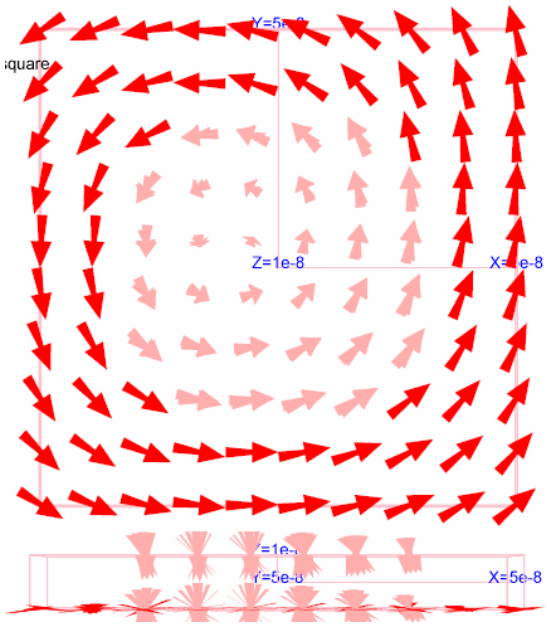

Figure 45. The magnetization of a cobalt cylinder embedded in an iron square. Lost of symmetry in magnetization at zero field is observed. Upper: top view. Lower: side view.

In another modeling work, a coaxial structure has been studied. The coaxial structure is a 40nm radius cobalt cylinder with 25nm height coated by 10nm thick and 25nm high iron. The easy axis of cobalt is in Z direction while the three easy axes of iron coincide with the three cartesian axes. A hysteresis loop with the applied field in the X direction was conducted, starting from a virgin loop. The hysteresis curve is shown in Figure 46. The hysteresis curve resembles the hysteresis curve in the hard axis direction, because the spins in the cubic iron can switch to other directions more easily than in a uniaxial material. Note that the y and z components of magnetization are not zero during the reversal process.

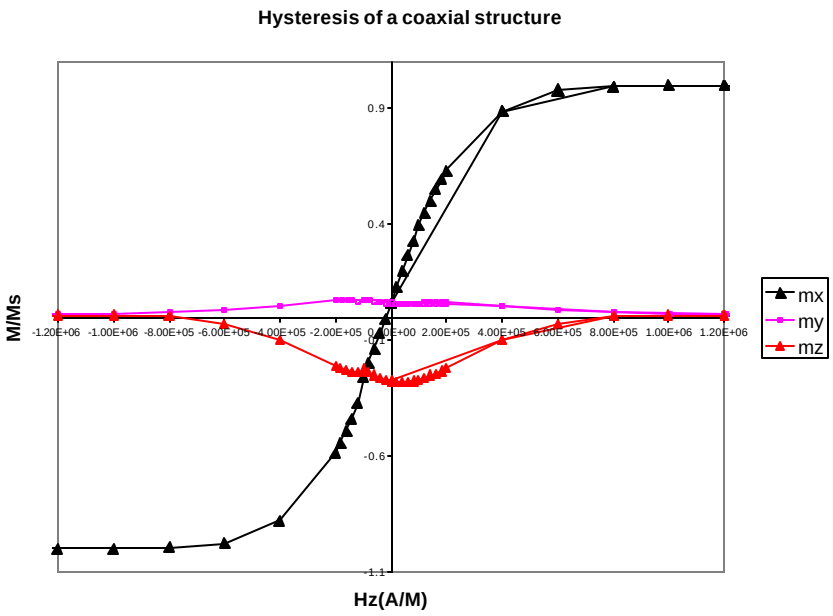

Figure 46. Hysteresis of a coaxial structure. The y and z components of magnetization are not zero, owing to the anisotropy of the materials.

The reversal mechanism is different for the two materials. The spins in the cobalt cylinder reverses through coherent rotation in the X-Z plane. The rotation is not uniform,

i.e. the magnetization gradient in the cylinder is not zero, but no nucleation is found. The center of the cylinder flips first while the edge spins near the material interface are pinned to the vortices in the iron ring and flip later. The spins in the iron ring first align vertically, to make an anti-parallel coupling with the cobalt cylinder. The horizontal components of the iron spins form vortices at the same time. The spins in the iron reverse through rotation of the two "frontlines", similar to the reversal of the spins in the cross-tie modified rings, except no domain wall exists. The spins in the frontlines are just more vertical then other spins in the ring. The two frontlines move like spin waves during the reversal. It is suspected that the reversal mechanism in the iron ring is a result of the exchange coupling between the two materials. Figure 47 shows the side view of the center cross-section of the structure. Figure 48 shows the top view.

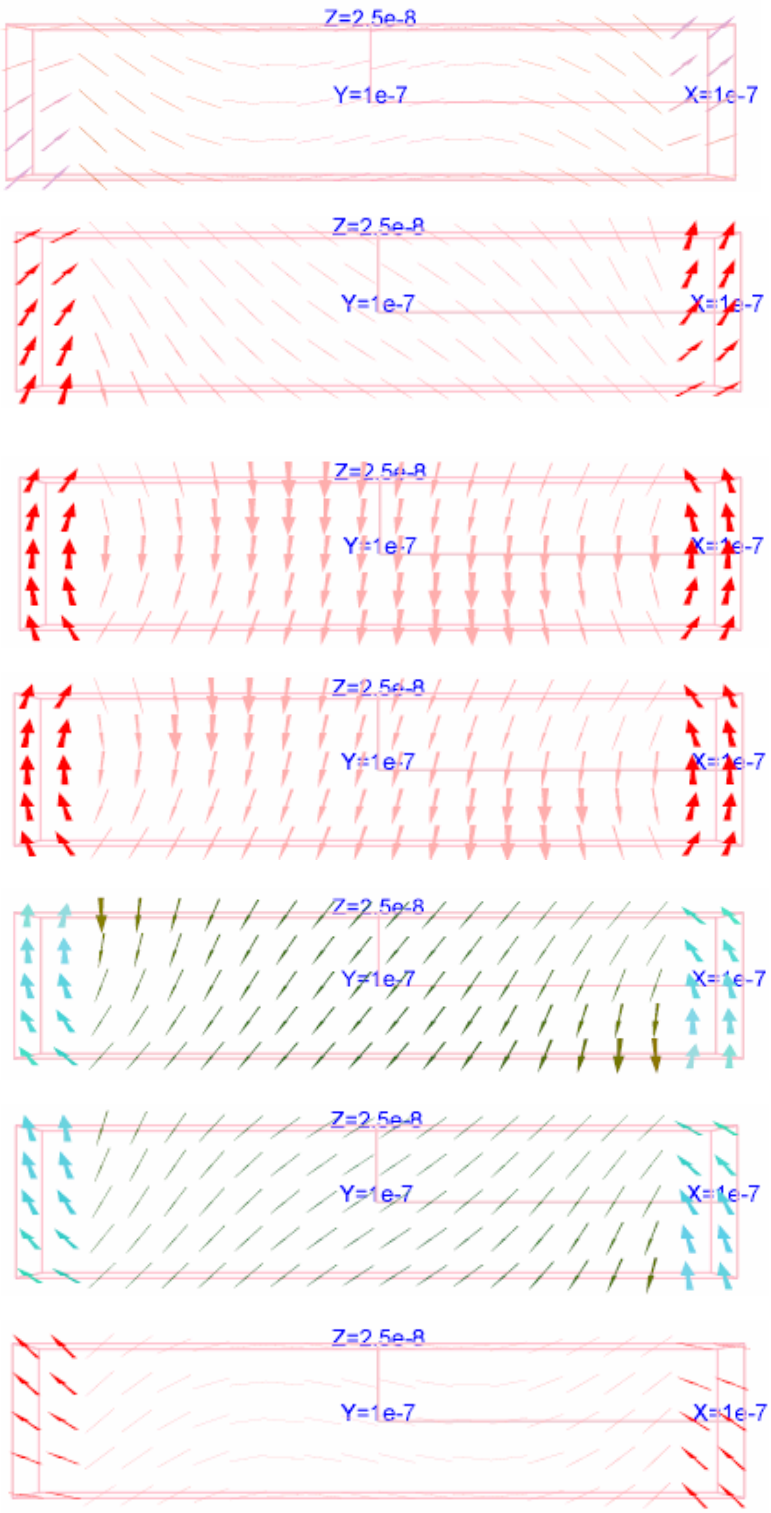

Figure 47. Side view of the domain pattern in the reversal of a coaxial structure.

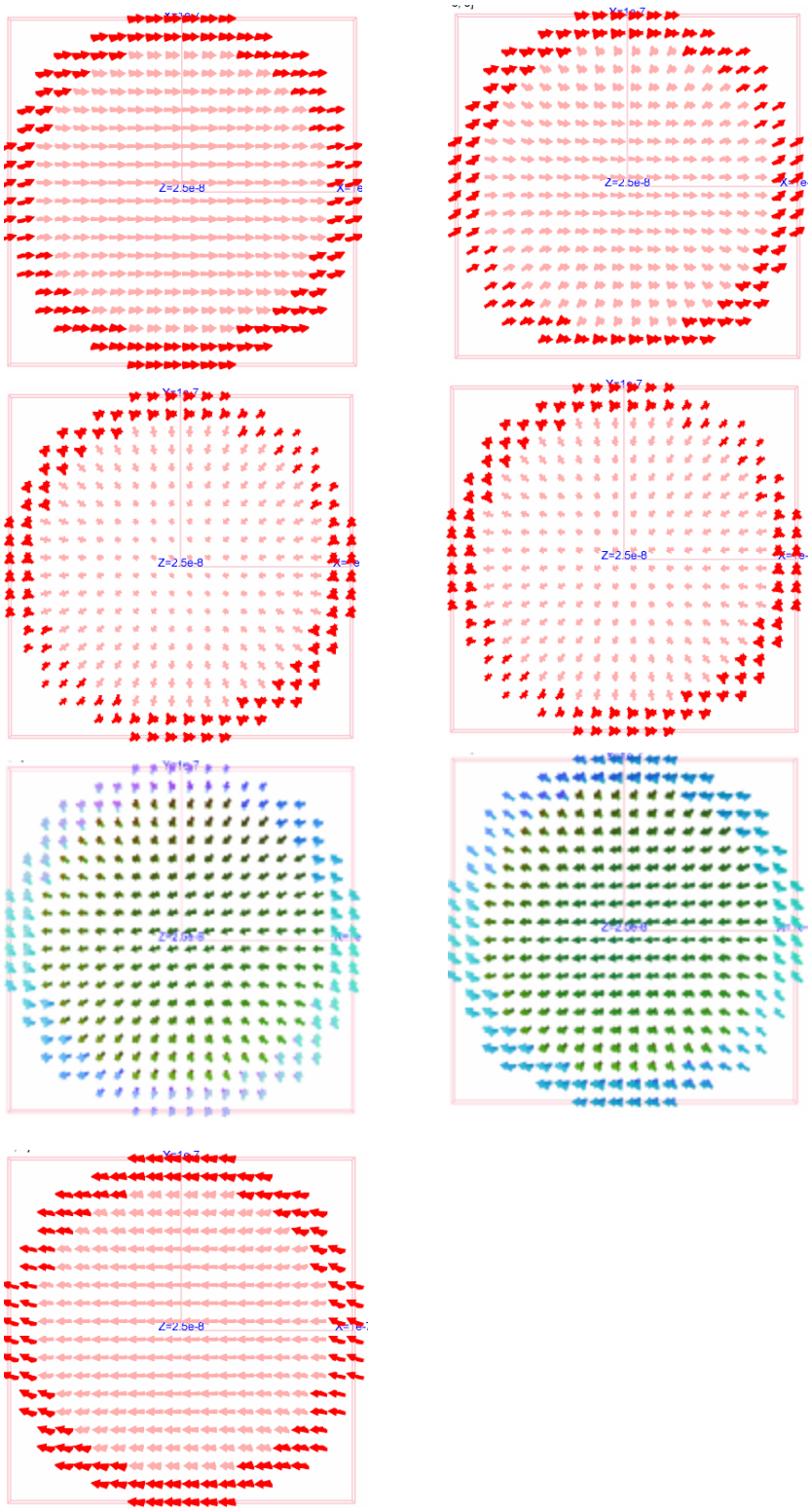

Figure 48. Top view of the domain pattern in the reversal of a coaxial structure. From top down, the applied field is 400K A/M, 200K A/M, 0K A/M, -20K A/M, -100K A/M, -200K A/M and -400K A/M respectively.

7.3 FM-AFM Coupling

Shape effect plays an important role in nano particles because of magnetostatic constraints. But, in an antiferromagnetic material (AFM), the role is dramatically weakened, because no net magnetic charge exists on the material surface. For instance, the spins can align in the vertical direction in a high aspect ratio nano disc, while a ferromagnetic material (FM) in the same configuration always forms in-plane domain patterns.

Figure 49 shows the spontaneous spin configuration of a FM-AFM 100nm square with 5nm thickness. The factitious AFM has the same set of micromagnetics parameters as the ferromagnetic cobalt, other than a negative exchange stiffness coefficient. The AFM material A is put side by side with cobalt. The influence of the AFM slab on the spin configuration in the FM slab is observable only on the exchange interface and the slab edges.

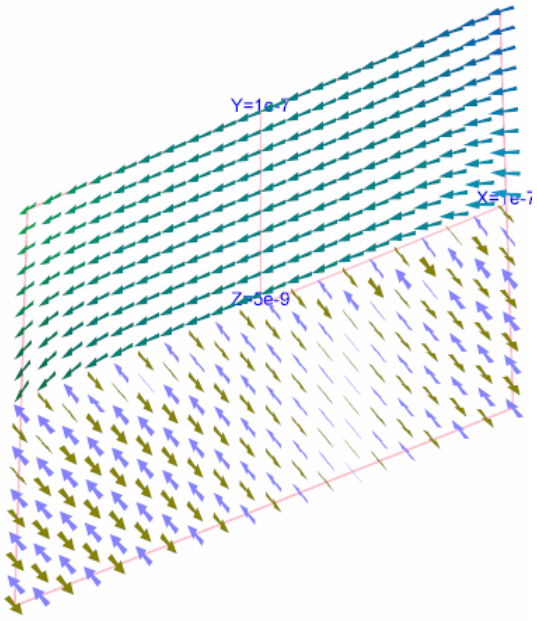

Figure 49. Spontaneous spin configuration of an FM-AFM square.

The hysteresis of two FM-AFM bilayers has been modeled. In the simulation, the FM material is polycrystalline cobalt with zero anisotropy. The AFM material is cobaltous oxide with zero anisotropy. The parameters of CoO are given in Table 11. The exchange coupling between cobalt and cobaltous oxide is antiferromagnetic. The coupling exchange coefficient is set as $-2.1\times10^{-11}\ {}^{J}\!/_{M}$.

Table 11. Micromagnetics parameters of CoO

Material	$Ms\left({}^{A}\!/_{M}\right)$	$A\left({}^{J}\!/_{M}\right)$	$A_{ij}\left({}^{J}\!/_{M}\right)$	$K_1\left({}^{J}\!/_{M^3}\right)$	$K_2\left({}^{J}\!/_{M^3}\right)$	a
CoO	9.8×10^{5}	-2.1×10^{-11}	-2.1×10^{-11}	0	0	0.75

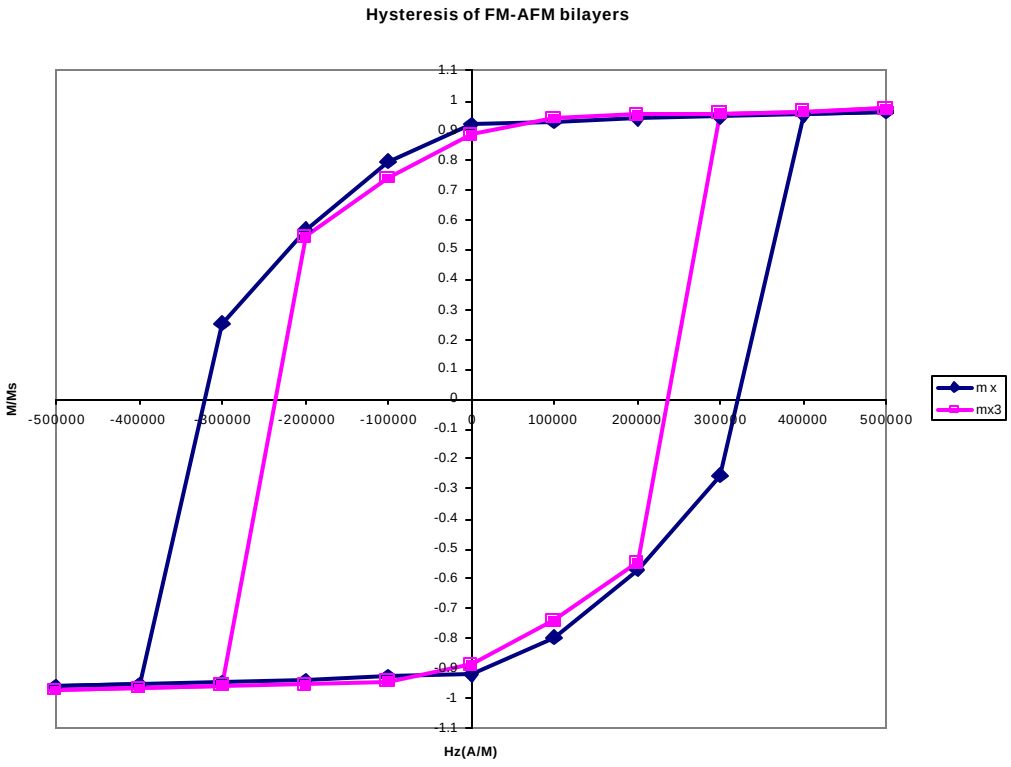

Figure 50. Hysteresis of FM-AFM bilayers. mx is the normalized magnetization for a 10nm thick square and mx3 is the normalized magnetization for a 30nm thick square.

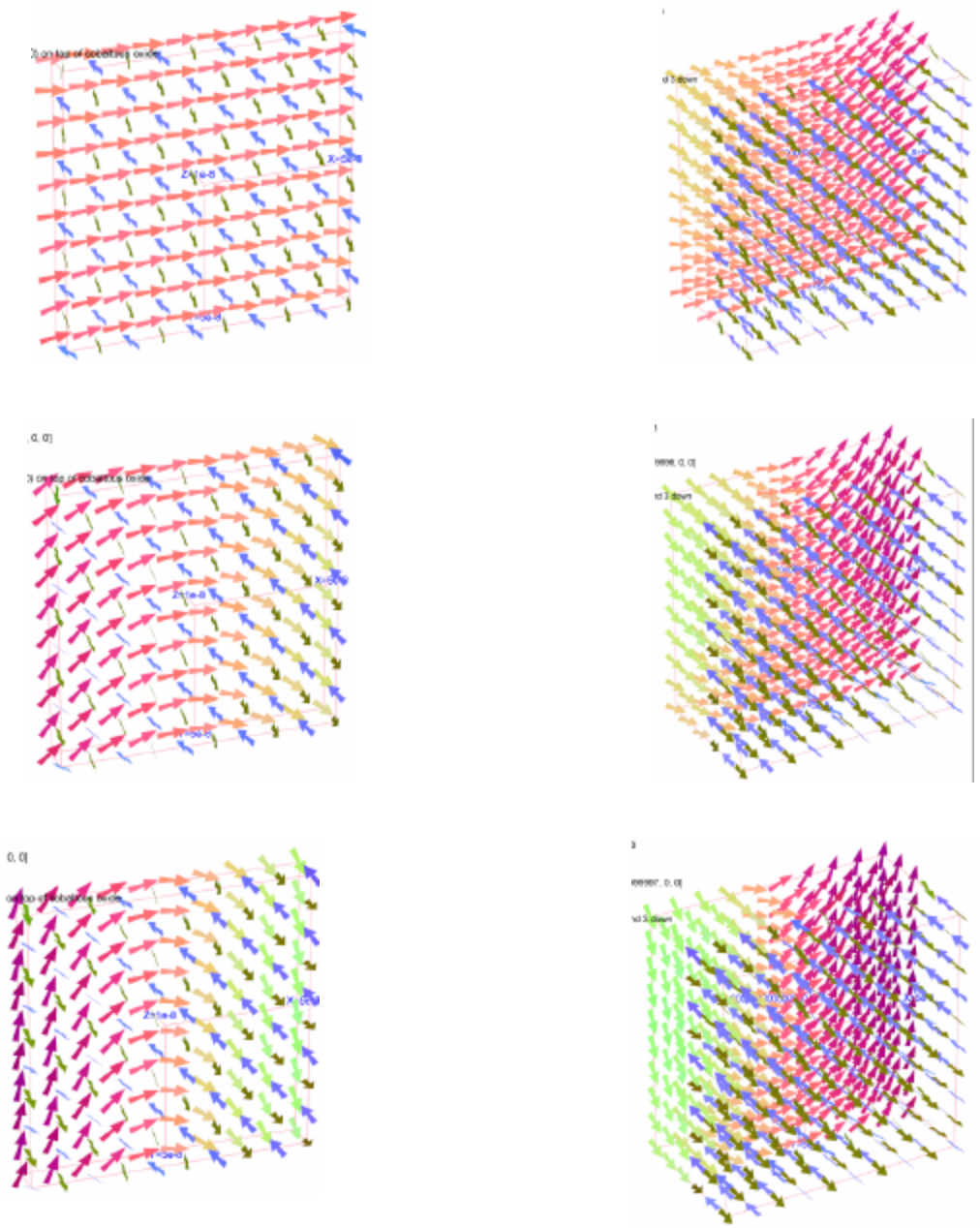

Figure 51. Spin configuration in the reversal of FM-AFM bilayers. From top down, the applied field is 0 , -100K $A/_M$ and -200K $A/_M$ respectively.

7.4 Discussion

The investigations presented in this chapter are not complete. Therefore, no

meaningful conclusion was reached. However, some work, such as the coupling between cobalt and iron and the coupling between cobalt and cobaltous oxide, are of practical interest. More modeling work on such topics needs to be performed in the future with the powerful micromagnetics simulation tool -- Micromag. The investigation provides a guide for further in-depth study on such topics.

Conclusions

A web based micromagnetics modeling program, Micromag, has been created. This program is capable of modeling multiple magnetic materials with arbitrary shape and has been used to model a variety of magnetic materials. The analyzing and visualization tools provide insight into the magnetization reversal details.

The results of the simulation recommended two candidates for the Magnetic Random Access Memory application. By modifying a nano permalloy ring with a narrow cross-tie structure, the changes in the in-plane magnetization reversal with the applied field diagonal to the cross-tie structure suggests this device will better meet MRAM requirements. The two desired onion states were stabilized by the introduced configurational anisotropy. The switching field distribution was drastically reduced and the hysteresis squareness was greatly increased. While the PM I element did not meet MRAM application requirements, the PM II element with a greater aspect ratio was suitable for MRAM. The reversal process of the PM I element has two stages, the formation and motion of domain walls and the formation and dissipation of a vortex center. The reversal process of the PM II element lacks the second "problem-making" stage due to geometry constraints and leads to a squarer hysteresis curve. The simulation result is in agreement with experiments and simulation results by other authors.

Study on the thickness dependence of the magnetization reversal of a series of core-shell particles revealed two different reversal mechanisms depending on whether a

Bloch wall was able to form in the soft magnetic material layer. The center of the Bloch wall existed only in the soft magnetic material layer and the spins in the center aligned perpendicular to the applied field to form vortices. At the remanent state, the surface spins of a thin shell particle align in the opposite direction to the applied field. The characteristics of exchange spring magnets, which are normally observed in magnetic thin films, were found in the exchange spring core-shell magnet.

The modeling program has been successfully used to simulate the domain patterns and reversal processes of other magnetic elements, such as narrow permalloy rings, cone, soft nanoporous magnetic material, FM-FM core-shell particle and FM-AFM bilayers. The simulation results were compared with available experimental results and simulation results and agreement was found. This technique provides in-depth insight into the magnetization reversal phenomena.

References

1 E. C. Stoner, *Proc. R. Soc. A*, **165**, 372 (1965)

2 F. Bethe and G. Gentile, *Ann. Phys., Lpz.* **3**, 133 (1929)

3 F. Bloch and G. Z. Gentile, *Phys.* **70**, 395 (1931)

4 R. Skomski and J. M. D. Coey, *Phys. Rev. B*, **48**, 15812 (1993)

5 R. L. Comstock, *Introduction to Magnetism and Magnetic Recording*, New York: Wiley (1999)

6 D. J. Sellmyer, C. P. Luo, Y. Qiang and J. P. Liu, *Handbook of Thin Film Materials. Nanomaterials and magnetic thin films.* **Vol.5,** p337

7 J. Yu, U. Rudiger, A. D. Kent, L. Thomas and S. S. P. Parkin, *J. Appl. Phys.* **85**, 5501 (1999)

8 Y. Millev, R. Skomski and J. Kirschner, *Phys. Rev. B*, **58**, 6305 (1998)

9 S. Bulgel, *Phys. Rev. B*, **51**, 2025 (1995)

10 E. E. Fullerton, S. J. Jiang and S. D. Bader, *J. Magn. Magn. Mater.* **200**, 392 (1999)

11 H. Zeng, M. Zheng, R. Skomski, D. J. Sellmyer, Y. Liu, L. Menon and S. Bandyopadhyay, *J. Appl. Phys.* **87**, 4718 (2000)

12 M. Zheng, R. Skomski, Y. Liu and D. J. Sellmyer, *J. Phys. Condens. Matter* **12** L497 (2000)

13 R. Skomski, H-P Oepen and J. Kirschner, *Phy. Rev. B*, **58**, 3223 (1998)

14 C. A. Ross, R. Chantrell, M. Hwang, M. Farhoud, T. A. Savas, Y. Hao, H. I. Smith, F. M. Ross, M. Redjdal and F. B. Humphrey, *Phys. Rev. B*, **62**, 14252 (2000)

15 E. C. Stoner and E. P. Wohlfarth, *Philos. Trans. London* **Ser. A 240**, 599 (1948), reprinted in *IEEE Trans. Magn.* **MAG-27**, 3475 (1991).

16 C. Jiang, M. Venkatesan, K. Gallagher and J. M. D. Coey, *J. Magn. Magn. Mater.* **236**, 49 (2001)

17 Z. Chen, X. Meng-Burany, H. Okumura and G. C. Hadjipanayis, *J. Appl. Phys.* **87**, 3409 (2000)

18 G. Vertesy, M. Pardavi-Horvath, L. Tomas and L. Pust, *J. Appl. Phys.* **63,** 1694 (1988)

19 V. Novosad, M. Grimsditch, J. Darrouzet, J. Pearson, S. D. Bader, V. Metlushko, K. Guslienko, Y. Otani, H. Shima and K. Fukamichi, *Appl. Phys. Lett*, **82**, 3716 (2003)

20 M. J. Donahue, G. Vertesy and M. Pardavi-Horvath, *J. Appl. Phys.* **93**, 7308 (2003)

21 J. Shi, *IEEE Trans. Magn.* **34**, 997 (1998)

22 Y. Zheng and J-G Zhu, *J. Appl. Phys.* **81**, 5471 (1997)

23 F. J. Castaño, C. A. Ross and A. Eilez, *J. Phys. D.: Appl. Phys.* **36**, 2031 (2003)

24 Elmer F. J., *Phys. Rev. B*, **53**, 14323 (1996)

25 P. Vavassori, M. Grimsdith, V. Novosad, V. Metlushko and B. Ilic, *J. Appl. Phys.* **93**, 7900 (2003)

26 D. K. Koltsov and M. E. Welland, *J. Appl. Phys.* **94**, 3457 (2003)

27 F. J. Castaño, C. A. Ross, C. Frandsen, A. Eilez, D. Gil, H. I. Smith, M. Redjdal and F. B. Humphrey, *Phys. Rev. B*, **67**, 184425 (2003)

28 J. Lee, K. Oh, H-J Kim, and K. Kim, "Magnetization reversal process of the nanosized elliptical permalloy magnetic dots with various aspect ratios", *J. Magn. Magn. Matt*. In press. (2004), preprint at http://engineering.snu.ac.kr/pdf

29 H. Barkhausen, *Z. Phys.* **20**, 401 (1919)

30 R. Skomski and J. M. D. Coey, *Permanent Magnetism* (Bristol: Institute of Physics Publishing), (1999)

31 M. A. Ruderman and C. Kittel, *Phys. Rev*., **96**, 99 (1954)

32 P. Bruno and C. Chappert, *Phys. Rev. B,* **46**, 261 (1992).

33 L. Greengard and V. Rokhlin, *J. Comp. Phys.* **73**, 325(1987).

34 P. B. Visscher and D. M. Apalkov, "Simple recursive Cartesian implementation of fast multipole algorithm", preprint at http://bama.ua.edu/~visscher/mumag/cart.pdf.

35 A. J. Newell, W. Williams, and D. J. Dunlop, *J. of Geo. Res.* **98**, 9551 (1993)

36 J-G Zhu, Y. Zheng and G. Prinz**,** *J.Appl. Phys.* **87(9),** 6668 (2000)

37 M. Schneider, H. Hoffmann, S. Otto, Th. Haug And J. Zweck, *J. Appl. Phys.* **92**, 1466 (2002)

38 M. Steiner and J. Nitta *Appl. Phys. Lett*., **84(6)**, 939 (2004)

39 M. Klaui, C. A. F. Vaz, L. Lopez-Diaz and J. A. C. Bland, *J. Phys. Cond. Matt*. **15,** 985 (2003)

40 H. Park, Y. K. Hong, S. H. Gee and D. W. Erickson, "Magnetic Element Shape for Magnetic Random Access Memory (MRAM)". 11th Ann. NASA Symp .on VLSI design, (2003), at http://www.cambr.uidaho.edu/symposiums/symp11/YangKiHongPaper.pdf

41 M. Klaui, C. A. F. Vaz, J. A. C. Bland, E. H. C. P. Sinnecker and A. P. Guimarães, W. Wernsdorfer, G. Faini, E. Cambril, L. J. Heyderman and C. David, *Appl. Phys. Lett*. **84(6)**, 951 (2004)

42 S. Tehrani, B. Engel, J. Slaughter, E. Chen, M. DeHerrera, M. Durlam, P. Naji, R. Whig, J. Janesky and J. Calder, *IEEE Trans Magn*. **36**, 2752 (2000)

43 L. Lopez-Diaz, J. Rothman, M. Klaui and J. A. C. Bland, *IEEE Trans Magn*. **36**, 3155 (2000)

44 N. Dao, "Micromagnetics of nanoshaped and multilayer magnetic elements", Ph.D. dissertation, University of New Orleans, (2002)

45 S. Homer, "Depth and shape dependent micromagnetics effects of geometry and configuration on switching properties". Ph.D. dissertation, University of New Orleans (2002)

46 H. Park, Y. K. Hong, S. H. Gee, D. W. Erickson and B. C. Choi, *Appl. Phys. Lett.* **83,** 329 (2003)

47 E. F. Kneller and R. Hawig, *IEEE Trans. Magn***. 27**, 3588 (1991)

48 E. Goto, N. Hayashi, T. Miyashita and K. Nakagawa, *J. Appl. Phys.* **36**, 2951 (1965)

49 E. E. Fullerton, J. S. Jiang, M. Grimsditch, C. H. Sowers and S. D. Bader, *Phys. Rev. B. Cond. Matt,*. **58**, 12193 (1998)

50 T. Leineweber and H. Kronmuller, *J. Magn. Magn. Mat.* **176,** 145 (1997)

51 S. Yan, J. A. Barnard, F. Xu, J. L. Weston and G. Zangari, *Phys. Rev. B. Cond. Matt.* **64,** 184403 (2001)

52 J. Samuel, J. Hans, G. Kaper and G. K. Leaf, *Disc. Cont. Dyna. Sys. B.* 1, 219 (2001)

53 L. Zhao, K. Liu, C. R. Pike, J. Davies, R. T. Scalettar, G. T. Zimanyi, K. L. Verosub and M. W. McElfresh, "First Order Reversal Curve (FORC) - A graphical tool to study the irreversible field in spring magnets", to be appear in *J. Magn. Magn. Mat.* at http://lifshitz.ucdavis.edu/~lzhao/papers/spring_magnet_Oct0503.pdf

54 G. Gubbiotti, G. Carlotti, M. Adami, J. Weston, P. Vavassori and G. Zangari, IEEE Trans. Magn., 38(5), 2779 (2002).

55 E. L. Salaba, M. Spasova and M. Farle, "Self-assembly and Magnetism in Novel Core-shell Microspheres" at http://www.iho.tu-bs.de/413.pdf

56 J. M. G. Coey and K. O'Donnell, *J. Appl. Phys.* **81**, 4810 (1997)

57 Cientifica Ltd. "Nanoporous materials technology whit paper" at http://www.cientifica.com/html/Whitepapers/wpfiles/nanoporous_materials_WP.pdf

58 Lee K. H., Jeung W. Y. and Lee W. Y. *J. Appl. Phys.* **91**, 8513 (2002)

59 T. G. Sorop, C. Untiedt, F. Luis, M. Kroll, M. Ra and L. J. de Jongh, *Phys. Rev. B* **67**, 014402 (2003)

60 T. G. Sorop, C. Untiedt, F. Luis, and L. J. de Jongh, *J. Appl. Phys.* **93**, 7044 (2003)

Appendix A Thermal Fluctuation Strength

The thermal fluctuation is assumed to be Gaussian white noise. The thermal fluctuation field H_t is characterized by the expectation values of its first and second moments.

The average taken over time is zero

$$\left\langle H_{t,i}(t)\right\rangle = 0 \tag{1}$$

and the variance is proportional to a diffusion coefficient

$$\left\langle H_{t,i}(t)\, H_{t,j}(t')\right\rangle = 2D\delta_{ij}\delta(t-t') \tag{2}$$

In Eq. 2, D is the diffusion coefficient, i and j denotes the Cartesian coordinates, δ_{ij} is the Kronecker symbol and $\delta(t-t')$ is the Dirac delta. Eq. 2 means that the thermal field is irrelevant in coordinates and not correlated in time. The later assumption is based on the fact that thermal fluctuation is much faster than the motion of magnetization.

Including thermal fluctuation in the Landau-Lifshitz-Gilbert equation leads to a stochastic LLG equation:

$$\frac{dM}{dt} = -\gamma M \times (H + H_t) - \frac{\alpha\gamma}{M_s} M \times \left[M \times (H + H_t)\right] \tag{3}$$

Eq. 3 can be split into the deterministic part and the stochastic part:

$$\frac{dM}{dt} = -g M \times (H) - \frac{ag}{M_s} M \times (M \times H) \\ -g M \times (H_t) - \frac{ag}{M_s} M \times (M \times H_t) \tag{4}$$

We define the i component of the deterministic part as

$A_i(M,t) = \left[-g M \times H - \frac{ag}{M_s} M \times M \times H \right]_i$, where A is a function of magnetization, which in turn is a function of time.

Using the Levi-Civita notation of cross product of two vectors $\vec{a} \times \vec{b} = e_{ijk} a_j b_k$ with the Einstein summation convention, the i component of the stochastic part can be simplified.

$$[M \times H_t]_i = e_{ijk} M_j H_{t,k}$$

and

$$\begin{aligned} M \times M \times H_t &= e_{ijn} M_j \left(e_{nmk} M_m H_{t,k} \right) \\ &= \left(e_{ijn} e_{nmk} M_j M_m \right) H_{t,k} \\ &= \left[\left(d_{im} d_{jk} - d_{ik} d_{jm} \right) M_j M_m \right] H_{t,k} \\ &= \left[M_i M_k - d_{ik} M_j M_j \right] H_{t,k} \\ &= \left[M_i M_k - d_{ik} |M|^2 \right] H_{t,k} \end{aligned} \tag{5}$$

in Eq. 5 $e_{ijk} e_{klm} = d_{il} d_{jm} - d_{im} d_{jl}$ is used and $M_j M_j = M_x^2 + M_y^2 + M_z^2 = |M|^2$.

The i component of the stochastic part can be simplified by defining:

$$B_{ik}(M,t) = -g e_{ijk} M_j - \frac{ag}{M_s} \left(M_i M_k - d_{ij} |M|^2 \right) \tag{6}$$

Thus

$$\frac{dM_i}{dt} = A_i(M,t) + B_{ik}(M,t) H_{t,k} \tag{7}$$

Eq. 7 is a Langevin equation where the multiplicative factor $B_{ik}(M,t)$ for the stochastic process $H_{t,k}(t)$ is a function of M.

The time evolution of the non-equilibrium probability distribution $P(M,t)$ of a Langevin system represented by Eq. 7 is given by the Fokker-Planck equation in the following form:

$$\frac{\partial P}{\partial t} = -\frac{\partial}{\partial M_i}\left[\left(A_i + DB_{jk}\frac{\partial B_{ik}}{\partial M_j}\right)P\right] + \frac{\partial^2}{\partial M_i \partial M_j}\left[\left(DB_{ik}B_{jk}\right)P\right] \quad (8)$$

The derivative of Eq. 6 is given by:

$$\begin{aligned}\frac{\partial B_{ik}}{\partial M_j} &= \frac{\partial}{\partial M_j}\left[-ge_{ijk}M_j - \frac{ag}{M_s}\left(M_i M_k - d_{ik}|M|^2\right)\right] \\ &= -ge_{ijk} - \frac{ag}{M_s}\left[\left(M_i d_{jk} + M_k d_{ij} - 2d_{ik}M_j\right)\right]\end{aligned} \quad (9)$$

thus

$$\begin{aligned}B_{jk}\frac{\partial B_{ik}}{\partial M_j} &= B_{jk}\left\{-ge_{ijk} - \frac{ag}{M_s}\left[\left(M_i d_{jk} + M_k d_{ij} - 2d_{ik}M_j\right)\right]\right\} \\ &= g^2\left\{e_{ijk}M_i + \frac{a}{M_s}\left(M_j M_k - d_{jk}|M|^2\right)\right\}\left\{e_{ijk} + \frac{a}{M_s}\left[\left(M_i d_{jk} + M_k d_{ij} - 2d_{ik}M_j\right)\right]\right\} \\ &= g^2\left\{\begin{array}{l} e_{ijk}e_{ijk}M_i + \frac{a}{M_s}\left(e_{ijk}d_{jk}|M|^2 + e_{ijk}M_j M_k - 2e_{ijk}M_j M_k + e_{ijk}M_j M_k - e_{ijk}d_{jk}|M|^2\right) \\ +\left(\frac{a}{M_s}\right)^2\left(M_i|M|^2 - d_{jk}d_{jk}M_i|M|^2 + M_i|M|^2 - M_i|M|^2 - 2M_i|M|^2 + 2M_i|M|^2\right)\end{array}\right\} \\ &= g^2\left\{0\cdot M_i + \frac{a}{M_s}\cdot 0 + \left(\frac{a}{M_s}\right)^2\cdot 0\right\} \\ &= 0\end{aligned}$$

In the above equation $d_{jk}d_{jk} = d_{jj} = 1$ and $e_{ijk}e_{ijk} = d_{jj}d_{kk} - d_{jk}d_{jk} = 1 - 1 = 0$.

$$B_{ik}B_{jk} = g^2\left\{e_{ikl}M_l + \frac{a}{M_s}\left(M_iM_k - d_{ik}\left|M\right|^2\right)\right\}\left\{e_{jkm}M_m + \frac{a}{M_s}\left(M_jM_k - d_{jk}\left|M\right|^2\right)\right\}$$

$$= g^2\left\{\begin{array}{l} e_{ikl}e_{jkm}M_lM_m \\ +\frac{a}{M_s}\left(e_{ikl}M_lM_jM_k - e_{ijl}M_l\left|M\right|^2 + e_{jkm}M_mM_iM_k - e_{jim}M_m\left|M\right|^2\right) \\ +\left(\frac{a}{M_s}\right)^2\left(M_iM_j\left|M\right|^2 - M_iM_j\left|M\right|^2 - M_jM_i\left|M\right|^2 + d_{ij}\left|M\right|^4\right)\end{array}\right\}$$

$$= g^2\left\{\begin{array}{l} \left(d_{ij}d_{lm} - d_{im}d_{lj}\right)M_lM_m \\ +\frac{a}{M_s}\left(e_{ikj}M_jM_jM_k - e_{ijk}M_k\left|M\right|^2 + e_{jki}M_iM_iM_k - e_{jik}M_k\left|M\right|^2\right) \\ +\left(\frac{a}{M_s}\right)^2\left(M_iM_j\left|M\right|^2 - M_iM_j\left|M\right|^2 - M_jM_i\left|M\right|^2 + d_{ij}\left|M\right|^4\right)\end{array}\right\}$$

$$= g^2\left\{\begin{array}{l} \left(d_{ij}d_{lm} - d_{im}d_{lj}\right)M_lM_m \\ +\left(\frac{a}{M_s}\right)^2\left(M_iM_j\left|M\right|^2 - M_iM_k\left|M\right|^2 - M_jM_i\left|M\right|^2 + d_{ij}\left|M\right|^4\right)\end{array}\right\}$$

$$= g^2\left\{\left(d_{ij}\left|M\right|^2 - M_iM_j\right) + \left(\frac{a}{M_s}\right)^2\left|M\right|^2\left(d_{ij}\left|M\right|^2 - M_iM_j\right)\right\}$$

$$= g^2\left(1 + a^2\right)\left(d_{ij}\left|M\right|^2 - M_iM_j\right)$$

The Fokker-Planck equation Eq. 8 can be rewritten as:

$$\frac{\partial P}{\partial t} = -\frac{\partial}{\partial M_i}[A_i P] + Dg^2\left(1+a^2\right)\frac{\partial^2}{\partial M_i \partial M_j}\left[\left(d_{ij}\left|M\right|^2 - M_i M_j\right)P\right]$$

$$= -\frac{\partial}{\partial M_i}\left[A_i P + Dg^2\left(1+a^2\right)\frac{\partial}{\partial M_j}\left(d_{ij}\left|M\right|^2 - M_i M_j\right)P\right]$$

$$= -\frac{\partial}{\partial M_i}\left\{A_i P + Dg^2\left(1+a^2\right)\left[\left(2d_{ij}M_j - M_i - M_j d_{ij}\right)P + \left(d_{ij}\left|M\right|^2 - M_i M_j\right)\frac{\partial P}{\partial M_j}\right]\right\} \quad (10)$$

$$= -\frac{\partial}{\partial M_i}\left[A_i P + Dg^2\left(1+a^2\right)\left(d_{ij}\left|M\right|^2 - M_i M_j\right)\frac{\partial P}{\partial M_j}\right]$$

$$= -\frac{\partial}{\partial M_i}\left\{A_i P - Dg^2\left(1+a^2\right)\left[\vec{M}\times\vec{M}\times\frac{\partial P}{\partial M}\right]_i\right\}$$

We assume at thermal equilibrium the system is stationary so that the ground state probability P_0 does not vary with time. Also, we assume that the distribution follows Maxwell's distribution rule, that is, the probability P follows the distribution law:

$$P = P_0 e^{-\frac{E}{k_B T}} = P_0 e^{-\frac{-m_0 \vec{M}\cdot\vec{H}V}{k_B T}} = P_0 e^{\frac{m_0 \vec{M}\cdot\vec{H}V}{k_B T}}$$

$$\text{and } \frac{\partial P}{\partial M} = \frac{\partial}{\partial M}\left(P_0 e^{\frac{m_0 \vec{M}\cdot\vec{H}V}{k_B T}}\right) = P_0 e^{\frac{m_0 \vec{M}\cdot\vec{H}V}{k_B T}}\frac{m_0 \vec{H}V}{k_B T} = \frac{m_0 V}{k_B T}HP$$

where E is the magnetic free energy. With these assumptions Eq. 10 is further reduced to:

$$\frac{\partial P}{\partial t} = -P\frac{\partial}{\partial M}\left\{-g\,\vec{M}\times\vec{H} - \left[\frac{ag}{M_s} - Dg^2\left(1+a^2\right)\frac{m_0 V}{k_B T}\right]\vec{M}\times\left(\vec{M}\times\vec{H}\right)\right\}$$

$$= P\frac{\partial}{\partial M}\left\{\left[\frac{ag}{M_s} - Dg^2\left(1+a^2\right)\frac{m_0 V}{k_B T}\right]\vec{M}\times\left(\vec{M}\times\vec{H}\right)\right\}$$

$$\text{since } \frac{\partial}{\partial M}\left(\vec{M}\times\vec{H}\right) = \frac{\partial}{\partial M_i}\left(e_{ijk}M_j H_k\right) = e_{ijk}\frac{\partial M_j}{\partial M_i}H_k = e_{ijk}d_{ij}H_k = 0$$

For the thermal ground state, the left hand side of the above equation is zero. It follows that

$$\frac{ag}{M_s} - \frac{Dg^2\left(1+a^2\right)m_0 V}{k_B T} = 0$$

or

$$D = \frac{a\,k_B T}{\left(1+a^2\right) g\, M_s m_0 V} \tag{11}$$

D is the diffusion coefficient of thermal fluctuation field of Landau-Lifshitz-Gilbert equation. If the system is described by the Gilbert equation

$$\frac{d\vec{M}}{dt} = -g'\vec{M}\times\vec{H} + \frac{a'}{M_s}\vec{M}\times\frac{d\vec{M}}{dt} \tag{12}$$

then similarly

$$D = \frac{a'k_B T}{g\, M_s m_0 V} = \frac{a\,k_B T}{g\, M_s m_0 V} \tag{13}$$

is found.

The LLG equation and the Gilbert equation Eq. 12 are equivalent in that:

$$\begin{aligned}
\vec{M}\times\frac{d\vec{M}}{dt} &= -g'\vec{M}\times\left(\vec{M}\times\vec{H}\right) + \frac{a'}{M_s}\vec{M}\times\left(\vec{M}\times\frac{d\vec{M}}{dt}\right) \\
&= -g'\vec{M}\times\left(\vec{M}\times\vec{H}\right) + \frac{a'}{M_s}\left(\left(\vec{M}\bullet\frac{d\vec{M}}{dt}\right)\vec{M} - \left(\vec{M}\bullet\vec{M}\right)\frac{d\vec{M}}{dt}\right) \\
&= -g'\vec{M}\times\left(\vec{M}\times\vec{H}\right) - \frac{a'}{M_s}\left(\left(\vec{M}\bullet\vec{M}\right)\frac{d\vec{M}}{dt}\right) \\
&= -g'\vec{M}\times\left(\vec{M}\times\vec{H}\right) - a'M_s\frac{d\vec{M}}{dt}
\end{aligned}$$

and

$$\frac{d\vec{M}}{dt} = -g'\vec{M}\times\vec{H} + \frac{a'}{M_s}\vec{M}\times\frac{d\vec{M}}{dt} = -g'\vec{M}\times\vec{H} + \frac{a'}{M_s}\left(-g'\vec{M}\times\left(\vec{M}\times\vec{H}\right) - a'M_s\frac{d\vec{M}}{dt}\right)$$

or

$$\left(1+a'^2\right)\frac{d\vec{M}}{dt} = -g'\vec{M}\times\vec{H} - \frac{a'g'}{M_s}\vec{M}\times\left(\vec{M}\times\vec{H}\right) \tag{14}$$

or

$$\frac{d\vec{M}}{dt} = \frac{-g'}{\left(1+a'^2\right)}\vec{M}\times\vec{H} - \frac{a'}{\left(1+a'^2\right)}\frac{g'}{M_s}\vec{M}\times\left(\vec{M}\times\vec{H}\right)$$

Defining $g' = \left(1+a'^2\right)g$ and $a' = a$, Eq. 12 becomes the Landau-Lifshitz-Gilbert equation.

Appendix B Micromag XML Schema

XML (Extensible Markup Language) is the basis of Micromag data, exchange, distribution and visualization. The XML schema is the foundation of XML data format of the Micromag program. It is the most important document of the Micromag program.

```
<?xml version="1.0" encoding="UTF-8"?>
<schema targetNamespace="http://jacob.chem.uno.edu/schemas/Micromag.xsd"
xmlns:mm="http://jacob.chem.uno.edu/schemas/Micromag.xsd"
xmlns="http://www.w3.org/2001/XMLSchema"
xmlns:jaxb="http://java.sun.com/xml/ns/jaxb"
xmlns:xjc="http://java.sun.com/xml/ns/jaxb/xjc" elementFormDefault="qualified"
attributeFormDefault="unqualified" jaxb:extensionBindingPrefixes="xjc"
jaxb:version="1.0">
    <annotation>
        <appinfo>
            <jaxb:globalBindings generateIsSetMethod="true">
                <xjc:serializable uid="13730112166"/>
            </jaxb:globalBindings>
        </appinfo>
    </annotation>
    <element name="AnalyticalRegion" type="mm:AnalyticalRegionType"
substitutionGroup="mm:Region"/>
    <element name="Cell" type="mm:CellType">
        <key name="CellID">
            <selector xpath="Task/ControlData/Cells/Cell"/>
            <field xpath="@CellID"/>
        </key>
    </element>
    <element name="CellData" type="mm:CellDataType"/>
    <element name="ControlData" type="mm:ControlDataType"/>
    <element name="CouplingExchangeConstant"
type="mm:CouplingExchangeConstantType"/>
    <element name="Location" type="mm:LocationType"/>
    <element name="Log" type="mm:LogType">
        <keyref name="Task" refer="mm:TaskID">
            <selector xpath="Task"/>
            <field xpath="@TaskID"/>
```

```
    </keyref>
</element>
<element name="Material" type="mm:MaterialType">
    <key name="MaterialID">
        <selector xpath="ControlData/Materials/Material"/>
        <field xpath="@MaterialID"/>
    </key>
</element>
<element name="MMData" type="mm:MMDataType"/>
<element name="Region" type="mm:RegionType">
    <key name="RegionID">
        <selector xpath="ControlData/Sample/Region"/>
        <field xpath="@RegionID"/>
    </key>
</element>
<element name="RegionData" type="mm:RegionDataType"/>
<element name="Result" type="mm:ResultType"/>
<element name="Results">
    <complexType>
        <sequence minOccurs="0" maxOccurs="unbounded">
            <element ref="mm:Result"/>
        </sequence>
    </complexType>
</element>
<element name="Sample">
    <complexType>
        <sequence maxOccurs="unbounded">
            <element ref="mm:Region"/>
        </sequence>
        <attribute name="SampleID" use="required">
            <simpleType>
                <restriction base="ID">
                    <pattern value="Sample-\d+"/>
                </restriction>
            </simpleType>
        </attribute>
    </complexType>
    <key name="SampleID">
        <selector xpath="ControlData/Sample"/>
        <field xpath="@SampleID"/>
    </key>
</element>
<element name="SampleData" type="mm:SampleDataType"/>
<element name="Step" type="mm:StepType">
    <key name="StepID">
        <selector xpath="ControlData/Hysteresis/Step"/>
```

```
            <field xpath="@StepID"/>
        </key>
    </element>
    <element name="Task">
        <complexType>
            <sequence>
                <element ref="mm:ControlData"/>
                <element ref="mm:Log"/>
                <element ref="mm:Results"/>
            </sequence>
            <attribute name="TaskID" use="required">
                <simpleType>
                    <restriction base="ID">
                        <pattern value="Task-\d+"/>
                    </restriction>
                </simpleType>
            </attribute>
        </complexType>
        <key name="TaskID">
            <selector xpath="Task"/>
            <field xpath="@TaskID"/>
        </key>
    </element>
    <element name="TimeStamp" type="mm:TimeStampType"/>
    <element name="Units">
        <complexType>
            <attribute name="Spin" type="mm:UnitSystem" use="optional"/>
            <attribute name="Field" type="mm:UnitSystem" use="optional"/>
            <attribute name="AnisotropyConstant" type="mm:UnitSystem"
use="optional"/>
            <attribute name="ExchangeConstant" type="mm:UnitSystem"
use="optional"/>
            <attribute name="MagnetostaticConstant" type="mm:UnitSystem"
use="optional"/>
            <attribute name="DampingConstant" type="mm:UnitSystem"
use="optional"/>
            <attribute name="Energy" type="mm:UnitSystem" use="optional"/>
            <attribute name="CellSize" type="mm:UnitSystem" use="optional"/>
            <attribute name="Location" type="mm:UnitSystem" use="optional"/>
            <attribute name="Time" type="mm:UnitSystem" use="optional"/>
        </complexType>
    </element>
    <element name="User" type="mm:UserType"/>
    <element name="Vec3d" type="mm:Vec3dType"/>
    <complexType name="AnalyticalRegionType">
        <complexContent>
```

```
            <extension base="mm:RegionType">
               <sequence>
                  <element name="Origin" type="mm:Vec3dType" minOccurs="0"/>
                  <element name="Axis" type="mm:Vec3dType" minOccurs="0"/>
                  <element name="Angle" type="double" minOccurs="0"/>
                  <sequence minOccurs="0" maxOccurs="unbounded">
                     <element name="Constraint">
                        <complexType>
                           <attribute name="cx2" type="double" use="optional"
default="0"/>
                           <attribute name="cy2" type="double" use="optional"
default="0"/>
                           <attribute name="cz2" type="double" use="optional"
default="0"/>
                           <attribute name="cxy" type="double" use="optional"
default="0"/>
                           <attribute name="cxz" type="double" use="optional"
default="0"/>
                           <attribute name="cyz" type="double" use="optional"
default="0"/>
                           <attribute name="cx" type="double" use="optional"
default="0"/>
                           <attribute name="cy" type="double" use="optional"
default="0"/>
                           <attribute name="cz" type="double" use="optional"
default="0"/>
                           <attribute name="sign" type="mm:SignType"
use="optional" default="Equals"/>
                           <attribute name="c" type="double" use="optional"
default="0"/>
                        </complexType>
                     </element>
                  </sequence>
               </sequence>
            </extension>
         </complexContent>
      </complexType>
      <complexType name="CellDataType">
         <sequence>
            <element ref="mm:MMData"/>
         </sequence>
         <attribute name="Cell" type="IDREF" use="required"/>
      </complexType>
      <complexType name="CellType">
         <annotation>
            <documentation>
```

```
            Magnetic cell
          </documentation>
        </annotation>
        <all>
          <element ref="mm:Location"/>
          <element name="EasyAxis" type="mm:Vec3dType"/>
          <element name="SecondEasyAxis" type="mm:Vec3dType"
minOccurs="0"/>
          <element name="Spin" type="mm:Vec3dType"/>
          <element name="AppliedField" type="mm:Vec3dType" minOccurs="0"/>
          <element name="Neighbors" type="IDREFS" minOccurs="0"/>
        </all>
        <attribute name="CellID" use="required">
          <simpleType>
            <restriction base="ID">
              <pattern value="Cell-\d+"/>
            </restriction>
          </simpleType>
        </attribute>
        <attribute name="Region" type="IDREF" use="required"/>
    </complexType>
    <complexType name="ControlDataType">
        <sequence>
          <element name="Title" type="string"/>
          <element name="Description" type="string"/>
          <element ref="mm:User"/>
          <element ref="mm:Units"/>
          <element name="Bound" type="mm:LocationType"/>
          <element name="CellSize" type="mm:Vec3dType"/>
          <element name="ConvergenceLimit" type="double" default="1e-5"/>
          <element name="MaximumTimeStep" type="double" default="0.4"
minOccurs="0"/>
          <element name="MinimumTimeStep" type="double" default="0.001"
minOccurs="0"/>
          <element name="MaximumIterationNumber" type="int" default="3000"
minOccurs="0"/>
          <element name="Temperature" type="double" minOccurs="0"/>
          <element name="Hysteresis" minOccurs="0">
            <complexType>
              <sequence maxOccurs="unbounded">
                <element ref="mm:Step"/>
              </sequence>
            </complexType>
          </element>
          <element name="Materials">
            <complexType>
```

```
                <sequence maxOccurs="unbounded">
                    <element ref="mm:Material"/>
                </sequence>
            </complexType>
        </element>
        <element ref="mm:CouplingExchangeConstant"/>
        <element ref="mm:Sample"/>
        <element name="Cells">
            <complexType>
                <sequence maxOccurs="unbounded">
                    <element ref="mm:Cell"/>
                </sequence>
            </complexType>
        </element>
    </sequence>
</complexType>
<complexType name="CouplingExchangeConstantType">
    <sequence minOccurs="0" maxOccurs="unbounded">
        <element name="Couple">
            <complexType>
                <attribute name="Material_A" type="IDREF" use="required"/>
                <attribute name="Material_B" type="IDREF" use="required"/>
                <attribute name="DoubleValue" type="double" use="required"/>
            </complexType>
        </element>
    </sequence>
</complexType>
<complexType name="LocationType">
    <annotation>
        <documentation>
            Generic location, coordinates must be integer
            </documentation>
    </annotation>
    <sequence>
        <element name="x" type="int" default="0"/>
        <element name="y" type="int" default="0"/>
        <element name="z" type="int" default="0"/>
    </sequence>
</complexType>
<complexType name="LogType">
    <sequence>
        <element ref="mm:TimeStamp" minOccurs="0"
maxOccurs="unbounded"/>
    </sequence>
    <attribute name="Task" type="IDREF" use="required"/>
</complexType>
```

```
    <complexType name="MaterialType">
        <annotation>
            <documentation>
                Magnetic material descriptor
             </documentation>
        </annotation>
        <sequence>
            <element name="MaterialName" type="string"/>
            <element name="Anisotropy">
                <complexType>
                    <attribute name="Type" type="mm:AnisotropyClass"
use="required"/>
                </complexType>
            </element>
            <element name="AnisotropyConstant" type="double"/>
            <element name="SecondAnisotropyConstant" type="double"
minOccurs="0"/>
            <element name="SelfExchangeConstant" type="double"/>
            <element name="DampingConstant" type="double"/>
            <element name="MagnetoSaturationConstant" type="double"/>
            <element name="DisplayColor" minOccurs="0">
                <complexType>
                    <sequence>
                        <element name="Red" type="int"/>
                        <element name="Green" type="int"/>
                        <element name="Blue" type="int"/>
                    </sequence>
                </complexType>
            </element>
        </sequence>
        <attribute name="MaterialID" use="required">
            <simpleType>
                <restriction base="ID">
                    <pattern value="Material-\d+"/>
                </restriction>
            </simpleType>
        </attribute>
    </complexType>
    <complexType name="MMDataType">
        <annotation>
            <documentation>
                MicroMagnetism dataset
             </documentation>
        </annotation>
        <sequence>
            <element name="Spin" type="mm:Vec3dType"/>
```

```
            <element name="TotalField" type="mm:Vec3dType" minOccurs="0"/>
            <element name="AnisotropyField" type="mm:Vec3dType"/>
            <element name="ExchangeField" type="mm:Vec3dType"/>
            <element name="MagnetostaticField" type="mm:Vec3dType"/>
            <element name="AppliedField" type="mm:Vec3dType" minOccurs="0"/>
            <element name="ThermalField" type="mm:Vec3dType"
minOccurs="0"/>
            <element name="TotalEnergy" type="double" minOccurs="0"/>
            <element name="AnisotropyEnergy" type="double"/>
            <element name="ExchangeEnergy" type="double"/>
            <element name="MagnetostaticEnergy" type="double"/>
            <element name="ZeemanEnergy" type="double" minOccurs="0"/>
            <element name="ThermalEnergy" type="double" minOccurs="0"/>
            <element name="Torque" type="double" minOccurs="0"/>
        </sequence>
    </complexType>
    <complexType name="RegionType">
        <sequence>
            <element name="InitialSpinPattern">
                <complexType>
                    <attribute name="Pattern" type="mm:SpinPatternType"
use="required"/>
                </complexType>
            </element>
            <element name="EasyAxis" type="mm:Vec3dType"/>
            <element name="InitialSpin" type="mm:Vec3dType" minOccurs="0"/>
            <element name="SecondEasyAxis" type="mm:Vec3dType"
minOccurs="0"/>
        </sequence>
        <attribute name="RegionID" use="required">
            <simpleType>
                <restriction base="ID">
                    <pattern value="Region-\d+"/>
                </restriction>
            </simpleType>
        </attribute>
        <attribute name="Material" type="IDREF" use="required"/>
    </complexType>
    <complexType name="RegionDataType">
        <sequence>
            <element ref="mm:MMData"/>
        </sequence>
        <attribute name="Region" type="IDREF" use="required"/>
    </complexType>
    <complexType name="ResultType">
        <sequence>
```

```
        <element name="SimulationTime" type="double"/>
        <sequence minOccurs="0" maxOccurs="unbounded">
            <element ref="mm:CellData"/>
        </sequence>
        <sequence minOccurs="0" maxOccurs="unbounded">
            <element ref="mm:RegionData"/>
        </sequence>
        <element ref="mm:SampleData" minOccurs="0"/>
    </sequence>
    <attribute name="Task" type="IDREF" use="required"/>
    <attribute name="Step" type="IDREF" use="required"/>
</complexType>
<complexType name="SampleDataType">
    <sequence>
        <element ref="mm:MMData"/>
    </sequence>
    <attribute name="Sample" type="IDREF" use="required"/>
</complexType>
<complexType name="StepType">
    <complexContent>
        <extension base="mm:Vec3dType">
            <attribute name="StepID" use="required">
                <simpleType>
                    <restriction base="ID">
                        <pattern value="Step-\d+"/>
                    </restriction>
                </simpleType>
            </attribute>
        </extension>
    </complexContent>
</complexType>
<complexType name="TimeStampType">
    <attribute name="Sequence" type="int" use="required"/>
    <attribute name="Time" type="dateTime" use="required"/>
    <attribute name="Status" type="mm:StatusType" use="required"/>
</complexType>
<complexType name="UnitType">
    <attribute name="Unit" type="mm:UnitSystem" use="required"/>
    <attribute name="Surffix" type="string" use="optional"/>
</complexType>
<complexType name="UserType">
    <annotation>
        <documentation>
            MicroMagnetism user
         </documentation>
    </annotation>
```

```
    <sequence>
      <element name="Name" type="string"/>
      <element name="Contact" type="string" minOccurs="0"/>
    </sequence>
</complexType>
<complexType name="Vec3dType">
    <annotation>
      <documentation>
        Generic 3-tuple vector
       </documentation>
    </annotation>
    <sequence>
      <element name="x" type="double"/>
      <element name="y" type="double"/>
      <element name="z" type="double"/>
    </sequence>
    <attribute name="Suffix" type="string" use="optional"/>
</complexType>
<simpleType name="AnisotropyClass">
    <restriction base="string">
      <enumeration value="uniaxial"/>
      <enumeration value="cubic"/>
    </restriction>
</simpleType>
<simpleType name="SignType">
    <restriction base="string">
      <enumeration value="GreaterThan"/>
      <enumeration value="GreaterOrEquals"/>
      <enumeration value="Equals"/>
      <enumeration value="LessOrEquals"/>
      <enumeration value="LessThan"/>
    </restriction>
</simpleType>
<simpleType name="SpinPatternType">
    <restriction base="string">
      <enumeration value="uniform"/>
      <enumeration value="random"/>
      <enumeration value="vortex"/>
    </restriction>
</simpleType>
<simpleType name="StatusType">
    <restriction base="string">
      <enumeration value="defined"/>
      <enumeration value="submitted"/>
      <enumeration value="started"/>
      <enumeration value="stepFailed"/>
```

```
            <enumeration value="stepDone"/>
            <enumeration value="canceled"/>
            <enumeration value="finished"/>
            <enumeration value="failed"/>
        </restriction>
    </simpleType>
    <simpleType name="UnitSystem">
        <restriction base="string">
            <enumeration value="cgs"/>
            <enumeration value="reduced"/>
            <enumeration value="metric"/>
            <enumeration value="suffixed"/>
        </restriction>
    </simpleType>
</schema>
```

Appendix C Micromag Computational Algorithms

This section gives the algorithms in reducing material parameters, evaluating magnetic field and energy terms and evaluating and integrating the LLG equation. Snips of JAVA source codes are listed. Most of them are self-explanatory. Necessary comments are given.

Reducing Parameters:

```
//Eq. 2.19 and Eq 2.14
  private void reduce()
  {
    if (u0ms2==0) return;
    a = 2*A/u0ms2;
    k1 = 2*K1/u0ms2;
    k2 = 2*K2/u0ms2;
  }

//Eq. 2.9
  public double getTimeInMetric(double time)
  {
    return time/(gamma*Ms);
  }

//Eq. 2.9
  public double getTimeReduced(double time)
  {
    return time*gamma*Ms;
  }

//Eq. 2.7
  public void reduceField(VecMate field)
  {
    if (Ms!=0) field.timesEquals(1.0/Ms);
  }
```

Calculating Fields and Energy:

- Uniaxial anisotropy

```
//Eq.2.19 and Eq. 2.20
  public void calculate()
  {
    reset();
```

```
    dot = spin.dot(a); //a is easy axis vector
    double multi = k1*dot + 2*k2*dot*(1-dot*dot);
    field.set(a);
    field.timesEquals(multi);

    double dot2 = dot*dot;

    if (k1>0) energy = k1*(1-dot2); else energy = -k1*(1-dot2);
    energy += k2*(1-dot2)*(1-dot2);
    energy *= 0.5;
  }
```

- Cubic anisotropy

```
//Eq.2.21 and Eq 2.22
  public void calculate()
  {
    reset();

    dota2 = spin.dot(a); dota2 *= dota2; //a, b, c are easy axes
    dotb2 = spin.dot(b); dotb2 *= dotb2;
    dotc2 = spin.dot(c); dotc2 *= dotc2;

    temp.set(a);
    temp.timesEquals(k1*(1-dota2) + k2*dotb2*dotc2);
    field.plusEquals(temp);

    temp.set(b);
    temp.timesEquals(k1*(1-dotb2) + k2*dota2*dotc2);
    field.plusEquals(temp);

    temp.set(c);
    temp.timesEquals(k1*(1-dotc2) + k2*dota2*dotb2);
    field.plusEquals(temp);

    energy = (dota2*dotb2+dota2*dotc2+dotb2*dotc2)*k1 +
          (dota2*dotb2*dotc2)*k2;
    energy *= 0.5;
  }
```

- Exchange

```
as[i] = eca[i] * 2.0 / (u0ms2*area);
//as[i] is the reduced coupling exchange constant with a neighbor cell
//area is the area of the cross-section to connecting the neighbor
  public void calculate()
  {
```

```
  reset();
  for (int i=0; i<ss.length; i++) //sum over all neighbors
  {
    temp = VecMate.minus(ss[i], spin, temp);
    energy += temp.dot(temp) * as[i] /2.0;
    temp.timesEquals(as[i]);
    field.plusEquals(temp);
  }
 }
```

- Magnetostatic field

Magnetostatic field is calculated in different ways. Listed here is the local direct calculation without FFT or distribution.

```
 public void calculate()
 {
  reset();

  DemagTensor tensor;
  Vector3 v3 = new Vector3();
  CellMate there;
  VecMate m;
  for (int i=0; i<cells.length; i++) //loop over all cells
  {
    there = cells[i];
    //demag tensor is pre-calculated and stored for repeated usage
    //see Eqs.2.28-2.37
    tensor = getTensor(there);
    m= there.getData().M;
    v3.set(m.getX(), m.getY(), m.getZ());
    v3 = tensor.times(v3);                          //Eq. 2.23
    temp.set(v3.x, v3.y, v3.z);
    temp.timesEquals(-ratios[i]);
    field.plusEquals(temp);
    energy += field.dot(spin);
  }
  energy *= 0.5; //avoid double count
 }
```

- Zeeman field

Zeeman field is given. Zeeman energy is calculated following Eq. 2.42.

```
//Eq. 2.42
  public void calculate()
```

```
  {
   energy = spin.dot(field)*-1.0;
  }
```

- Thermal field and other fields

The thermal field is not implemented. The body of the "calculate" method is currently empty. Implementation of this method will realize the thermal field and make the program stochastic. Other fields, such as the RKKY exchange and magnetoelastic anisotropy, can be included in the program without changing other modules of the program, as long as the field terms implement the interface of all field terms.

```
public interface FieldMate extends java.io.Serializable
{
  boolean isValid();
  void invalidate();
  void init(CellMate cell);
  void calculate();
  VecMate getField();
  double getEnergy();
}
```

- Evaluating the LLG equation for each cell

```
Compute individual field and energy terms
  //remember to calculate demag field immediately before calling this method if it is not
calculated in this method
  //the method computes every field term for a cell. Demag field may be calculated
globally
  public void calculate()
  {
    am.calculate(); //anisotropy
    em.calculate(); //exchange
    zm.calculate(); //Zeeman
    tm.calculate(); //thermal
     //additional field terms here
  }

//evaluate the LLG equation for an individual cell
  public void evaluateLLG()
  {
    data.Ea = am.getEnergy(); //populate the data structure with energy terms
    data.Ee = em.getEnergy();
```

```
    data.Ez = zm.getEnergy();
    data.Et = tm.getEnergy();
    data.sumerize(); //compute the local effective field and total energy for a cell

    data.DMDT = VecMate.cross(data.M, data.H, data.DMDT); //compute torque
    data.setTorque(data.DMDT.getNormal());
    temp = VecMate.cross(data.M, data.DMDT, temp);
    temp.timesEquals(cell.getAlpha());
    data.DMDT.plusEquals(temp);
    data.DMDT.timesEquals(-1); //lhs of the LLG equation is dm/dt
  }

//given the time step, get the updated spin using Jacob's method
  public VecMate getNextSpin(double timeInMetric, VecMate result)
  {
    double time = cell.getTimeReduced(timeInMetric); //reduce time to dimensionless
    double alpha = cell.getAlpha(); //damping coefficient
    temp = VecMate.cross(data.M, data.H, temp); // m X h

    //dmdt = -m X h - a m X (m X h)
    data.DMDT = VecMate.linearCombine(-1, temp, alpha, data.H, data.DMDT); //-
mXh+ah
    temp.set(data.M); temp.timesEquals(alpha*data.M.dot(data.H)); //a(m,h)m
    data.DMDT.minusEquals(temp); //dmdt

    result = VecMate.linearCombine(1.0, data.M, time, data.DMDT, result);
    result.normalize(); //enforce constant magnitude
    return result;
  }

//given the time step, get the updated spin using Gauss-Seidel method
  public VecMate getNextSpinGS(double timeInMetric, VecMate result)
  {
    VecMate m = data.M, h = data.H;
    double alpha = cell.getAlpha();
    double deltaT = cell.getTimeInMetric(timeInMetric);

    double m1 = m.getX(), m2 = m.getY(), m3 = m.getZ();
    double h1 = h.getX(), h2 = h.getY(), h3 = h.getZ();
    double da = m.dot(h)*cell.getAlpha(); //alpha * (m, h)

    m1 = m1 - deltaT * ((m2*h3-m3*h2) + da*m1 - alpha*h1);
    m2 = m2 - deltaT * ((m3*h1-m1*h3) + da*m2 - alpha*h2);
    m3 = m3 - deltaT * ((m1*h2-m2*h1) + da*m3 - alpha*h3);

    result.set(m1, m2, m3);
```

```
  result.normalize();
  return result;
}
```

- Evaluating the LLG equation for the entire sample

```
public double evaluateLLG(VecMate Hext, boolean calDemag)
{
  CellEvolver ce;
  double tor;

  Thread spliterThread = null;

  maxTor = -1;

  if (calDemag) //calculate demag term globally in a separate thread
  {
    spliterThread = new Thread(spliter);
    spliterThread.start();
  }
  //apply an external field and calculate field and energy terms for every cell
  for (int i=0; i<length; i++)
  {
    ce = ces[i];
    ce.setAppliedField(Hext);

    ce.calculate();
  }
  //if demag term is calculated in a separate theread, wait for it to finish
  if (calDemag)
    try
    {
      spliterThread.join();
    }
    catch (InterruptedException ie) { }
  //evaluate the LLG equation for each cell
  //return the maximum magnitude of the torque for all cells to check convergency
  for (int i=0; i<length; i++)
  {
    ce = ces[i];
    ce.evaluateLLG();
    tor = ce.getTorque();
    //update maximum torque
    //remember the Ms of the cell with maximum torque, for constant reducing purpose
    if (maxTor<tor)
    {
      maxIndex = i;
```

```
      maxTor = tor;
      maxMs = ce.getCell().getMs();
    }
  }
  return maxTor;
}
```

Vita

The author was born in China in 1968. He received his B.S. in chemistry from Huazhong University of Science and Technology in Wuhan, China in 1989. He attended Beijing Normal University in Beijing, China to study computational chemistry and received his master's degree in computational chemistry in 1992. After graduation he went back to Huazhong University of Science and Technology to work as an assistant professor of chemistry. He taught general and physical chemistry courses until 1998.

In 1999 he became a graduate student in the chemistry department of University of New Orleans. He also received a master's degree in computer science from the University of New Orleans in 2003.